

ISSN • 2708-6437 (Online)  
• 2708-6429 (Print)

# Journal of Engineering Advancements

**Editor-in-Chief:**

**Prof. Dr. Mohammad Mashud**

**Volume 03 Issue 01**



**Published by:  
SciEn Publishing Group**

# Journal of Engineering Advancements

Apt. # 6 C-D, House # 191  
Road # 9/A, Dhanmondi R/A  
Dhaka-1209, Bangladesh

Email: [jea@scienpg.com](mailto:jea@scienpg.com)

Website: [www.scienpg.com/jea/](http://www.scienpg.com/jea/)

---

## *Editor-in-Chief*

Prof. Dr. Mohammad Mashud  
Khulna University of Engineering & Technology  
Khulna-9203, Bangladesh.  
Tel: +880-41-769468 Ext. 405  
Email: [mdmashud@me.kuet.ac.bd](mailto:mdmashud@me.kuet.ac.bd)

## *Executive Editors*

Dr. Md. Arifuzzaman  
Khulna University of Engineering & Technology  
Khulna-9203, Bangladesh.  
Email: [arif48@me.kuet.ac.bd](mailto:arif48@me.kuet.ac.bd)

Dr. Md. Shariful Islam  
Khulna University of Engineering & Technology  
Khulna-9203, Bangladesh.  
Email: [msislam@me.kuet.ac.bd](mailto:msislam@me.kuet.ac.bd)

## *Editors*

Dr. Abul Mukid Mohammad Mukaddes  
Shahjalal University of Science and Technology  
Email: [mukaddes1975@gmail.com](mailto:mukaddes1975@gmail.com)

Dr. Seock Sam Kim  
University Malaysia Sabah  
Email: [sskim@ums.edu.my](mailto:sskim@ums.edu.my)

Dr. Chu Chi Ming  
University Malaysia Sabah  
Email: [chrischu@ums.edu.my](mailto:chrischu@ums.edu.my)

Dr. Sabuj Mallik  
University of Derby  
Email: [s.mallik@derby.ac.uk](mailto:s.mallik@derby.ac.uk)

Dr. Mohammad H. Rahman  
University of Wisconsin-Milwaukee  
Email: [rahmanmh@uwm.edu](mailto:rahmanmh@uwm.edu)

Dr. Mohd Suffian Bin Misaran  
University Malaysia Sabah  
Email: [suffian@ums.edu.my](mailto:suffian@ums.edu.my)

Dr. Sivakumar Kumaresan  
University Malaysia Sabah  
Email: [shiva@ums.edu.my](mailto:shiva@ums.edu.my)

Dr. Zahir Uddin Ahmed  
Khulna University of Engineering & Technology  
Email: [zuahmed@me.kuet.ac.bd](mailto:zuahmed@me.kuet.ac.bd)

Dr. Md. Mizanur Rahman  
World University of Bangladesh  
Email: [mizanur.rahman@mte.wub.edu.bd](mailto:mizanur.rahman@mte.wub.edu.bd)

Dr. Mohammad Ilias Inam  
Khulna University of Engineering & Technology  
Email: [iliasinam@me.kuet.ac.bd](mailto:iliasinam@me.kuet.ac.bd)

Dr. Riaz U. Ahmed  
University of Wisconsin-Green Bay  
Email: [ahmedm@uwgb.edu](mailto:ahmedm@uwgb.edu)

Dr. Md. Mahfuz Sarwar  
AECOM  
Email: [mahfuzsarwar@yahoo.com](mailto:mahfuzsarwar@yahoo.com)

Dr. Kazi Mostafijur Rahman  
Khulna University of Engineering & Technology  
Email: [mostafij@me.kuet.ac.bd](mailto:mostafij@me.kuet.ac.bd)

Dr. Md. Abdullah Al Bari  
Khulna University of Engineering & Technology  
Email: [abdullahalbari@me.kuet.ac.bd](mailto:abdullahalbari@me.kuet.ac.bd)

Dr. Md. Rashedul H. Sarker  
University of Indianapolis  
Email: [sarkerm@uindy.edu](mailto:sarkerm@uindy.edu)

Dr. Md. Najmul Hossain  
Pabna University of Science & Technology  
[najmul\\_eece@pust.ac.bd](mailto:najmul_eece@pust.ac.bd)



Published in: March 2022

Published by: SciEn Publishing Group

---

Price: Each Issue BDT 200.00 (US\$ 15)

ISSN: 2708-6437 (Online) 2708-6429 (Print)

# Journal of Engineering Advancements

Volume 03, Issue 01

March 2022

## CONTENTS

### Original Articles

01. A Real-time Face Mask Detection and Social Distancing System for COVID-19 using Attention-InceptionV3 Model  
*Abdullah Al Asif, Farhana Chowdhury Tisha* 1
02. The Decolorization and Phytotoxic Efficiency of Jackfruit Seed on a Textile Dye Novacron Blue  
*Rafi Ahmed Miah, Mohammad Jahangir Alam, Aklima Khatun, Mahmudul Hassan Suhag, Md. Nazmul Kayes* 6
03. Evaluation of Different Turbulence Models at Low Reynolds Number for the Flow over Symmetric and Cambered Airfoils  
*Tafsirul Hassan, Md. Tazul Islam, Md. Mizanur Rahman, Abu Raihan Ibna Ali, Asif Al Ziyen* 12
04. Mechanical and Energy Absorption Performance of Expanded Perlite Foam-filled Steel Tubes  
*Sadman Shahriar, Md Arifuzzaman, Pranto Karua* 23
05. Fundamental Study of CH<sub>4</sub>-Air Combustion under an Axisymmetric Small-scale Rectangular Combustor using Computational Modeling  
*Karan Gaglani, Md. Amzad Hossain* 29

This page is intentionally left blank.

# Journal of Engineering Advancements

Editor-in-Chief

Prof. Dr. Mohammad Mashud  
Department of Mechanical Engineering,  
Khulna University of Engineering & Technology, Khulna, Bangladesh

Executive Editors

Dr. Md. Shariful Islam  
Department of Mechanical Engineering,  
Khulna University of Engineering & Technology, Khulna, Bangladesh

&

Dr. Md. Arifuzzaman  
Department of Mechanical Engineering,  
Khulna University of Engineering & Technology, Khulna, Bangladesh



**Published by: SciEn Publishing Group**

Apt. # 6 C-D, House # 191, Road # 9/A  
Dhanmondi, Dhaka-1209, Bangladesh  
Email Address: [jea@scienpg.com](mailto:jea@scienpg.com)

[www.scienpg.com/jea/](http://www.scienpg.com/jea/)

This page is left intentionally blank

# A Real-time Face Mask Detection and Social Distancing System for COVID-19 using Attention-InceptionV3 Model

Abdullah Al Asif<sup>1,\*</sup>, Farhana Chowdhury Tisha<sup>2</sup>

<sup>1</sup>BRAC James P Grant School of Public Health, BRAC University, Dhaka-1213, Bangladesh

<sup>2</sup>Department of Computer Science and Engineering, East West University, Dhaka-1212, Bangladesh

Received: December 18, 2021, Revised: March 01, 2022, Accepted: March 02, 2022, Available Online: March 04, 2022

## ABSTRACT

One of the deadliest pandemics is now happening in the current world due to COVID-19. This contagious virus is spreading like wildfire around the whole world. To minimize the spreading of this virus, World Health Organization (WHO) has made protocols mandatory for wearing face masks and maintaining 6 feet physical distance. In this paper, we have developed a system that can detect the proper maintenance of that distance and people are properly using masks or not. We have used the customized attention-inceptionv3 model in this system for the identification of those two components. We have used two different datasets along with 10,800 images including both with and without Face Mask images. The training accuracy has been achieved 98% and validation accuracy 99.5%. The system can conduct a precision value of around 98.2% and the frame rate per second (FPS) was 25.0. So, with this system, we can identify high-risk areas with the highest possibility of the virus spreading zone. This may help authorities to take necessary steps to locate those risky areas and alert the local people to ensure proper precautions in no time.

Keywords: COVID-19, Real-time, Social Distancing, Facemask Detection, Attention, InceptionV3, Euclidean Distance, CNN.



This work is licensed under a [Creative Commons Attribution-Non Commercial 4.0 International License](https://creativecommons.org/licenses/by-nc/4.0/).

## 1 Introduction

In December 2019, Wuhan, the People's Republic of China, reported the discovery of a new virus called 2019-nCoV. The virus became an outbreak in 2020 around the world. It has caused the 21st century's global health crisis. The condition has been declared a COVID-19 pandemic by the World Health Organization (WHO). According to the world meters data, more than 250 million people have been impacted, with 5.1 million individuals dying around the world [1]. This virus is growing extremely powerful as it develops the capacity to modify its pattern on its own, making it increasingly difficult to erase. As this virus is highly infectious, it can infect a substantial percentage of people within a short period. Fever, cough, runny nose, chills, weakness, body ache, loss of taste and smell, and shortness of breath are all usual symptoms. Since most of these symptoms are identical to the influenza virus, many individuals ignore them until they become severe, which in some cases, death results. This severity has compelled governments in several nations to implement lockdowns to prevent the virus from spreading, resulting in a massive crisis in many industries. Scientists and the World Health Organization (WHO) confirmed that this virus transmits through human interaction, so they have recommended some protocols for safety measurements to reduce the transmission of COVID-19. By wearing a facemask and maintaining social distancing, people can ensure their safety in some situations [2]. An infected person should not interact with anyone and should stay at home if they do not need a medical emergency. Wearing a facemask and keeping social distance are also effective ways to reduce physical contact. As a result, our primary goal in the current context is to give technical services to make sure that these two indicators are appropriately enforced. Some dedicated research works have been done for facial recognition or measuring distance calculation, but we never

expected that facemask detection or ensuring maintenance of social distancing could be a vital aspect considering the current situation. For this purpose, many researchers mostly considered various versions of the YOLO algorithm for implementing those safety measurements. But most of them faced the scarcity of datasets, not enough research materials on this area, not enough implementation of different types of models for the comparison purpose as well. Our objective is to find out that the two of the basic safety measurements of COVID-19 such as wearing facemask and maintenance of social distancing are properly getting maintained with having minimal infringements by people in public places.

We used deep learning approaches to identify facial masks and social distance between persons. As we know that the attention model works best for identifying any particular object on the real-time dataset. Besides, the inceptionv3 model also works well for object detection purposes as it has the advantages of extra layers in it with minimal computational cost in the shortest time. That is why we combined these two models in our system. We have used inceptionv3 for pre-train purposes and the attention model as the final layer in it. We have summarized them in the points below:

In both situations, we employed the object detection approach and the method is capable of detecting anomalies in real-time video feeds.

## 2 Related Works

Almost the whole world got to face the outburst of the COVID-19 tragedy. This infectious disease shows almost similar symptoms to the influenza virus, but still, medical researchers and pharmaceuticals are unable to invent the appropriate remedy for this virus. It is very difficult to say how long it will take to find the proper medication or vaccination for the disease. According to WHO, reduction in human physical interaction can

decrease the transference of COVID-19, so that is why considering the current situation, it has become the most significant matter to contemplate. Many researchers around the world also tried to use some tracking devices or drones using Bluetooth and GPS to locate covid affected people and in India, Aarogya Setu was one of them [3]. The application was intended to be made for Indian people mostly as this app supported many Indian languages. Some of them used wireless signal amplitude wave-form for human detection as well [4]. But in this case, a huge number of antennas needed to be implemented to work out this properly, but this might cost a lot of time and money. As the Covid-19 outburst is very recent, so there are not so many papers that have been researched on this issue particularly. But Face masks and human detection can be considered object detection in computer vision. However, object detection and classification are very well-known terms in the technical world. In state-of-the-art, the advancement of computer vision and deep learning methods has been shown immense progress in so many circumstances. There are lots of popular models and algorithms like Convolutional Neural Network (CNN), Recurrent Neural Network (RNN), etc. in deep learning that has been used in this subject. Convolutional Neural Network is one of the deep learning categories that has been accomplished great performing capability in image recognition standards. Different CNN models such as AlexNet, InceptionV3, ResNet-50, VGG16, etc. are showing great success in detecting objects in various scenarios due to high-performance computing systems [5]. CNN is also undoubtedly used for the classification part and for getting more information from an image.

Many researchers mostly acknowledged one of the CNN-based model's various versions of the YOLO (You Only Look Once) algorithm for optimized object detection in real-time [6]-[9]. YOLOv3 algorithm has been considered for detecting social distance by using the 2-dimensional top-down view of video footage where the camera angle was fixed [10]. They have monitored and calculated the distance between pedestrians by creating a fixed square-shaped place on the street. Their model can also detect the pedestrian's half body when they enter the box. But it cannot show any result until the object is inside of the box. So, if any object avoids that fixed place, the system will not be able to detect it. If this limitation is revealed, people easily would be able to deceive this system.

Another researcher proposed a model which is a combination with an inverse perspective mapping (IPM) technique with the YOLOv4-based Deep Neural Network (DNN) model, and it is applicable for different environments using CCTV cameras [6]. For face detection in real-time, the Haar Cascade classifier and YOLOv3 algorithm have been used as well [8]. A device like glasses was made for blind people with an alarm to maintain social distancing for the Covid-19 issue [11]. But the device does not warn the person of anything except other persons is in the reported distance. These devices were based on GPS, Wi-Fi, and networks and that is why those devices cannot work when the device will lose every type of connection from it. Some of the other developers used two other CNN-based models in their hardware devices such as VGG16, MobileNetv2 as well [12],[13].

Face detection was widely used in the state-of-the-art but detection of facemask for limiting the transference of the virus is now a very important event in the current situation. People need to ensure that they are properly wearing their facemask and keep following social distancing as very basic steps in public places.

Another noticeable fact was that there was no implementation of these preliminary steps together in one system. After observing these research gaps, we have proposed a model with the maintenance of those two safety measures which were not supposedly used for this purpose more accurately in the shortest time till now.

### 3 Methodology

The suggested model has two primary components: The model is deep transfer learning for face mask identification with the customized inception-v3 model, and the second one is calculating the Euclidean distance between pixels of an image. The Inception network has been meticulously designed. Google's Inception V3 is the third version in a series of Deep Learning Convolutional Architectures. Inception V3 was trained with 1,000 classes from the original ImageNet dataset, which was trained with over 1 million training pictures [14].

In our research findings, we did not notice that any other researcher used this model for this purpose yet. We want to build this system for real-time, so time efficiency is very much important. In that case, the attention mechanism plays a vital role. Generally, the concept of the attention model is inspired by the function of the human eye. Our eyes can catch a fairly wide perspective of the world, but we tend to "glance" at the overview and only pay attention to a small portion of it, leaving the rest "blurred out." The attention model tries to capitalize on this concept by allowing the neural network to "focus" its "attention" on the most interesting part of the image, where it can get the most information while paying less "attention" elsewhere, resulting in a reduction in the amount of image processing power required [15]. Besides, the inceptionv3 model also works well for object detection purposes as it has the advantages of extra layers in it. That is why we combined these two models in our system. We have used inceptionv3 for pre-train purposes and the attention model as the final layer in it.

#### 3.1 Data Collection

The experiments in this study were carried out on two different datasets along with 10,800 images including both with and without Face Mask images. The first dataset has taken from a website (<https://makeml.app/datasets/mask>) under a public domain license with 1776 images [16]. The rest of the 9024 images were collected and filtered from the search engines using Bing-image-downloader [17]. This is known as a python library to download the bulk of images from Bing.com. For the training, validation, and testing phases, both datasets were used.

#### 3.2 Facemask Detection

The purpose is to create a facemask detection system by retraining certain modified final layers with attention mechanisms and utilizing a pre-trained inceptionv3 as a base model. So, this part consists of two parts which are feature extraction and classification. The pre-trained inceptionv3 model is deployed as a standalone feature extraction part, in which case input images are pre-processed by the model or a portion of the model to produce an output (e.g., a vector of numbers) that may subsequently be utilized as input for training a new model. The default input image size of Inception-v3 is 299×299; however, the image shape resized into 150×150 pixels in this model. This did not affect the number of channels, but only on the size of the feature maps created during the method, and the outcome was adequate. The feature map dimensions after the convolutional

layers and Inception modules were 3×3 with 2,048 channels as in shown Fig. 1. This is all about the extraction of general features from input images.

Now the visual soft attention mechanism comes to play to classify the images based on the features obtained from the inceptionv3 model. The attention model is a streamlined attempt that focuses on the few relevant things of the selective activities [18]. As a result, this classification system focuses on human faces and determines whether or not the individual is wearing a mask.

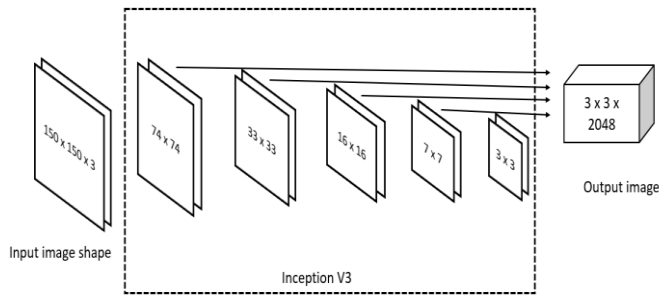


Fig. 1 The model architecture of inceptionV3

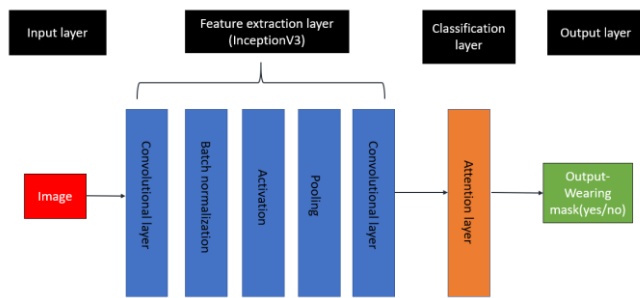


Fig. 2 The proposed transfer learning model

In transfer learning, the method reuses the feature extraction component and re-trains the classification section with the desired dataset. As the feature extraction section (which is the most complex part of the model) does not have to be trained, as shown in Fig. 2, it takes fewer computer resources and less training time to train the model.

### 3.1. Measuring Social Distance (SD)

People cannot share germs if they are not close together, hence social distance is undoubtedly the most effective prevention technique to limit disease spread. This section focuses on determining the distance between persons in public places using our suggested technique. The human face recognition and tracking module receives video stream sequences from the cameras. To measure the level of social distance practiced, factors such as the center of a person’s position and distance between them play a vital role [19]. The color of the bounding box, green to red, will be changed by an alert for the social distancing violation.

First, we locate any human face and denote it as the marker. Then, we calculate its width in pixels by taking the difference of the horizontal coordinates of the bounding box’s top-left corner ( $X_1$ ) and bottom-right corner ( $X_2$ ) and denote it as  $P = X_2 - X_1$  [20].

The distance between two people determines how close they are. The decision is based on a comparison of the distance vector with a threshold value. If the Euclidean distance between two things is less than a certain threshold value, it is thought that they are not adhering to the social distancing rules or have not created adequate distance between them. The distance between two pixels is calculated by the following formula:

$$\text{Euclidean distance, } d(p, q) = \sqrt{\sum_{i=1}^n (q_i - p_i)^2},$$

where,  $p, q$  = two points in Euclidean  $n$ -space,  $n$  = Number of dimensions,  $q_i, p_i$  = Euclidean vectors, starting from the origin of the space (initial point).

We applied a 2D Euclidean distance system measurement in this case. The face will be detected using the distance measurement function, which will return the face width as a pixel value. The focal length of the camera is calculated using the pixel value. Finally, we calculated the distance using a reference image. To measure distance, we compare the pixel of the reference picture to the pixel of our acquired image. We need to know the exact size of an item in the image to estimate distance on a real scale. That is why the reference image is being used. If we know the distance between the ground level and the camera on a big scale, we can simply determine the distance. However, if we don't know the reference value, we can't compute the distance using the 2D technique. This is the system's most serious flaw. As a result, we intend to apply the 3D reconstruction approach in our future work.

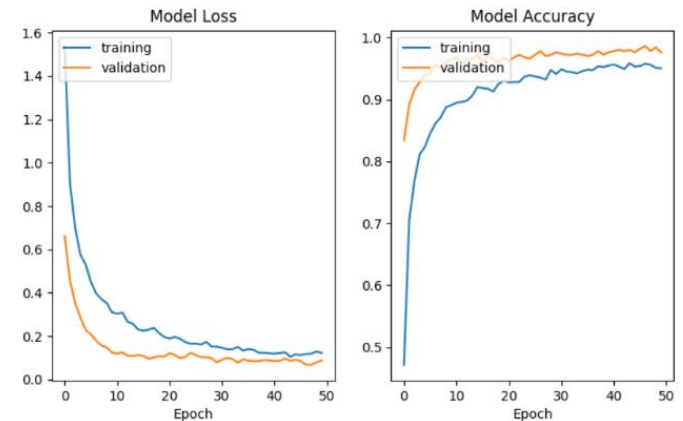


Fig. 3 Model training accuracy and loss curve

## 4 Experimental Results and Discussion

This paper tries to fine-tune using Inception V3 on a dataset containing around ten thousand images in two classes. Initially, we froze all base layers and just trained 2 fully connected layers (2048 units and 3 respectively). The training accuracy went 98 percent in 20 epochs and the validation accuracy is 99.5 percent, as shown in Fig. 3. The model initially detects all people in the cameras and shows a green boundary case around each person who is far from the other. If the minimum distance (threshold) exceeds, which means people violate social distance (SD) norms the color of the box changes to red [21].

In Fig. 4, the child is properly wearing a mask, but still, the bounding box is red because our model not only detects facemask but also measures the social distancing aspects as well and as we can see that part did not maintain properly so that is why the bounding box turned into a red one.



Fig. 4 Visualization of the test results obtained by the proposed system

The model detects the SD and masks with a precision score of 98.2 percent and a recall value of 97.8. The frame rate per second (FPS) was 25.0.

The experiments were conducted on Google Colaboratory with Intel(R) core i5, 1.80 GHz CPU, Virtual TPUv2-8 64 GB, 12GB DDR4 VRAM, and 8 GB RAM. All programs were written in Python - 3.6 and utilized OpenCV - 4.2.0, Keras -2.3.0 and TensorFlow - 2.2.0. We have mentioned different types of models and their accuracy which have been used relatively in this sector in Table 1.

Table 1 Comparison table of other models with details

References	Algorithm	Accuracy	Data
[5]	YOLOv4	99.8	3,762,615
[6]	YOLOv2	D1-95.6% D2-94.5%	1575 (d1-775, d2-800)
[9]	VGG-16	96%	25000
<b>This paper</b>	<b>InceptionV3+ attention</b>	<b>99% to 99.5 %</b>	<b>10800</b>

As we can see many kinds of methodology considered only one safety measurement which was mask detection but our model ensures two of them in the meantime. Most of them have been chosen to go with the YOLO algorithm and its different versions. After comparing the details, we have noticed that another type of the proposed model had obtained 99.8% accuracy with almost 3.5 lakhs dataset, but our dataset only consists of 10800 data, and as we know the inceptionv3 model provides higher accuracy with small datasets [21]. Since the system initially would not have enough data but as it will work in a real-time environment so after the implementation it would be able to collect enormous data. Additionally, the attention mechanism is known for identifying individual small objects more precisely from an image, and as our system needed to find facemasks from a real-time scenario so that is why we had chosen this model for our research purpose and successfully got 99.5% accuracy.

The test accuracy for different algorithms is shown in Fig. 5 and shows the performance of the f1-score for with mask and without mask classification.

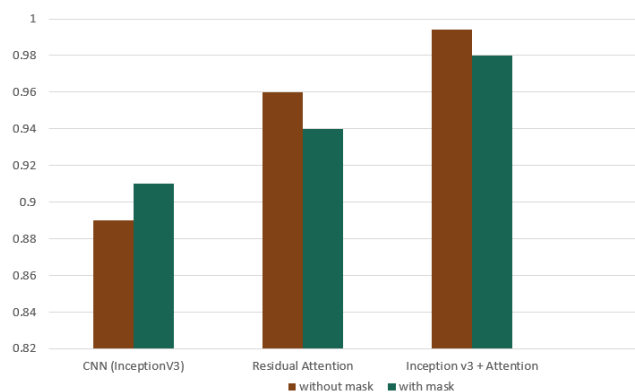


Fig. 5 The f1-score for CNN, attention mechanism, and hybrid inceptionV3+attention model

## 5 Conclusion and Future work

The spread of the contagious COVID-19 virus has created global health crises all over the world, so wearing facemasks and maintaining social distancing are the preliminary precautions. Our model works in real-time so that it has the potential to reduce violations of those two criteria and it can improve the safety of people in the meantime which can reduce the spreading rate of COVID19 all around the globe. By discovering those people who are not wearing masks and not ensuring social distancing, we can ensure that they do so and that is how we can make sure public safety.

We can implement this model in a hardware device for monitoring where the COVID-19 affected people are living the most so that we can ensure that those people are strictly maintaining face masks and social distancing. We can also update another feature where it will detect whether a person is wearing double facemasks, face shields, or not. Besides, one of the common symptoms of COVID-19 is fever and, in our system, we can implement a thermal camera through which we can measure the temperature of a person from a very far distance. We can also use an approach where it will be able to detect if a person is having a breathing problem or not by observing the person's activity. This system cannot only be used for COVID-19 but also it can be used for any kind of infectious disease as well.

## References

- [1] Coronavirus Cases. Available: <https://www.worldometers.info/coronavirus/> (Accessed Sep. 25, 2021).
- [2] A guide to WHO's guidance on COVID-19, 2020. <https://www.who.int/news-room/feature-stories/detail/a-guide-to-who-s-guidance> (Accessed Sep. 25, 2021).
- [3] Jhunjunwala, A., 2020. Role of telecom network to manage COVID-19 in India: Aarogya Setu. *Transactions of the Indian National Academy of Engineering*, 5(2), pp.157-161.
- [4] Xin, T., Guo, B., Wang, Z., Wang, P., Lam, J.C.K., Li, V. and Yu, Z., 2018. Freesense: a robust approach for indoor human detection using wi-fi signals. *Proceedings of the ACM on Interactive, Mobile, Wearable and Ubiquitous Technologies*, 2(3), pp.1-23.
- [5] R. Karim, "Illustrated: 10 CNN Architectures," 2019. <https://towardsdatascience.com/illustrated-10-cnn-architectures-95d78ace614d> (Accessed Sep. 25, 2021).

- [6] Rezaei, M. and Azarmi, M., 2020. Deepsocial: Social distancing monitoring and infection risk assessment in covid-19 pandemic. *Applied Sciences*, 10(21), p.7514.
- [7] Saponara, S., Elhanashi, A. and Gagliardi, A., 2021. Implementing a real-time, AI-based, people detection and social distancing measuring system for Covid-19. *Journal of Real-Time Image Processing*, 18(6), pp.1937-1947.
- [8] Vinh, T.Q. and Anh, N.T.N., 2020, November. Real-Time Face Mask Detector Using YOLOv3 Algorithm and Haar Cascade Classifier. In *2020 International Conference on Advanced Computing and Applications (ACOMP)* (pp. 146-149). IEEE.
- [9] Jiang, X., Gao, T., Zhu, Z. and Zhao, Y., 2021. Real-time face mask detection method based on YOLOv3. *Electronics*, 10(7), p.837.
- [10] Hou, Y.C., Baharuddin, M.Z., Yussof, S. and Dzulkifly, S., 2020, August. Social distancing detection with deep learning model. In *2020 8th International Conference on Information Technology and Multimedia (ICIMU)* (pp. 334-338). IEEE.
- [11] Martinez, M., Yang, K., Constantinescu, A. and Stiefelwagen, R., 2020. Helping the blind to get through COVID-19: Social distancing assistant using real-time semantic segmentation on RGB-D video. *Sensors*, 20(18), p.5202.
- [12] Militante, S.V. and Dionisio, N.V., 2020, August. Real-time facemask recognition with alarm system using deep learning. In *2020 11th IEEE Control and System Graduate Research Colloquium (ICSGRC)* (pp. 106-110). IEEE.
- [13] Krishna, K.P. and Harshita, S., 2021, Social Distancing and Face Mask Detection Using Deep Learning. 6(6), pp. 114–120.
- [14] Milton-Barker, A., 2019. Inception V3 Deep Convolutional Architecture For Classifying Acute Myeloid/Lymphoblastic Leukemia. *Intel*. Available: <https://software.intel.com/content/www/us/en/develop/articles/inception-v3-deep-convolutional-architecture-for-classifying-acute-myeloidlymphoblastic.html> (Accessed Jun. 02, 2021).
- [15] Tristan, Visual Attention Model in Deep Learning. Available: <https://towardsdatascience.com/visual-attention-model-in-deep-learning-708813c2912c?fbclid=IwAR144qRT028EzciqcCWVM DZ90A5KB23JoudhlEjKi4Hoywo8MJ8Xk8hyWA0>.
- [16] “Mask Dataset,” 2020. Available: <https://makeml.app/datasets/mask> (Accessed Jun. 02, 2021).
- [17] “bing-image-downloader,” 2021. <https://pypi.org/project/bing-image-downloader/> (Accessed Jun. 02, 2021).
- [18] Das, A.K., Al Asif, A., Paul, A. and Hossain, M.N., 2021. Bangla hate speech detection on social media using attention-based recurrent neural network. *Journal of Intelligent Systems*, 30(1), pp.578-591.
- [19] Ansari, M. and Singh, D.K., 2021. Monitoring social distancing through human detection for preventing/reducing COVID spread. *International Journal of Information Technology*, 13(3), pp.1255-1264.
- [20] Gupta, S., Kapil, R., Kanahasabai, G., Joshi, S.S. and Joshi, A.S., 2020, September. SD-measure: a social distancing detector. In *2020 12th International Conference on Computational Intelligence and Communication Networks (CICN)* (pp. 306-311). IEEE.
- [21] Yadav, S., 2020. Deep learning based safe social distancing and face mask detection in public areas for covid-19 safety guidelines adherence. *International Journal for Research in Applied Science and Engineering Technology*, 8(7), pp.1368-1375.

# The Decolorization and Phytotoxic Efficiency of Jackfruit Seed on a Textile Dye Novacron Blue

Rafi Ahmed Miah<sup>1</sup>, Mohammad Jahangir Alam<sup>1</sup>, Aklima Khatun<sup>2</sup>, Mahmudul Hassan Suhag<sup>1,2</sup> and Md. Nazmul Kayes<sup>1\*</sup>

<sup>1</sup>Department of Chemistry, University of Barishal, Barishal-8254, Bangladesh

<sup>2</sup>Department of Chemistry for Materials, Mie University, Mie 514-8507, Japan

Received: January 17, 2022, Revised: March 13, 2022, Accepted: March 13, 2022, Available Online: March 15, 2022

## ABSTRACT

Industrial wastewater containing dye can cause severe destruction to the human immune system as well as the nervous system. The purpose of the present study is to optimize the decolorization of a textile dye Novacron blue on the surface of jackfruit seed powder (JSP). Jackfruit seed can be obtained at a low cost and be used without further purification/chemical treatment to adsorb some pollutants on its surface. About 73% of Novacron blue was adsorbed on the surface of JSP after 60 minutes of contact time. Effects of various physico-chemical parameters such as adsorbent dose, initial dye concentration, pH, temperature, and contact time on the adsorption of Novacron blue have been investigated. The adsorption was found to be increased initially with the adsorbent dose and become maximum at 10 g of the adsorbent. The maximum adsorption capacity was 0.732 mg/g. The decolorization efficiency was inversely proportional to the initial concentration of Novacron blue. Basic medium and low temperature are preferred by the adsorbent for the adsorption of Novacron blue on JSP. Kinetics of adsorption was accomplished with the pseudo-first-order and pseudo-second-order model. Phytotoxic study on Red Amaranth reveals the abolishment of hazardous species from the wastewater.

Keywords: Adsorption, Bio-adsorbent, Decolorization, Jackfruit Seed, Phytotoxic Efficiency.



This work is licensed under a [Creative Commons Attribution-Non Commercial 4.0 International License](https://creativecommons.org/licenses/by-nc/4.0/).

## 1 Introduction

Dyes are aromatic synthetic compounds that are colorants and water-soluble. These are used as raw materials in various industries such as leather, paper, pulp, paint, cosmetics, printing, textile, etc [1]. Dye is one of the hazardous and abundant water pollutants among the various organic compounds [2]. The textile industry utilizes over  $7 \times 10^5$  tones and about 10000 different dyes and pigments per year [3]. Improper discharge of industrial dye effluent causes severe damage to the environment. These are visually unpleasant in the aqueous environment and cause a reduction in sunlight and oxygen penetration by their high turbidity. For this reason, photosynthetic activity, dissolved oxygen concentration as well as water quality is decreased. In addition dye molecules increase the total organic carbon (TOC) and decrease the chemical oxygen demand (COD) and biological oxygen demand (BOD) in the water system. Furthermore, several reports indicate that textile dyes and effluents have toxic effects on the germination rates and biomass of several plant species which have important ecological functions [2],[4]-[6].

So, the treatment of effluent-containing textile dye is crucial before their final discharge to the environment to protect aquatic life and public health. Numerous methods like ozonation, photo-oxidation, electrocoagulation, froth flotation, reverse osmosis, ion exchange, membrane filtration, flocculation, and adsorption by activated carbon are applied for color removal from effluents containing textile dye [2],[7]-[9]. Adsorption is widely used for the removal of wastewater due to the ease of its operation and cost-effectiveness. But the use of commercially available activated carbon/chemicals as adsorbents is expensive for their manufacturing and regeneration costs [10]. Using biological materials as adsorbents is found to be superior to other techniques for its cost-effectiveness, higher efficiency, less

sludge production, minimal requirement for chemicals, etc. Some cost-effective bio-adsorbents such as rice husk, sawdust, orange peel, water hyacinth, peanut hull, pomegranate seed, neem leaf powder, wheat straw, apple pomace, de-oiled soya, palm ash, aloe vera leaf, durian peels, banana peel and have been used for removal of dye from wastewater containing industrial effluent [2],[7]-[8],[11]-[24]. For instance, the decolorization of crystal violet (91.1%) and methylene blue (83.6%) by seed powder of *Punica granatum* L at neutral pH have been reported [24]. The maximum adsorption capacity of Jackfruit seed on Rhodamine B was found to be 26.4 and 37.9 mg/g, respectively by Langmuir and Sips models prediction [25]. The maximum adsorption capacity of Jackfruit leaf powder on methylene blue is 326.32 mg/g [1]. It has been the maximum uptake capacity of Congo red dye by Aloe vera leaves shell was 1850 mg/g [11]. Decolorization of Novacron blue has been studied by electrochemical degradation [26], TiO<sub>2</sub>/palygorskite nanocomposite photocatalyst [27], *Bacillus badius*, and *Bacillus sphaericus* bacteria [28]. The instrumental setup for the electrochemical degradation and synthesis of TiO<sub>2</sub>/palygorskite nanocomposite is a cost-intensive method. On the other hand, there is a huge risk of propagation of bacteria in the laboratory which may cause epidemic diseases.

Polyaniline emeraldine salt was synthesized by polymerization technique in presence of an oxidizing agent ammonium persulfate. The synthesized salt was used as an adsorbent to remove Novacron Blue ECR from the aqueous solution. About 88% of Novacron blue ECR dye was removed at optimized conditions after 80 minutes of contact time [29]. The removal efficiency of Novacron blue 4R by the adsorption on the surface of activated carbon was studied both theoretically and experimentally. The removal efficiency was found 96.24% and 93.63%, respectively at optimized conditions [30].

Removal of dye from wastewater by adsorption technique especially with the bio-adsorbent is a cost-effective and less hazardous method in comparison to the others. Novacron blue is an azo dye having high water solubility, which is used abundantly in different textile industries of Bangladesh. The availability of jackfruit as well as jackfruit seeds in Bangladesh is very high and can be collected at a cheap rate. That is why, in the present study, the jackfruit seed powder (JSP) was used as an adsorbent to decolorize the textile dye Novacron blue. The decolorization efficacy was monitored by a UV-Visible spectrophotometer. The adsorption of Novacron blue was investigated at various physico-chemical parameters such as different amounts of adsorbent, initial dye concentration, initial pH, initial temperature, and contact time. The Phytotoxic effect was also studied under Novacron blue solution and decolorized solution.

## 2 Materials and Methods

### 2.1 Chemicals, Reagents, and Instruments

Jackfruit seeds were collected from the local area of Barishal, Bangladesh. A textile dye Novacron blue was collected from a textile industry of Gazipur, Bangladesh. Deionized water was used as a reference in a UV-visible spectrophotometer. Ethanol and acetone were used to clean the glass apparatus used in the present study. All reagents and solvents were purchased from Merck, Germany, and used for the study without further purification. Adsorption was carried out in an orbital shaker (Model No-JSOS-300) and the decolorization was monitored by a UV-Visible spectrophotometer (Lamda-365) at 200 - 800 nm.

### 2.2 Preparation of Adsorbent

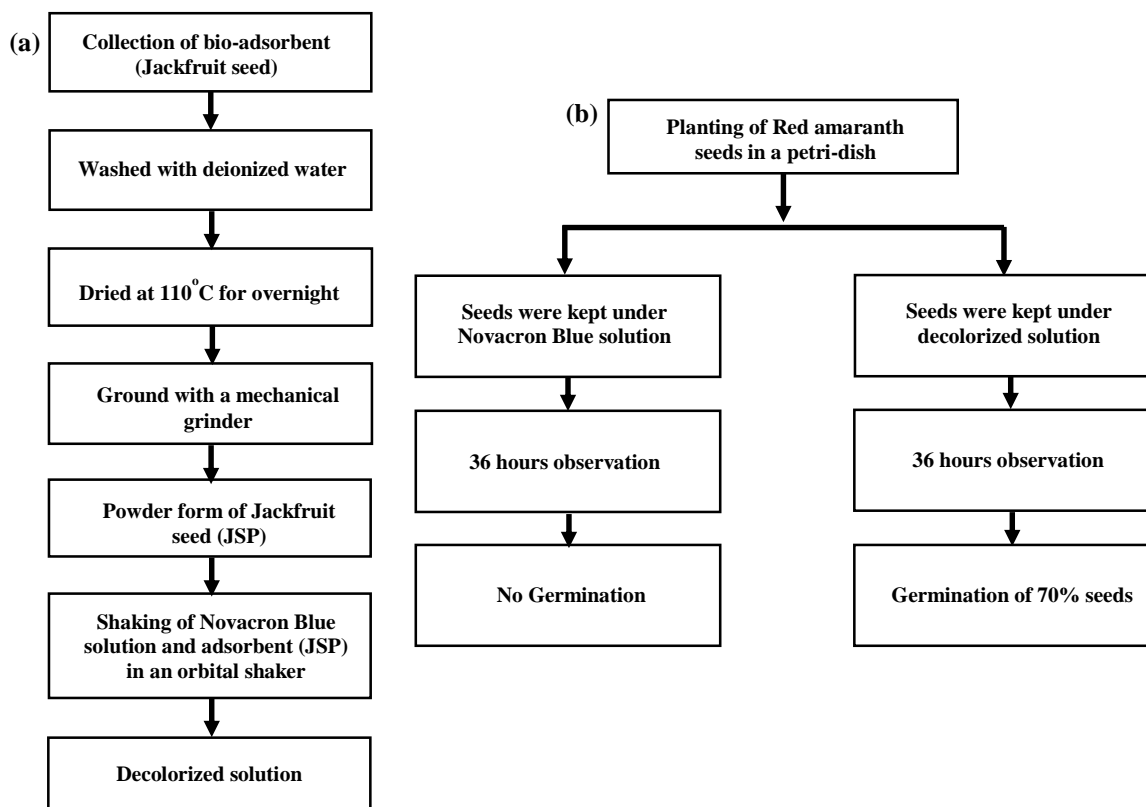


Fig. 1 A schematic representation for the (a) decolorization and (b) phytotoxic study of Novacron blue dye by JSP.

Jackfruit seeds were washed with distilled water to remove the surface adhered particles and water-soluble materials. Then washed jackfruit seeds were heated in an oven at 110°C overnight. The dried seeds were ground with a grinder to make powder. The ground powders were sieved manually.

### 2.3 Preparation of Dye Solutions

500 ppm of an aqueous solution of Novacron blue was prepared in 500 mL of volumetric flask and kept as a stock solution. Solutions of different concentrations were prepared from stock solution by appropriate dilution.

### 2.4 Decolorization Study

A definite amount of JSP was added to a solution of Novacron blue and shaken with an orbital shaker at 210 rpm of agitation rate. About 2-3 mL solution was collected after a definite time interval and centrifuged at 200 rpm for 10 minutes. The baseline correction of the UV-Visible spectrophotometer was carried out by using deionized water which was used as a reference. After that absorption of the clear dye solution was measured at  $\lambda_{\max} = 602$  nm wavelength by UV-Visible spectrophotometer. A schematic representation for the whole process is shown in Fig. 1.

Percentage of decolorization of Novacron blue by JSP was determined by the following equation:

$$\text{Decolorization (\%)} = \frac{A_0 - A_t}{A_0} \times 100$$

where,  $A_0$  and  $A_t$  are initial and final absorbance of Novacron blue solution, respectively.

## 2.5 Decolorization Study of Novacron Blue by Various Physicochemical Parameters

### 2.5.1 Decolorization by JSP

Decolorization was studied with various adsorbent doses (0.5 g - 12.0 g of JSP) at a fixed concentration (100 ppm), different dye concentrations (50 - 250 ppm) with a fixed amount of JSP (10 g). The effect of temperature (25°C - 60°C) and pH (4.3 - 8.4) on decolorization was also investigated. The volume of Novacron blue solution was kept at 100 mL to carry out all the experiments. The decolorization of 100 mL of Novacron blue (100 ppm) by JSP (10 g) was also investigated at different time intervals up to 2.5 hours. Effects of all the physicochemical parameters on decolorization were monitored with the UV-visible spectrophotometer.

### 2.5.2 Phytotoxic Study by Germination Process

Phytotoxicity of decolorized dye solution and initial dye solution was tested by using a few seeds of Red Amaranth (*Amaranthus cruentus*). These three solutions with 10 seeds of Red Amaranth were taken in two Petri dishes separately for 36 hours. After 36 hours percent of germination was observed in each solution by using the following equations [31]-[32]:

$$\text{Germination (\%)} = \frac{\text{Number of seeds germinated}}{\text{Total number of seeds set for test}} \times 100$$

## 3 Results and Discussion

### 3.1 Effect of Amount of Adsorbent

The decolorization of Novacron blue was increased with the increasing amount of JSP and reaches a constant level after a certain amount. The degree of decolorization of dye increased from 2% to 68% as the amount of JSP increased from 0.5 to 10.0 g and then remain constant (Fig. 2). With the increase of adsorbent dosage, the surface area of the adsorbent increases, which also increases the number of available sites for adsorption. In addition, the decolorization remains constant after 10.0 g of JSP is due to the saturation of adsorption sites [33]-[34].

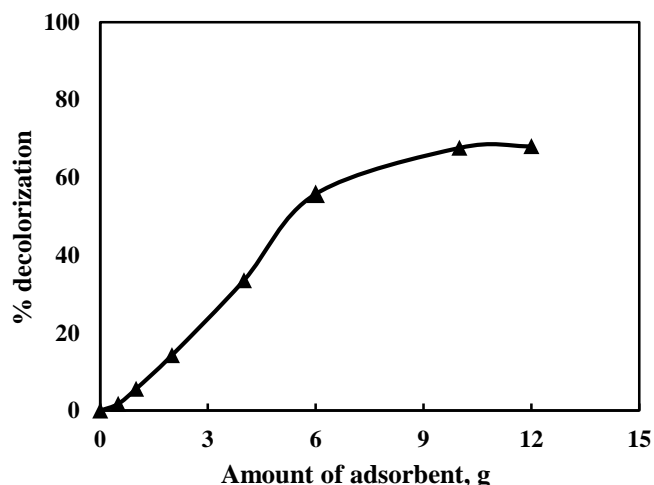


Fig. 2 Percentage of decolorization of Novacron blue at different amount of adsorbents.

### 3.2 Effect of Initial Concentration of Novacron Blue

It was observed that decolorization of Novacron blue by JSP was decreased from 67% to 51% with the increase in the initial concentration of dye from 50 to 250 ppm (Fig. 3). At a lower

concentration, molecules have available binding sites on JSP, which results in better adsorption or decolorization of dye. The number of adsorbate molecules increases at high concentrations but the number of sites on the surface of the adsorbent is fixed. As a result, the number of available binding sites on JSP for the adsorbate molecule becomes limited at higher concentrations and the adsorption rate is found to be decreased [34]-[35].

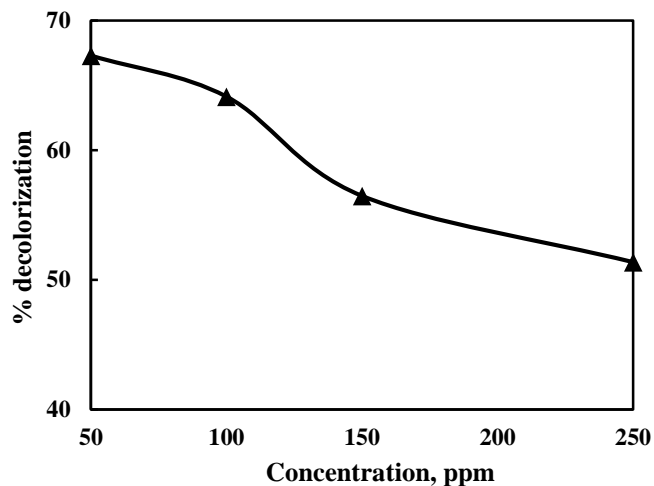


Fig. 3 Effect of initial concentration of Novacron blue on the decolorization.

### 3.3 Effect of pH

The percentage of decolorization was increased with the increase of pH from 4.3 to 8.4. The efficiency was increased from 66% to 68% after 30 minutes of contact time. In the acidic media, there is a competition between the cation of dye and the excess H<sup>+</sup> ion present in the solution to adsorb on the surface sites. As a result, the amount of adsorption on the surface of adsorbents is lower. On the contrary, the number of negatively charged sites is higher than the number of positively charged sites at the basic medium. So, there is an electrostatic attraction between the negatively charged sites and the dye cation which increases the amount of adsorption [36] (Fig. 4).

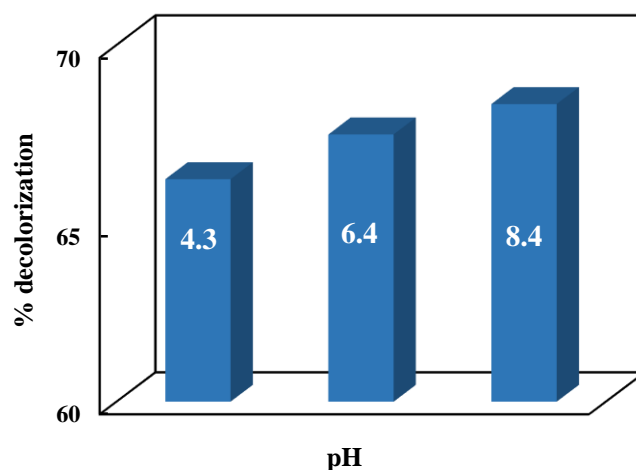


Fig. 4 Effect of pH on the decolorization of Novacron blue by the adsorbents.

### 3.4 Effect of Temperature

It was observed that decolorization of Novacron blue was decreased by JSP with the increase of temperature (Fig. 5) which

indicates the exothermic nature of the adsorption. The percentage of decolorization was decreased from 67% to 59% after 30 minutes of contact time with the increase of temperature from 25°C to 60°C. The decrease in decolorization with temperature may be occurred due to the decreased active sites of the adsorbent at high temperatures [37]-[38].

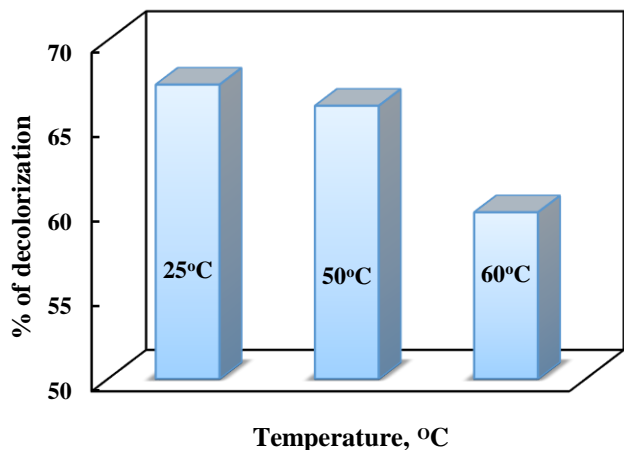


Fig. 5 Percentage of decolorization of Novacron blue by JSP at different temperatures.

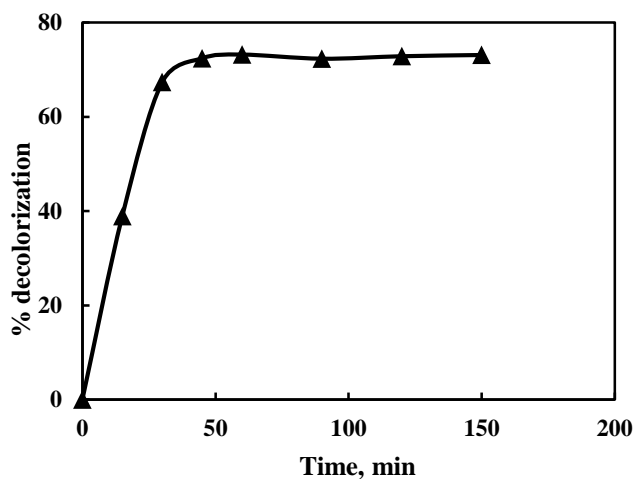


Fig. 6 Percentage of decolorization of Novacron blue at different contact times.

### 3.5 Effect of Contact Time

There is a rapid increase in the percentage of decolorization of Novacron blue with the increase of contact time as seen in Fig. 6. The percentage of decolorization became almost constant/slightly decreased after the adsorption of 60 minutes. The quick decolorization might be attributed to a large number of surface sites of adsorbent for adsorption at the initial stages but after a certain period of time, all the surface sites of the adsorbent become saturated [37],[39]. The surface sites of JSP for adsorption could be fully occupied after 60 minutes. At this stage, an equilibrium is established between the adsorbate and adsorbent. After that, desorption may take place [40].

### 3.6 Kinetic studies

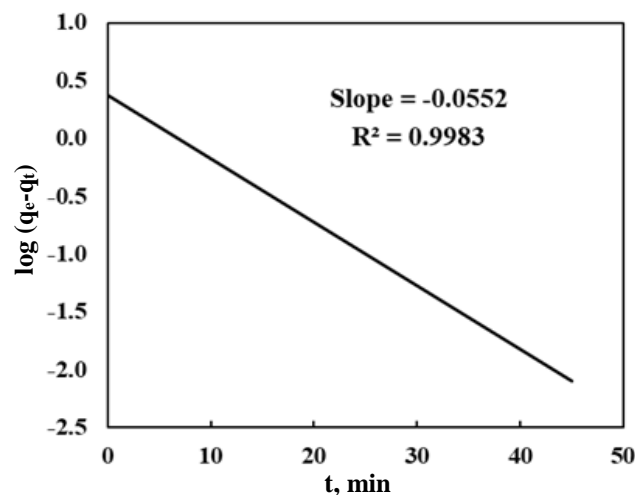
The mechanism and kinetics of adsorption of Novacron blue on the surface of JSP can be obtained by fitting the experimental data to some kinetic models (pseudo-first-order, pseudo-second-

order). The kinetic equations for the pseudo-first and pseudo-second-order models are as follows [41]-[42].

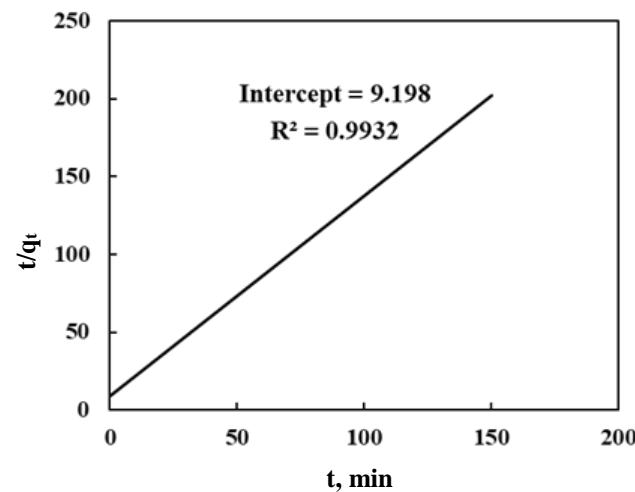
$$\log(q_e - q_t) = \log q_e - k_1 t \tag{1}$$

$$t/q_t = 1/(k_2 q_e^2) + t/q_e \tag{2}$$

where  $q_e$  and  $q_t$  are the amount of adsorbate adsorbed on adsorbent (mg/g) at equilibrium and any time  $t$  respectively.  $k_1$  and  $k_2$  are the corresponding rate constants for the pseudo-first and second-order reactions.



(a)



(b)

Fig. 7 (a) Pseudo-first order and (b) Pseudo-second order kinetic model for the adsorption of Novacron blue on JSP respectively.

The value of  $q_e$  and  $q_t$  are calculated by using the following equations [43]

$$q_t = (C_0 - C_t) V/W \tag{3}$$

$$q_e = (C_0 - C_e) V/W \tag{4}$$

where,  $C_0$ ,  $C_t$  and  $C_e$  represent the initial concentration, concentration at any time  $t$ , and equilibrium concentration of dye in mg/L respectively.  $V$  is the volume of the solution (L) used for adsorption and  $W$  is the mass of dry adsorbent (g).

All the kinetic parameters are evaluated separately from the plot of  $\log(q_e - q_t)$  vs.  $\log q_e$  and  $t/q_t$  vs.  $t$  (Fig. 7). The value of rate constants, maximum adsorption capacity, and correlation coefficient ( $R^2$ ) are listed in Table 1. The value of  $R^2$  suggests that the adsorption on JSP follows pseudo-first-order kinetics.

Table 1 Kinetic parameters for the pseudo-first and pseudo-second order models.

JSP				
$q_e$	Pseudo-first-order		Pseudo-second-order	
mg/g	$k_1$	$R^2$	$k_2$	$R^2$
0.732	0.0552	0.9983	0.2029	0.9932

### 3.7 Phytotoxicity by Germination

Phytotoxic effect on Red Amaranth (*Amaranthus cruentus*) by Novacron blue and decolorized dye solutions have been explored in Fig. 8 and Table 2. A significant phytotoxic effect on Red Amaranth (*Amaranthus cruentus*) by the decolorized dye solution of Novacron blue was observed, which reveals the efficiency of JSP as a bio-adsorbent.

Table 2 Germination of Red Amaranth seeds at different conditions.

Germination condition	% of seeds germinated
Novacron blue solution	0%
Decolorized Novacron blue by JSP	70%

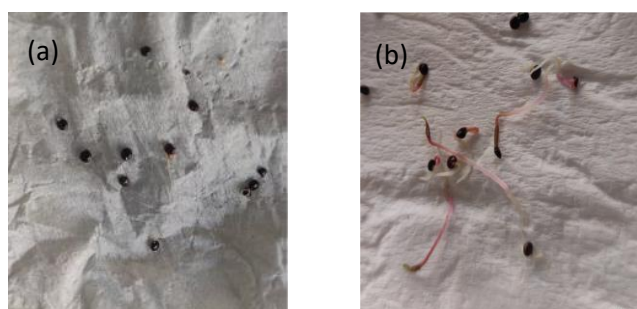


Fig. 8 Phytotoxic effect of (a) Novacron blue solution and (b) decolorized solution of Novacron blue.

## 4 Conclusion

Jackfruit seeds showed good decolorization efficiency to Novacron blue through the adsorption process. The adsorption efficiency of JSP was transformed with the change of various physicochemical parameters. The maximum adsorption capacity of JSP in removing the Novacron blue dye from wastewater is better than some other previously reported research. The adsorption on JSP is found to follow pseudo-first-order kinetics. The phytotoxic effect of dye solution is significantly changed after decolorization. The percentage of adsorption was better at basic medium and low temperatures. The unconcerned dumping of agricultural wastage to the environment may cause a severe problem which can be reduced by their use as an adsorbent in removing contaminants from wastewater. Bangladesh is one of the world's biggest garment manufacturing countries and that is why wastewater is commonly dumped directly into rivers and streams without any treatment. The main reason behind this

problem is the existing expensive methods for wastewater treatment. A low-cost adsorbent and inexpensive industrial setup may be a fruitful solution to this problem. It is expected that the above findings in the present research will make the JSP a potential candidate to use as an adsorbent in removing pollutants from wastewater.

## Acknowledgment

We would like to thank the University of Barishal as well as the University Grant Commission (UGC), Bangladesh for the financial support.

## References

- [1] Uddin, M., Rukanuzzaman, M., Khan, M., Rahman, M. and Islam, M., 2009. Jackfruit (*Artocarpus heterophyllus*) leaf powder: An effective adsorbent for removal of methylene blue from aqueous solutions. *Indian Journal of Chemical Technology*, 16, pp. 142–149.
- [2] Shah, J., Rasul Jan, M., Haq, A. and Khan, Y., 2013. Removal of Rhodamine B from aqueous solutions and wastewater by walnut shells: kinetics, equilibrium and thermodynamics studies. *Frontiers of Chemical Science and Engineering*, 7(4), pp.428-436.
- [3] Joseph, N.T., Chinonye, O.E., Philomena, I.K., Christian, A.C. and Elijah, O.C., 2016. Isotherm and kinetic modeling of adsorption of dyestuffs onto kola nut (*Cola acuminata*) shell activated carbon. *Journal of Chemical Technology and Metallurgy*, 51(2), pp. 188-201.
- [4] Yagub, M.T., Sen, T.K., Afroze, S. and Ang, H.M., 2014. Dye and its removal from aqueous solution by adsorption: a review. *Advances in Colloid and Interface Science*, 209, pp.172-184.
- [5] Mittal, A., Mittal, J., Malviya, A., Kaur, D. and Gupta, V.K., 2010. Decoloration treatment of a hazardous triarylmethane dye, Light Green SF (Yellowish) by waste material adsorbents. *Journal of Colloid and Interface Science*, 342(2), pp.518-527.
- [6] Saratale, R.G., Saratale, G.D., Chang, J.S. and Govindwar, S.P., 2011. Bacterial decolorization and degradation of azo dyes: A review. *Journal of the Taiwan Institute of Chemical Engineers*, 42(1), pp. 138-157.
- [7] Murugan, T., Ganapathi, A. and Valliappan, R., 2010. Removal of dyes from aqueous solution by adsorption on biomass of mango (*Mangifera indica*) leaves. *E-Journal of Chemistry*, 7(3), pp. 669-676.
- [8] Thakur, A. and Kaur, H., 2017. Response surface optimization of Rhodamine B dye removal using paper industry waste as adsorbent. *International Journal of Industrial Chemistry*, 8, pp. 175-186.
- [9] Kumar, B. and Kumar, U., 2014. Removal of Malachite Green and Crystal Violet Dyes from Aqueous Solution with Bio-Materials: A Review. *Global Journal of Researches in Engineering*, 14(4), pp. 50-60.
- [10] Mohammed, M.A., Shitu, A. and Ibrahim, A., 2014. Removal of Methylene Blue Using Low Cost Adsorbent: A Review. *Research Journal of Chemical Sciences*, 4, pp. 91-102.
- [11] Khaniabadi, Y.O., Mohammadi, M.J., Shegerd, M., Sadeghi, S., Saedi, S. and Basiri, H., 2017. Removal of Congo red dye from aqueous solutions by a low-cost adsorbent: activated carbon prepared from Aloe vera leaves shell. *Environmental Health Engineering Management Journal*, 4, pp. 29-35.
- [12] Daouda, A., Honorine, A.T., Bertrand, N.G., Richard, D. and Domga, 2019. Adsorption of Rhodamine B onto Orange Peel Powder. *American Journal of Chemistry*, 9(5), pp. 142-149.
- [13] Thakur, A. and Kaur, H., 2016. Removal of hazardous Rhodamine B dye by using chemically activated low cost

- adsorbent: Pine cone charcoal. *International Journal of Chemical and Physical Sciences*, 5(4), pp. 17-28.
- [14] Hameed, B.H. and El-Khaiary, M.I., 2008. Malachite green adsorption by rattan sawdust: Isotherm, kinetic and mechanism modeling. *Journal of Hazardous Materials*, 159, pp. 574-579.
- [15] Banat, F., Al-Asheh, S. and Al-Makhadmeh, L., 2003. Evaluation of the use of raw and activated date pits as potential adsorbents for dye containing waters. *Process Biochemistry*, 39, pp. 193-202.
- [16] Gong, R., Li, M., Yang, C., Sun, Y. and Chen, J., 2005. Removal of cationic dyes from aqueous solution by adsorption on peanut hull. *Journal of Hazardous Materials*, 121, pp. 247-250.
- [17] Bhattacharya, K.G. and Sharma, A., 2005. Kinetics and thermodynamics of Methylene Blue adsorption on Neem (*Azadirachta indica*) leaf powder. *Dyes and Pigments*, 65, pp. 51-59.
- [18] Vadivelan, V. and Vasanth Kumar, K., 2005. Equilibrium, kinetics, mechanism, and process design for the sorption of methylene blue onto rice husk. *Journal of Colloid and Interface Science*, 286, pp. 90-100.
- [19] Nassar, M.M., Hamoda, M.F. and Radwan, G.H., 1995. Adsorption equilibria of basic dyestuff onto palm-fruit bunch particles. *Water Science and Technology*, 32, pp. 27-32.
- [20] Ponnusamy, S.K. and Subramaniam, R., 2013. Process optimization studies of Congo red dye adsorption onto cashew nut shell using response surface methodology. *International Journal of Industrial Chemistry*, 4(1), pp.1-10.
- [21] Garg, V.K., Gupta, R., Yadav, A.B. and Kumar, R., 2003. Dye removal from aqueous solution by adsorption on treated sawdust. *Bioresource Technology*, 89(2), pp. 121-124.
- [22] Robinson, T., Chandran, B. and Nigam, P., 2002. Removal of dyes from a synthetic textile dye effluent by biosorption on apple pomace and wheat straw. *Water Research*, 36, pp. 2824-2830.
- [23] Namasivayam, C., Radhika, R. and Suba, S., 2001. Uptake of dyes by a promising locally available agricultural solid waste: Coir pith. *Waste Management*, 21, pp. 381-387.
- [24] Uddin, M.K. and Nasar, A., 2020. Decolorization of Basic Dyes Solution by Utilizing Fruit Seed Powder. *KSCE Journal of Civil Engineering*, 24, pp. 345-355.
- [25] Kooh, M.R.R., Dahri, M.K. and Lim, L.B.L., 2016. Jackfruit seed as a sustainable adsorbent for the removal of Rhodamine B dye. *Journal of Environment and Biotechnology Research*, 4, pp. 7-16.
- [26] Rocha, J.H.B., Solano, A.M.S., Fernandes, N.S., da Silva, D.R., Peralta-Hernandez, J.M. and Martínez-Huitle, C.A., 2012. Electrochemical Degradation of Remazol Red BR and Novacron Blue C-D Dyes Using Diamond Electrode. *Electrocatalysis*, 3, pp. 1-12.
- [27] Assis, M.L.M. de, Junior, E.D., Almeida, J.M.F. de, Silva, I. do N., Barbosa, R.V., Santos, L.M. dos, Dias, E.F., Fernandes, N.S. and Martínez-huitle, C.A., 2021. Photocatalytic degradation of Novacron blue and Novacron yellow textile dyes by the TiO<sub>2</sub>/palygorskite nanocomposite. *Environmental Science and Pollution Research*, 28, pp. 64440-64460.
- [28] Mahbub, K.R., Morium, B., Ahmed, M.M., Akond, M.A. and Andrews, S., 2015. Decolorization of Novacron Blue and Novacron Super Black Azo Dyes by *Bacillus* spp Isolated from Textile Effluents in Bangladesh. *Journal of Scientific Research*, 7, pp. 45-53.
- [29] Lingeswari, U.D., Vimala, T., 2019. Kinetics and isotherm study of adsorption of industrial dyes Novacron Blue ECR and Reactive Yellow 145 by PANI-Emeraldine salt. *International Journal of Research and Analytical Reviews*, 6, pp. 698-705.
- [30] Barrak, N., Mannai, R., Zaidi, M., Achour, S., Kechida, M., Helal, A.N., 2018. Optimization of Novacron Blue 4R (NB4R) removal by adsorption process on activated carbon using response surface methodology. *Desalination and Water Treatment*, 104, pp. 346-353.
- [31] Vibhuti, Shahi, C., Bargali, K. and Bargali, S.S., 2015. Seed germination and seedling growth parameters of rice (*Oryza sativa*) varieties as affected by salt and water stress. *Indian Journal of Agricultural Sciences*, 85, pp. 102-108.
- [32] Rahman, A., Rahman, S., Mohiuddin, K.M., Chowdhury, A.H. and Chowdhury, A.K., 2019. Germination and seedling growth of rice (*Oryza sativa* L.) as affected by varying concentrations of loom- dye effluent. *Journal of the Bangladesh Agricultural University*, 17, pp. 153-160.
- [33] Badii, K., Ardejani, F.D., Saberi, M.A., Limaee, N.Y. and Shafaei, S.Z., 2010. Adsorption of Acid blue 25 dye on diatomite in aqueous solutions. *Indian Journal of Chemical Technology*, 17, pp. 7-16.
- [34] Satish, P., Renukdas, S. and Patel, N., 2011. Removal of Methylene Blue, a Basic Dye from Aqueous Solutions by Adsorption Using Teak Tree (*Tectona Grandis*) Bark Powder. *International Journal of Environmental Sciences*, 1(5), pp. 711-726.
- [35] El Qada, E., 2020. Kinetic Behavior of the Adsorption of Malachite Green Using Jordanian Diatomite as Adsorbent. *Jordanian Journal of Engineering and Chemical Industries*, 3(1), pp. 1-10.
- [36] Batzias, F.A. and Sidiras, D.K., 2007. Simulation of dye adsorption by beech sawdust as affected by pH. *Journal of Hazardous Materials*, 141, pp. 668-679.
- [37] Khan, T.A., Sharma, S. and Ali, I., 2011. Adsorption of Rhodamine B dye from aqueous solution onto acid activated mango (*Mangifera indica*) leaf powder: Equilibrium, kinetic and thermodynamic studies. *Journal of Toxicology and Environmental Health Sciences*, 3, pp. 286-297.
- [38] Omar, H., El-Gendy, A. and Al-Ahmary, K., 2018. Bioremoval of toxic dye by using different marine macroalgae. *Turkish Journal of Botany*, 42, pp. 15-27.
- [39] Umpuch, C., 2015. Removal of yellow 20 dye from aqueous solution using organo-rice straw: Characteristic, kinetic and equilibrium studies. *Engineering Journal*, 19(2), pp. 59-69.
- [40] Kayes, M.N., Chowdhury, M.M.R., Seikh, M.A., Suhag, M.H. and Akter, F., 2019. Application of sugarcane bagasse as an adsorbent for treatment of a textile dye Rhodamine B. *Barishal University Journal Part 1*, 6, pp. 47-57.
- [41] Tseng, R.L., Wu, F.C and Juang, R.S., 2010. Characteristics and Applications of the Lagergren's First-Order Equation for Adsorption Kinetics. *Journal of the Taiwan Institute of Chemical Engineers*, 41, pp. 661-669.
- [42] Fytianos K., Voudrias E. and Kokkalis E., 2000. Sorption-desorption behaviour of 2,4-dichlorophenol by marine sediments. *Chemosphere*, 40(1), pp. 3-6.
- [43] Vijayakumar G., Tamilarasan R. and Dharmendirakumar M., 2012. Adsorption, Kinetic, Equilibrium and Thermodynamic studies on the removal of basic dye Rhodamine-B from aqueous solution by the use of natural adsorbent perlite. *Journal of Materials and Environmental Science*, 3(1), pp. 157-170.

# Evaluation of Different Turbulence Models at Low Reynolds Number for the Flow over Symmetric and Cambered Airfoils

Tafsirul Hassan\*, Md. Tazul Islam, Md. Mizanur Rahman, Abu Raihan Ibna Ali, Asif Al Zayan

Department of Mechanical Engineering, Chittagong University of Engineering & Technology, Chattogram-4349, Bangladesh

Received: February 13, 2022, Revised: March 16, 2022, Accepted: March 16, 2022, Available Online: March 18, 2022

## ABSTRACT

This paper presents an evaluation of five different turbulence models by comparing the numerical data derived from these models using ANSYS Fluent with experimental data at a Reynolds number and a Mach number of  $0.05 \times 10^6$  and 0.015 respectively based on the centerline chord of the airfoil for the flow over NACA 0012 and NACA 2412 airfoils. Moreover, the aim of the present study is to demonstrate the difference in aerodynamic characteristics of the airfoils in order to find aerodynamically more advantageous airfoil. It is concluded that Spalart-Allmaras model and  $k-\omega$  SST model are capable of providing the most accurate prediction for lift coefficient at a low angle of attack for both airfoils. Standard  $k-\epsilon$  model gives a slightly low value of lift coefficient at low angle of attack and slightly high value of lift coefficient at high angle of attack for both airfoils.  $k-\omega$  SST model, Spalart-Allmaras model, Transition  $k-k_L-\omega$  model, and  $\gamma-Re_{\theta}$  Transition SST model can predict drag coefficient reasonably at low angle of attack. At a high angle of attack, however, no turbulence model is able to give a satisfactory prediction for lift coefficient as well as drag coefficient, which implies that these models are unable to predict post-stall characteristics. NACA 2412 airfoil produces more lift coefficient than that of the NACA 0012 airfoil at all angles of attack. Moreover, the drag coefficient of NACA 2412 airfoil is less than that of the NACA 0012 airfoil, which implies that NACA 2412 airfoil exhibits better aerodynamic performance. The lift to drag coefficient ratio of NACA 2412 airfoil is also higher than that of the NACA 0012 airfoil indicating NACA 2412 airfoil to be more fuel economic.

Keywords: Turbulence Models, CFD Analysis, Wind Tunnel Testing, Airfoil, Lift Coefficient, Drag Coefficient.



This work is licensed under a [Creative Commons Attribution-Non Commercial 4.0 International License](https://creativecommons.org/licenses/by-nc/4.0/).

## 1 Introduction

Aerodynamics is one of the important branches of science that deals with the analysis of airflow over a body. The investigation of airflow characteristics over airfoils is inevitable during designing aircraft wings, helicopter rotors, wind turbines, etc. Different approaches such as numerical, analytical, experimental, etc. approaches are followed in any investigation. These approaches have their own pros and cons. Nowadays, computational fluid dynamics (CFD) simulation is gaining enormous popularity, since wind tunnel testing is quite laborious and costly compared to CFD. Hence, the numerical method is the best alternative to the experimental method [1]. It would be more convenient if a turbulence model could predict the aerodynamic performance of an airfoil that would be close to experimental outcomes. CFD is a division of fluid mechanics that utilizes numerical analysis in order to solve and analyze a problem related to fluid flow [2],[3]. It necessitates a governing equation. In CFD analysis, a CAD model is first generated in CAD software, which is then imported into CFD software. Mesh is generated and a proper turbulence model is selected to predict quantitative and qualitative aerodynamic characteristics. Different boundary conditions and convergence criteria are set. Then simulation is initialized and run to obtain numerical results. The key premise of practically all CFD issues is the Navier-Stokes equations. The terms comprising viscous activities are eliminated in order to convert Navier-Stokes equations to Euler equations. In order to obtain linearized potential equations, these equations are then manipulated. Two-dimensional (2D) methods were developed in the 1930s [4]. There are three governing equations upon which all of the fluid dynamics are based: (a) Mass is conserved. (b) The rate of change of momentum is

constant and (c) Energy is conserved. These governing equations can be solved by using either the finite element method or the finite volume method [5].

Sahoo and Maity [6] found  $k-\omega$  SST turbulence model to be more accurate at a high Reynolds number of  $6 \times 10^6$  compared to other turbulence models. Maani et al. [7] also concluded that there was good consistency between  $k-\omega$  SST model and reliable experimental data for the compressible flow of high Reynolds number. Badran [8] showed that the RNG  $k-\epsilon$  model and Reynolds Stress Model (RSM) had the ability to capture the physics of unsteady flow and these models showed excellent agreement with experimental data to predict pressure coefficient, skin friction, velocity vectors, shear stress, and kinetic energy. Oukassou et al. [9] found that Spalart-Allmaras, RNG  $k-\epsilon$  model, and  $k-\omega$  model were in good agreement with experimental outputs. Douvi et al. [10] concluded that  $k-\omega$  SST model is more consistent than any other turbulence model at a moderate Reynolds number of  $3 \times 10^6$  and at a low angle of attack while no turbulence model can provide satisfactory prediction at a high angle of attack. Linjing et al. [11] simulated for S825 and S827 2-D wind turbine with Spalart-Allmaras model, Standard  $k-\omega$  model, and standard  $k-\epsilon$  model and concluded that these models cannot provide accurate prediction for the stall characteristics at high angle of attack. Bacha and Ghaly [12] presented a transition model which reflected a significant improvement in drag prediction at low Reynolds numbers.

The NACA 2412 airfoil is a cambered airfoil and has a maximum camber of 0.02 times chord, which is positioned 0.4 times chord from the leading edge having a maximum thickness of 0.12 times chord. The NACA 0012 airfoil is a symmetric airfoil having a maximum thickness of 0.12 times chord with no

\*Corresponding Author Email Address: [tafsir2086@gmail.com](mailto:tafsir2086@gmail.com)

camber. NACA 0012 airfoils have been used as a reference for the evaluation of wall interference and correction technique. Moreover, they are used as helicopter rotors, rudders, and flaps in the airplane while NACA 2412 airfoils, slow-speed airfoils, are used in the single-engine Cessna 152, 172, and 182 airplanes [13],[14]. Mayer et al. [15] investigated the effect of flow separation of a NACA 0012 airfoil for a range of Reynolds numbers and angles of attack. They observed that the main contributing eddies causing unsteady surface pressure fluctuations move away from the airfoil surface once the flow has separated. Harish et al. [16] studied the prediction of stalling angle by analysis of flow over symmetric airfoil NACA 0012 using reference velocity 01 m/s and concluded that an increase in lift force by 32.32% was observed for 12° angle of attack as compared to 4° angle of attack. Patil and Thakare [17] showed the variation of performance of NACA 0012 airfoil with Reynolds number. NACA0012 provided maximum lift at a high Reynolds number. Hasegawa and Sakaue [18] showed that almost 50% drag was reduced because of using microfiber coating over NACA 0012 airfoil compared to a surface without being coated with microfiber at the Reynolds number of  $6.1 \times 10^4$ . Venkatesan et al. [19] conducted a computational analysis of aerodynamic characteristics of dimple airfoil NACA 2412 airfoil at various angles of attack. They explained that dimples enhance the lift of an airfoil and square dimples had yielded better results. Meghani [20] observed that there was appreciable separation observed to develop at 20% of the chord of NACA 2412 airfoil while conducting wind tunnel test which XFOIL and FLUENT weren't capable to show. It was also concluded that XFOIL was suitable for analysis only at a low Reynolds number ( $Re=500,000$ ). At high Reynolds number, XFOIL results were not found to be accurate for full-scale flow. Havaladar et al. [21] concluded that the lift coefficient for NACA 2412 airfoil with internal passage was higher than the lift coefficient for NACA 2412 airfoil. They showed that the point of separation for NACA 2412 airfoil with internal passage was shifted towards the trailing edge that reducing the boundary layer separation at a higher angle of attack from the airfoil.

Many researchers have attempted to evaluate turbulence models at moderate and high Reynolds numbers. However, very few studies focused on evaluation at low Reynolds number, although aerodynamic characteristics at low Reynolds number are important for low-speed light aircraft, particularly, during takeoff and landing. This study addresses the research gap. The main aim of the present study is to determine a more suitable and accurate turbulence model that has the capability of predicting aerodynamic flow characteristics at low Reynolds number as well as Mach number for the flow over both symmetric and cambered airfoils. In this present study, five different turbulence models are used for numerical analysis of symmetric airfoil NACA 0012 and cambered airfoil NACA 2412 using ANSYS Fluent [22], a renowned CFD software.  $k-\omega$  SST model (2 equations), Standard  $k-\epsilon$  model (2 equations), Spalart-Allmaras model (1 equation), Transition  $k-k_L-\omega$  model (3 equations) and  $\gamma - Re_\theta$  Transition SST model (4 equations) are applied to predict the quantitative and qualitative performance of the airfoils with suitable boundary conditions at a Reynolds number and a Mach number of  $0.05 \times 10^6$  and 0.015 respectively based on the centerline chord of the airfoil. In addition, wind tunnel testing is conducted at the Reynolds number and Mach number same with the numerical investigation to evaluate different turbulence models. The focus of the present study is on the dynamic parameters such as lift coefficient, drag coefficient, etc.

Finally, a comparison of aerodynamic characteristics between NACA 0012 and NACA 2412 airfoil is also presented in order to demonstrate aerodynamically more advantageous airfoil.

## 2 Materials and Methods

### 2.1 Preparing the CAD models in DesignModeler

DesignModeler [22] has been used to prepare CAD models of the airfoil geometries and flow domain. The coordinates of the airfoils are imported to the software and the geometries with flow filed are modeled. Upstream and downstream are taken as 12.5 times chord length. Fig. 1 illustrates the geometry of the flow domain of the airfoils.

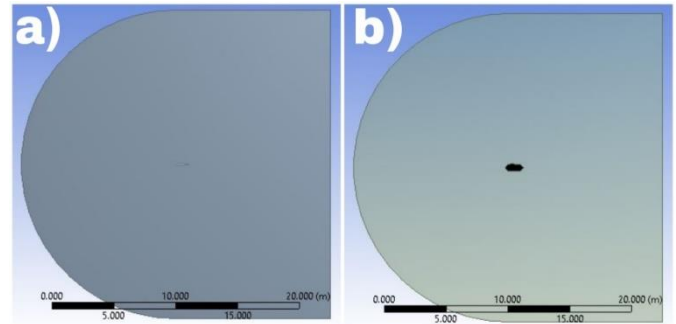


Fig. 1 CAD models of the flow domain of (a) NACA 0012 and (b) NACA 2412 airfoil.

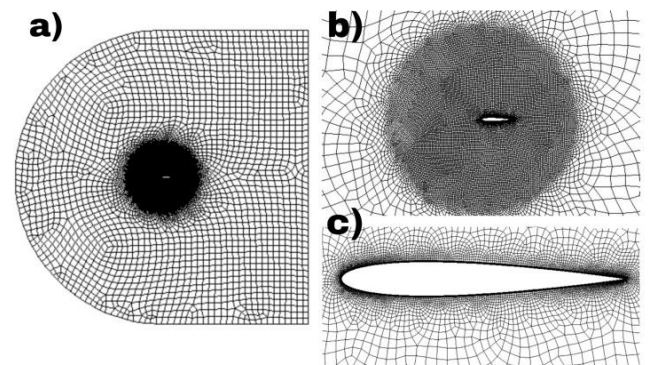


Fig. 2 Mesh of (a) whole flow domain, (b) flow domain near sphere of influence, (c) flow domain near NACA 0012 airfoil.

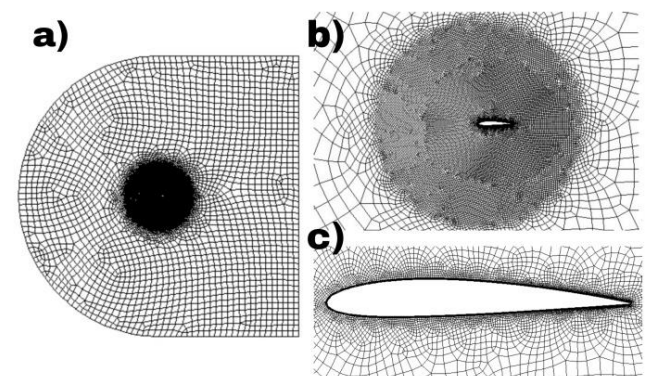


Fig. 3 Mesh of (a) whole flow domain, (b) flow domain near sphere of influence, (c) flow domain near NACA 2412 airfoil.

### 2.2 Mesh Generation

The 2-D CAD models of the flow geometries are imported to ANSYS Fluent. The mesh for both of the geometry of the airfoil is of unstructured type. The cells of the meshes are

quadrilateral and mesh matrix has orthogonal quality. The element is 50% of the chord and the element order is linear. The edge sizing of the airfoil is a bias type of bidirectional having a bias factor of 10 and element size of 0.3% of chord. Smooth transition with 1.2 growth rate inflation is taken near the surfaces of the airfoils. The layers of inflation are 10 and the maximum thickness is 0.6% of the chord. For body sizing, a sphere of influence of radius of 300% of chord and element size of 5% of the chord is taken where the center of the radius of the sphere of influence is at the origin of the global coordinate system. The maximum  $Y^+$  value used in this study is approximately 0.4. A  $Y^+$  value of the size should be sufficient to perfectly resolve the inner part of the boundary layer. A domain with a high grid number leads to an accurate simulated result. However, usage of higher grid numbers results in high computational costs. Hence, the lift coefficient at an angle of attack of  $0^\circ$  for a various number of elements is determined. It is observed that lift coefficients are approximately the same for the element number higher than 25000. Considering computational cost as well as the accuracy of simulation, nodes, and elements of NACA 0012 airfoil have been taken as 27343 and 26962 respectively while nodes and elements of NACA 2412 airfoil have been taken as 26414 and 26040 respectively. Fig. 2 and Fig. 3 demonstrate the mesh of the flow domain of NACA 0012 airfoil and NACA 2412 airfoil respectively.

### 2.3 Governing Equations

#### Conservation of Mass:

Equation (1) represents the continuity equation. It is a common form of conservation of mass equation, which is valid for not only incompressible flow but also compressible flow.

$$\frac{\partial \rho}{\partial t} + \nabla \cdot (\rho \vec{u}) = s_m \quad (1)$$

where, the source  $s_m$  represents the mass that is added to the continuous phase from the dispersed second phase and any user-defined source.

#### Conservation of Momentum:

Equation (2) represents the conservation of momentum.

$$\frac{\partial}{\partial t} (\rho \vec{u}) + \nabla \cdot (\rho \vec{u} \vec{v}) = -\nabla p + \nabla \cdot \vec{\tau} + \rho \vec{g} + \vec{F} \quad (2)$$

Where,  $p$  is the static pressure,  $\rho \vec{g}$  is the gravitational body force,  $\vec{F}$  is the external body force and  $\vec{\tau}$  is the stress tensor which is expressed as:

$$\vec{\tau} = \mu \left[ (\nabla \vec{u} + \nabla \vec{u}^T) - \frac{2}{3} \nabla \cdot \vec{u} I \right] \quad (3)$$

where,  $I$  is the unit tensor, and  $\mu$  is the molecular viscosity.

#### Equations in 2-D:

The continuity equation for the 2-Dimensional, incompressible and steady flow can be expressed as:

$$\frac{\partial u}{\partial x} + \frac{\partial v}{\partial y} = 0 \quad (4)$$

The momentum equations for viscid flow in two dimensions are respectively,

$$\rho \frac{Du}{Dt} = -\frac{\partial p}{\partial x} + \frac{\partial \tau_{xx}}{\partial x} + \frac{\partial \tau_{yx}}{\partial y} + \rho f_x \quad (5)$$

$$\rho \frac{Dv}{Dt} = -\frac{\partial p}{\partial y} + \frac{\partial \tau_{xy}}{\partial x} + \frac{\partial \tau_{yy}}{\partial y} + \rho f_y \quad (6)$$

### 2.3.1 The k- $\omega$ SST Turbulence Model

Standard k- $\omega$  model was developed from Wilcox's [23] k- $\omega$  model which was modified by Menter [24] creating a new turbulence model named k- $\omega$  Shear-Stress Transport (SST) model possessing two equations. This new model is more perfect and consistent than the Standard k- $\omega$  model for a broader class of fluid flows.

The k- $\omega$  SST turbulence model is governed by the following equations.

$$\frac{D\rho k}{Dt} = \tau_{ij} \cdot \frac{\partial u_i}{\partial x_j} + \beta^* \rho \omega k + \frac{\partial}{\partial x_j} \left[ (\mu_{+\sigma_k} \mu_t) \frac{\partial k}{\partial x_j} \right] \text{ and} \quad (7)$$

$$\frac{D\rho \omega}{Dt} = \frac{\gamma}{v_t} \tau_{ij} \frac{\partial u_i}{\partial x_j} - \beta \rho \omega^2 + \frac{\partial}{\partial x_j} \left[ (\mu_{+\sigma_\omega} \mu_t) \frac{\partial \omega}{\partial x_j} \right] + 2\rho(1-F_1)\sigma_\omega \frac{1}{\omega} \frac{\partial k}{\partial x_j} \frac{\partial \omega}{\partial x_j} \quad (8)$$

where,

$\beta^* = \frac{\epsilon}{k\omega}$  and the turbulence stress tensor is

$$\tau_{ij} = -\rho \overline{u_i' u_j'} = \mu_t \left( \frac{\partial u_i}{\partial x_j} + \frac{\partial u_j}{\partial x_i} - \frac{2}{3} \frac{\partial u_k}{\partial x_k} \delta_{ij} \right) - \frac{2}{3} \rho k \delta_{ij} \quad (9)$$

The turbulence viscosity can be determined by  $v_t = a_1 \frac{k}{\max[a_1 \omega, \Omega F_2]}$  where,  $\Omega$  = the absolute value of the vorticity,  $a_1 = 31.01$  and the function  $F_2$  is given by

$$F_2 = \tanh \left\{ \left[ \max \left( \frac{2\sqrt{k}}{0.09\omega y}, \frac{500v}{y^2\omega} \right) \right]^2 \right\} \quad (10)$$

where,  $y$  is the distance to the nearest surface.

The coefficients  $\beta, \gamma, \sigma_k, \sigma_\omega$  are defined as functions of the coefficients of the k- $\omega$  model which are defined as follows:

$$\begin{aligned} \beta &= F_1 \beta_1 + (1 - F_1) \beta_2, \gamma = F_1 \gamma_1 + (1 - F_1) \gamma_2 \\ \sigma_k &= F_1 \sigma_{k_1} + (1 - F_1) \sigma_{k_2}, \sigma_\omega = F_1 \sigma_{\omega_1} + (1 - F_1) \sigma_{\omega_2} \end{aligned} \quad (11)$$

where the function  $F_1$  is

$$F_1 = \tanh \left\{ \left[ \min \left[ \max \left( \frac{\sqrt{k}}{0.09\omega y}, \frac{500v}{y^2\omega} \right), \frac{4\rho\sigma_{\omega_2}k}{CD_{k\omega}y^2} \right] \right]^4 \right\} \quad (12)$$

and the coefficient

$$CD_{k\omega} = \max \left( 2\rho\sigma_{\omega_2} \frac{1}{\omega} \frac{\partial k}{\partial x_j} \frac{\partial \omega}{\partial x_j}, 10^{-20} \right) \quad (13)$$

#### Model constants:

$\beta^* = 0.09, \beta_1 = 0.075, \beta_2 = 0.0828, \gamma_1 = 0.5532, \gamma_2 = 0.4404, \sigma_{k_1} = 0.85, \sigma_{k_2} = 1.0, \sigma_{\omega_1} = 0.5$  and  $\sigma_{\omega_2} = 0.856$ .

### 2.3.2 Standard k- $\epsilon$ Model

Launder and Spalding [25] proposed a turbulence model that involves two equations. The model is popularly known as the standard k- $\epsilon$  model and is the most widely-used engineering turbulence model which is robust and reasonably accurate. The standard k- $\epsilon$  model is valid only for fully developed turbulent flows. Some modifications have been made over time to this model. These modified models include the RNG k- $\epsilon$  model and the realizable k- $\epsilon$  model [26]. Enhanced wall function was used

as  $\varepsilon$  equation contains a term which cannot be calculated without wall function.

The transport equation for turbulent kinetic energy ( $k$ ) is

$$\frac{\partial(\rho k)}{\partial t} + \frac{\partial(\rho k u_i)}{\partial x_i} = \frac{\partial}{\partial x_j} \left[ \left( \mu + \frac{\mu_t}{\sigma_k} \right) \frac{\partial k}{\partial x_j} \right] + G_k + G_b - \rho \varepsilon - Y_M + S_k \quad (14)$$

and transport equation for turbulent dissipation rate ( $\varepsilon$ ) is

$$\frac{\partial(\rho \varepsilon)}{\partial t} + \frac{\partial(\rho \varepsilon u_i)}{\partial x_i} = \frac{\partial}{\partial x_j} \left[ \left( \mu + \frac{\mu_t}{\sigma_\varepsilon} \right) \frac{\partial \varepsilon}{\partial x_j} \right] + C_{1\varepsilon} \frac{\varepsilon}{k} (G_k + C_{3\varepsilon} G_b) - C_{2\varepsilon} \rho \frac{\varepsilon^2}{k} + S_\varepsilon \quad (15)$$

where,  $\mu_t =$  turbulent viscosity  $= \rho C_\mu \frac{k^2}{\varepsilon}$ ,  $G_k =$  generation of the turbulent kinetic energy due to the mean velocity gradient,  $\sigma_k =$  effective prandtl number for turbulent kinetic energy,  $\sigma_\varepsilon =$  effective prandtl number for rate of dissipation,  $C_{1\varepsilon}, C_{2\varepsilon}$  are constants

*Model Constants:*

The default values of model constants  $C_{1\varepsilon}, C_{2\varepsilon}, C_\mu, \sigma_k,$  and  $\sigma_\varepsilon$  determined from experiments for fundamental turbulent flows and have the following values.

$$C_{1\varepsilon} = 1.44, C_{2\varepsilon} = 1.92, C_\mu = 0.09, \sigma_k = 1.0, \sigma_\varepsilon = 1.3$$

### 2.3.3 Spalart-Allmaras Model

Spalart-Allmaras model is a one equation turbulence model that was proposed by Spalart and Allmaras [27]. It was mainly designed for applications that involve aerodynamic operations while it is now also being used in turbomachinery applications. This model solves a transport equation that involves kinematic eddy viscosity. The main advantage of this model is that it is relatively robust. The resolution requirement is moderate. It is quite stable and it also shows good convergence.

The transported variable in the Spalart-Allmaras model,  $\tilde{\nu}$ , is identical to the turbulent kinematic viscosity except in the near-wall (viscosity-affected) region. The transport equation for  $\tilde{\nu}$  is

$$\frac{\partial}{\partial t} (\rho \tilde{\nu}) + \frac{\partial}{\partial x_i} (\rho \tilde{\nu} u_i) = G_\nu + \frac{1}{\sigma_\nu} \left[ \frac{\partial}{\partial x_j} \cdot \left\{ \left( \mu + \rho \tilde{\nu} \right) \frac{\partial \tilde{\nu}}{\partial x_j} \right\} + C_{b2} \rho \left( \frac{\partial \tilde{\nu}}{\partial x_i} \right)^2 \right] - Y_\nu + S_\nu \quad (16)$$

where,  $G_\nu =$  the production of turbulent viscosity,  $Y_\nu =$  the destruction of turbulent viscosity that occurs in the near-wall region due to wall blocking and viscous damping,  $\nu =$  the molecular kinematic viscosity,  $S_\nu =$  a user-defined source term and  $\sigma_\nu$  and  $C_{b2}$  are the constants.

*Model constants:*

$$C_{b2} = 0.622, \sigma_\nu = \frac{2}{3}$$

### 2.3.4 Transition k-k<sub>L</sub>- $\omega$ Model

Walter and Cokljat [28] developed a three equation k-k<sub>L</sub>- $\omega$  turbulence model which was inspired by the idea that was introduced by Walters and Leylek [29]. The model can successfully predict boundary layer development and transition flow behavior in various fluid systems.

The k-k<sub>L</sub>- $\omega$  model is considered to be a three-equation eddy-viscosity type, which includes transport equations for turbulent kinetic energy ( $k_T$ ), laminar kinetic energy ( $k_L$ ), and the inverse turbulent time scale ( $\omega$ ).

$$\frac{Dk_T}{Dt} = P_{k_T} + R + P_{NAT} - \omega k_T - D_T + \frac{\partial}{\partial x_j} \left[ \left( \nu + \frac{\alpha_T}{\alpha_k} \right) \frac{\partial k_T}{\partial x_j} \right] \quad (17)$$

$$\frac{Dk_L}{Dt} = P_{k_L} - R - R_{NAT} - D_L + \frac{\partial}{\partial x_j} \left[ \nu \frac{\partial k_L}{\partial x_j} \right] \quad (18)$$

$$\frac{D\omega}{Dt} = C_{\omega 1} \frac{\omega}{k_T} P_{k_T} + \left( \frac{C_{\omega 2}}{f_W} - 1 \right) \frac{\omega}{k_T} (R + R_{NAT}) - C_{\omega 2} \omega^2 + C_{\omega 3} f_{\omega} \alpha_T f_W^2 \frac{\sqrt{k_T}}{d^3} + \frac{\partial}{\partial x_j} \left[ \left( \nu + \frac{\alpha_T}{\alpha_\omega} \right) \frac{\partial \omega}{\partial x_j} \right] \quad (19)$$

*Model constants:*

$$C_{\omega 1} = 0.44, C_{\omega 2} = 0.92, C_{\omega 3} = 0.3$$

### 2.3.5 $\gamma - Re_\theta$ Transition SST Model

$\gamma - Re_\theta$  transition SST model was developed subsequently by Menter and Langraty [30]-[32]. It had successfully been used for flow prediction of an expansion swirl flow [33]. The transition SST model is based on the coupling of the SST k- $\omega$  transport equations with two other transport equations, one for the intermittency and one for the transition onset criteria, in terms of momentum-thickness Reynolds number.

The transport equation for the intermittency  $\gamma$  is defined as

$$\frac{\partial(\rho \gamma)}{\partial t} + \frac{\partial(\rho U_j \gamma)}{\partial x_j} = P_{\gamma 1} - E_{\gamma 1} + P_{\gamma 2} - E_{\gamma 2} + \frac{\partial}{\partial x_j} \left[ \left( \mu + \frac{\mu_t}{\sigma_\gamma} \right) \frac{\partial \gamma}{\partial x_j} \right] \quad (20)$$

The transition sources are defined as

$$E_{\gamma 1} = P_{\gamma 1} \gamma \text{ and} \quad (21)$$

$$P_{\gamma 1} = F_{length} \rho S [\gamma F_{onset}]^{c_{\gamma 3}} \quad (22)$$

where,  $S =$  the strain rate magnitude,  $F_{length} =$  an empirical correlation that controls the length of the transition region.

The destruction/relaminarization sources are defined as

$$P_{\gamma 2} = (2c_{\gamma 1}) \rho \Omega \gamma F_{turb} \text{ and} \quad (23)$$

$$E_{\gamma 2} = c_{\gamma 2} P_{\gamma 2} \gamma \quad (24)$$

where,  $\Omega$  is the vorticity magnitude.

*Model constants:*

$$c_{\gamma 1} = 0.03, c_{\gamma 2} = 50, c_{\gamma 3} = 1.0$$

### 2.4 Setting Boundary Conditions

The Mach number in this study is 0.015, which is lesser than 0.3 for which the flow is considered as incompressible and therefore energy equation has been omitted in numerical simulation. The solver has been taken as pressure-based and velocity formation has been taken as absolute. The time for the flow has been set as steady. Wall boundary condition is applied for airfoil surfaces with no-slip boundary conditions. The inlet (far-field 1) is assigned as velocity inlet where the velocity specification method is taken as component and reference frame is absolute with an initial gauge pressure of 0 Pa. The specification of turbulence is taken as an intensity to viscosity ratio with a turbulence intensity of 5% and turbulence viscosity ratio of 10. The outlet (far-field 2) is assigned as a pressure outlet having a gauge pressure of 0 Pa and the backflow reference frame is set as absolute, the backflow direction specification method is set as normal to the boundary, and the backflow pressure specification is set as total pressure. Fig. 4 illustrates the flow domain of the problem. Boundary conditions and other variables related to the numerical investigation are tabulated in Table 1.

### 2.5 Simulation Setup

The SIMPLE pressure-velocity coupling has been used in the present study. For spatial discretization, the gradient is taken as least square cell-based and other parameters are taken as second-order upwind. Reports have been defined to calculate lift and drag coefficients. The convergence condition is taken as absolute criteria. The criterion of the residuals is taken as  $10^{-6}$ . The solution is initialized with the standard initialization method. Then the calculation is, then, run to get quantitative and qualitative numerical results.

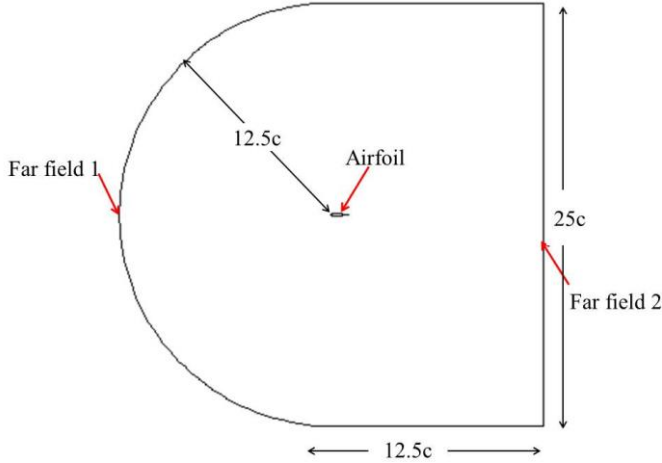


Fig. 4 Flow domain of the problem.

Table 1 Boundary conditions and some other variables.

Variable	Value
Fluid type	air
Test object material	wood
Free stream temperature	20 °C
Gauge pressure	0 Pa
Free stream velocity of air	5 m/s
Density of air	1.204 kg/m <sup>3</sup>
Viscosity of air	1.825 × 10 <sup>-5</sup> kg·m <sup>-1</sup> ·s <sup>-1</sup>
Chord Reynolds number	0.05 × 10 <sup>6</sup>
Mach number	0.015

### 2.6 Wind Tunnel Experiment

The wind tunnel experiment has been conducted using a subsonic open-circuit wind tunnel consisting of a converging and diverging nozzle to verify the performance of the turbulence models. The specification of the wind tunnel is presented in Table 2.

The models for both of the airfoils have been made of wood with having a chord of 150 mm and a span of 450 mm. The models have been fabricated and provided a smooth surface finish and thick coating so that the output obtained from wind tunnel testing is more accurate. Fig. 5 shows the wind tunnel with an airfoil mounted on it. In this present study, the free stream velocity is taken as 5 m/s for both of the airfoils which yield a Reynolds number of  $0.05 \times 10^6$  and Mach number of 0.015 based on the centerline chord of the airfoils. The velocity of air is increased up to 5 m/s and was inspected by a monitor.

Table 2 Specifications of the wind tunnel.

Specifications	Value
Model	TecQuipment AF100
Electrical supply	3 phase, 220 VAC to 240 VAC 50 Hz/60 Hz (20 A) or 380 VAC to 440 VAC 50 Hz/60 Hz (16 A)
Space required	2 m of free space around the inlet and 4 m at the outlet
Operating temperature range	5 °C to 40 °C
Operating relative humidity range	80% at temperatures < 31°C decreasing linearly to 50% at 40°C.
Net dimensions	3700 mm × 1065 mm × height 1900 mm
Dimensions of the working section	305 mm × 305 mm, and 600 mm long
Net weight	293 kg
Range of air velocity	0 to 36 ms <sup>-1</sup>
Noise level	80 dB(A)

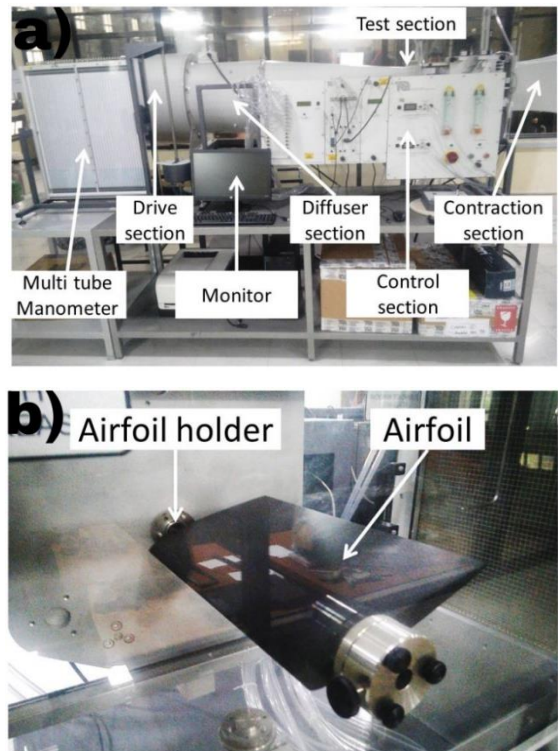


Fig. 5 Experimental setup showing (a) whole experimental setup and (b) close view of airfoil setup.

Lift and drag force are obtained using wind tunnel testing for both of the airfoils. Lift coefficient and drag coefficient are determined from these aerodynamic forces using Eqs. (25) and (26) respectively.

$$C_L = \frac{F_L}{\frac{1}{2} \rho v^2 A} \quad (25)$$

$$C_D = \frac{F_D}{\frac{1}{2} \rho v^2 A} \quad (26)$$

Where,  $F_L$  is lift force in N,  $F_D$  is drag force in N,  $C_L$  is lift coefficient,  $C_D$  is drag coefficient,  $\rho$  is the density of the air through the airfoil is moving in  $\text{kg/m}^3$ ,  $v$  is the relative speed between airfoil and air in  $\text{m/s}$  and  $A$  is the projected area of the airfoil in  $\text{m}^2$ .

In order to monitor experimental results such as lift coefficient and drag coefficient at a different angle of attack for both of the airfoils, computer along with TecQuipment's Versatile Data Acquisition System (VDAS®) software is used. With the usage of VDAS® software, lift coefficient and drag coefficient are accurately determined.

### 3 Results and discussion

#### 3.1 Evaluation of turbulence models for the flow over NACA 0012 airfoil

Fig. 6 illustrates a comparison between experimental data and numerical results of five different turbulence models of the lift coefficient curve for NACA 0012 airfoil. It is observed that Spalart-Allmaras model and k- $\omega$  SST model are able to reasonably predict lift coefficient up to the angle of attack of  $9^\circ$  and  $6^\circ$  respectively. Hence, it is obvious that Spalart-Allmaras model gives the most accurate prediction among other models. This finding is closely in agreement with previous studies conducted on the accuracy of turbulence models [6],[7],[9],[10]. The standard k- $\epsilon$  model gives slightly less value of lift coefficient at low angle of attack and slightly high value of lift coefficient at high angle of attack. However, at high angle of attack no turbulence model is capable of providing a satisfactory prediction. This phenomenon is also confirmed by prior studies [10],[11]. Transition k-kL- $\omega$  model and  $\gamma - Re_\theta$  Transition SST model are far beyond accuracy.

Fig. 7 demonstrates a comparison between experimental data and numerical results of five different turbulence models of the drag coefficient curve for NACA 0012 airfoil. It is observed that k- $\omega$  SST model, Spalart-Allmaras model, Transition k-kL- $\omega$  model, and  $\gamma - Re_\theta$  Transition SST model can predict drag coefficient reasonably at low angle of attack. The standard k- $\epsilon$  model gives slightly high value of drag coefficient at a low angle of attack and a slightly low value of drag coefficient at a high angle of attack. However, at a high angle of attack, no turbulence model can give a satisfactory prediction and all models except the Transition k-kL- $\omega$  model provide a lesser value of drag coefficient than that of the experimental value. Previous studies also indicate that turbulence models aren't capable of predicting at a high angle of attack [10],[11].

Fig. 8 and Fig. 9 illustrate contours of static pressure at the angle of attack of  $0^\circ$ ,  $6^\circ$ ,  $9^\circ$ , and  $18^\circ$  derived from Spalart-Allmaras model and k- $\omega$  SST model respectively for NACA 0012 airfoil. It can be observed that pressure distribution is symmetrical at  $0^\circ$  angle of attack because of NACA 0012 being symmetric airfoil while the pressure on the upper surface is lower than that of the lower surface at  $6^\circ$  and  $9^\circ$  angle of attack. Hence, a lift is produced upward. As the angle of attack is increased from  $0^\circ$  up to  $9^\circ$ , the pressure on the lower surface is increased as a result of which the lift force and lift coefficient are increased in

the upward direction. However, separation takes place at an angle of attack of  $18^\circ$  due to which the lift coefficient is dramatically decreased.

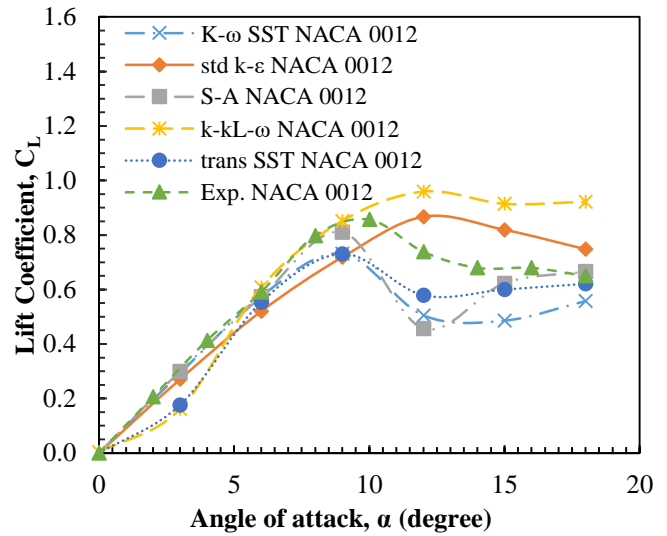


Fig. 6 Comparison between experiment data and numerical results of five different turbulence models of the lift coefficient curve for NACA 0012 airfoil.

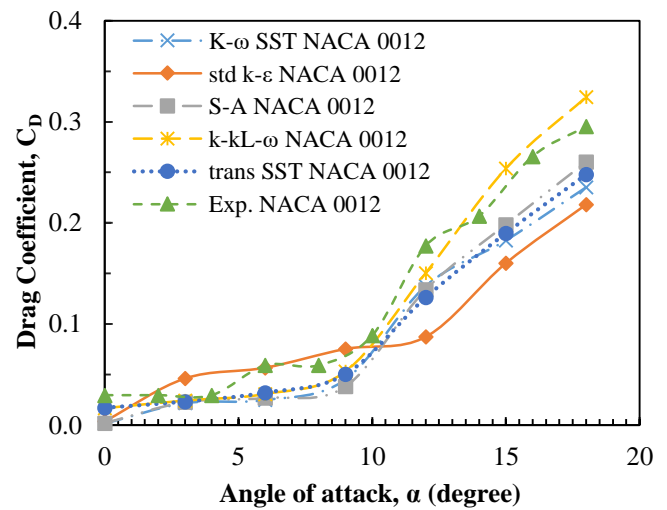


Fig. 7 Comparison between experiment data and numerical results of five different turbulence models of the drag coefficient curve for NACA 0012 airfoil.

Fig. 10 and Fig. 11 demonstrate contours of velocity magnitude at the angle of attack of  $0^\circ$ ,  $6^\circ$ ,  $9^\circ$  and  $18^\circ$  for Spalart-Allmaras model and k- $\omega$  SST model respectively for NACA 0012 airfoil. It can be observed that velocity magnitude is symmetrical at  $0^\circ$  angle of attack while in contrast to pressure distribution the velocity magnitude on the upper surface is higher than that of the lower surface for increased angle of attack which confirms Bernoulli's principle. The stagnation point at the trailing edge is moved forward to the direction of the leading edge with the increase in the angle of attack.

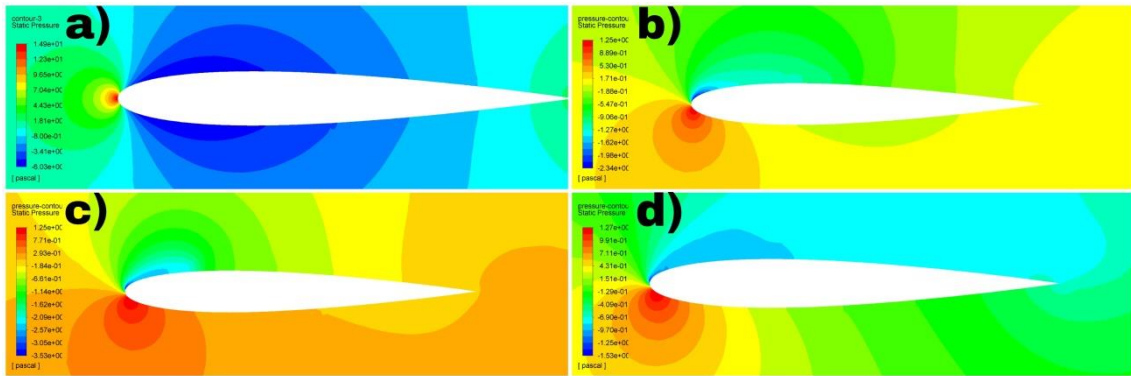


Fig. 8 Contours of static pressure at an angle of attack of (a) 0°, (b) 6°, (c) 9°, (d) 18° derived from Spalart-Allmaras model for NACA 0012 airfoil.

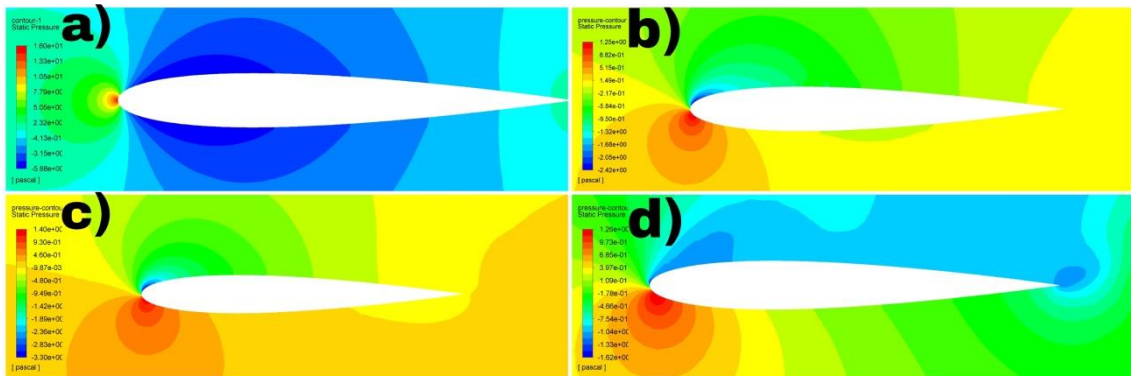


Fig. 9 Contours of static pressure at an angle of attack of (a) 0°, (b) 6°, (c) 9°, (d) 18° derived from k- $\omega$  SST model for NACA 0012 airfoil.

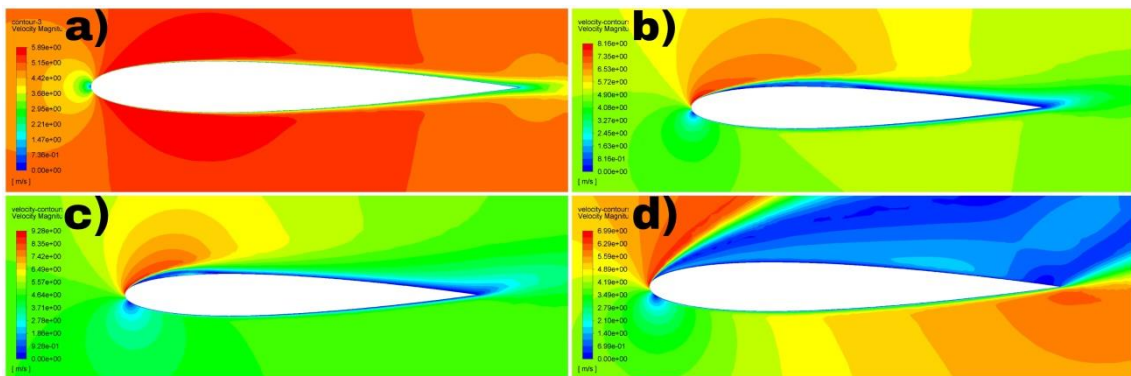


Fig. 10 Contours of velocity magnitude at an angle of attack of (a) 0°, (b) 6°, (c) 9°, (d) 18° derived from Spalart-Allmaras model for NACA 0012 airfoil.

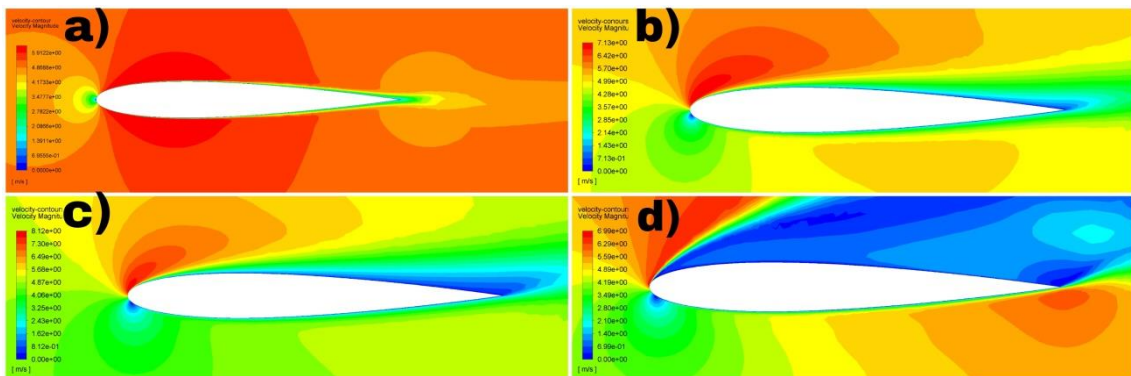


Fig. 11 Contours of velocity magnitude at an angle of attack of (a) 0°, (b) 6°, (c) 9°, (d) 18° derived from k- $\omega$  SST model for NACA 0012 airfoil.

### 3.2 Evaluation of turbulence models for the flow over NACA 2412 airfoil

Fig. 12 illustrates a comparison between experimental data and numerical results of five different turbulence models of the lift coefficient curve for NACA 2412 airfoil. It is observed that Spalart-Allmaras model and k- $\omega$  SST model are successfully able to predict lift coefficient up to the angle of attack of 9°. This finding is closely in agreement with earlier studies conducted on the assessment of turbulence models [6],[7],[9],[10]. Standard k- $\epsilon$  model gives slightly less value of lift coefficient at low angle of attack and slightly more value of lift coefficient at high angle of attack. However, no turbulence model is able to depict post-stall characteristics. Transition k- $k_L$ - $\omega$  model and  $\gamma - Re_\theta$  transition SST model are far beyond accuracy.

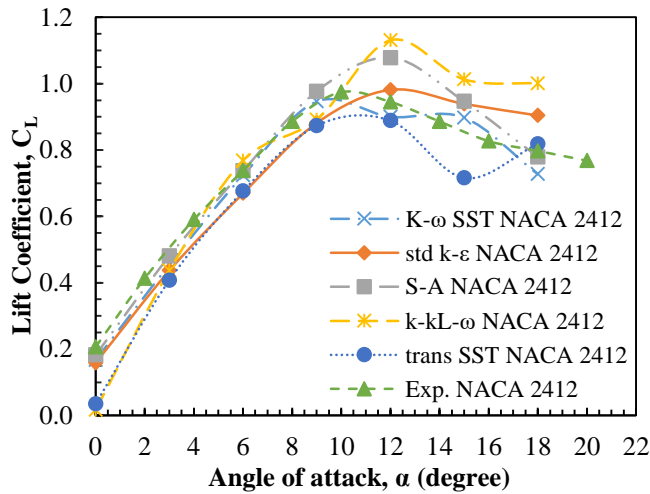


Fig. 12 Comparison between experiment data and numerical results of five different turbulence models of the lift coefficient curve for NACA 2412 airfoil.

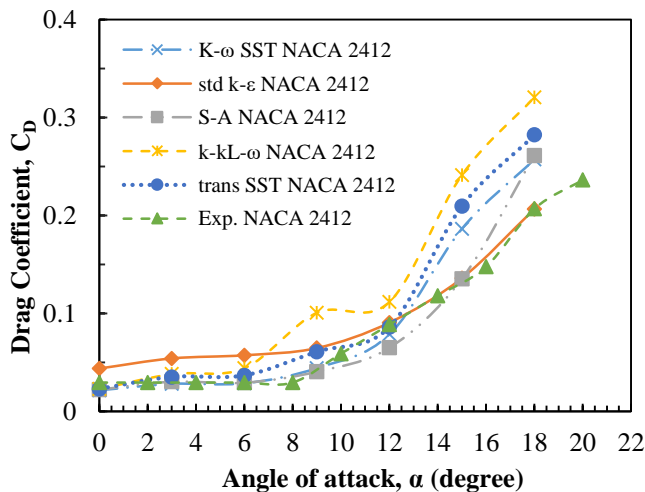


Fig. 13 Comparison between experiment data and numerical results of five different turbulence models of the drag coefficient curve for NACA 2412 airfoil.

Fig. 13 illustrates a comparison between experimental data and numerical results of five different turbulence models of the drag coefficient curve for NACA 2412 airfoil. It is observed that k- $\omega$  SST model, Spalart-Allmaras model, Transition k- $k_L$ - $\omega$  model and  $\gamma - Re_\theta$  Transition SST model are capable of predicting drag coefficient effectively at a low angle of attack. The standard k- $\epsilon$  model gives slightly high value of drag coefficient at a low angle of attack and exhibits a good prediction of drag coefficient at a high angle of attack. However, at a high angle of attack, no turbulence model can give a satisfactory prediction except the Standard k- $\epsilon$  model and they give higher value of drag coefficient than that of the experimental value. Douvi et al. [10] also observed that higher drag coefficients than that of the experimental result were deduced by different turbulence models.

Contours of static pressure at the angle of attack of 0°, 6°, 9° and 18° derived from Spalart-Allmaras model and k- $\omega$  SST model are demonstrated at Fig. 14 and Fig. 15 respectively for NACA 2412 airfoil. It can be observed that the pressure on the upper surface is lower than that of the lower surface because of which a lift is produced upward. As the angle of attack is increased from 0° to 9°, the pressure on the lower surface is increased as a result of which the lift force and lift coefficient are increased in the upward direction. However, separation takes place at an angle of attack of 18° due to which the lift coefficient is dramatically decreased.

Contours of velocity magnitude at the angle of attack of 0°, 6°, 9° and 18° for Spalart-Allmaras model and k- $\omega$  SST model are illustrated at Fig. 16 and Fig. 17 respectively for NACA 2412 airfoil. It can be observed that, unlike pressure distribution, the velocity magnitude on the upper surface is higher than that of the lower surface, which confirms Bernoulli's principle. The stagnation point at the trailing edge is moved forward to the direction of the leading edge with the increase in the angle of attack.

### 3.3 Comparison of NACA 0012 and NACA 2412 using experimental results

Fig. 18 illustrates a variation of lift coefficient with respect to the angle of attack for both NACA 0012 and NACA 2412 airfoils. It is observed that at a low angle of attack the lift coefficient increases almost linearly with the angle of attack and reaches its highest value at stall angle of attack (10°) because airflow is attached to the surfaces of airfoils at these angles of attack. After stall angle of attack, there is a dramatic decrease in lift coefficient because of the separation of the boundary layer. It can also be observed that the lift coefficient of NACA 2412 airfoil is greater than that of the NACA 0012 airfoil for all angles of attack. It was also depicted by Oukassou et al. [9] that NACA 2412 airfoil provided greater lift coefficients for a wide range of angles of attack at a Reynolds number of  $10^6$ . Hence, NACA 2412 airfoil provides better aerodynamic performance. The lift coefficient is zero lift for 0° angle of attack for NACA 0012 airfoil while there is an appreciable lift coefficient at 0° angle of attack for NACA 2412 airfoil.

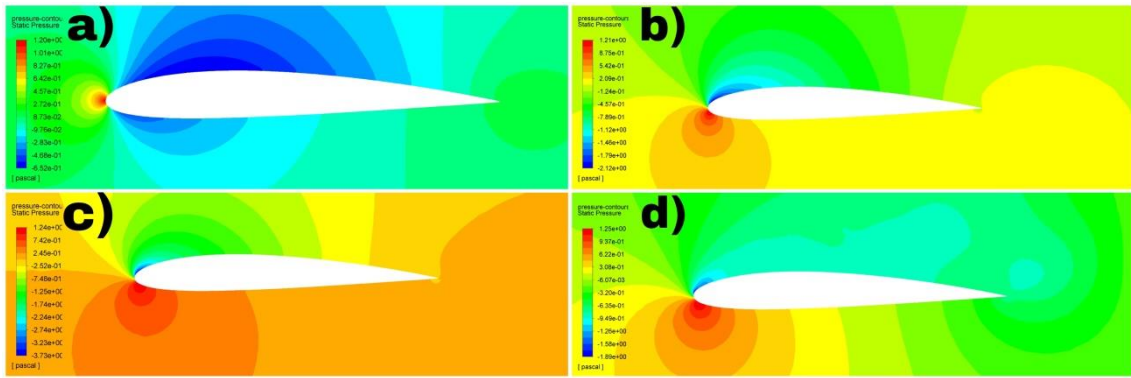


Fig. 14 Contours of static pressure at an angle of attack of (a) 0°, (b) 6°, (c) 9°, (d) 18° derived from Spalart-Allmaras model for NACA 2412 airfoil.

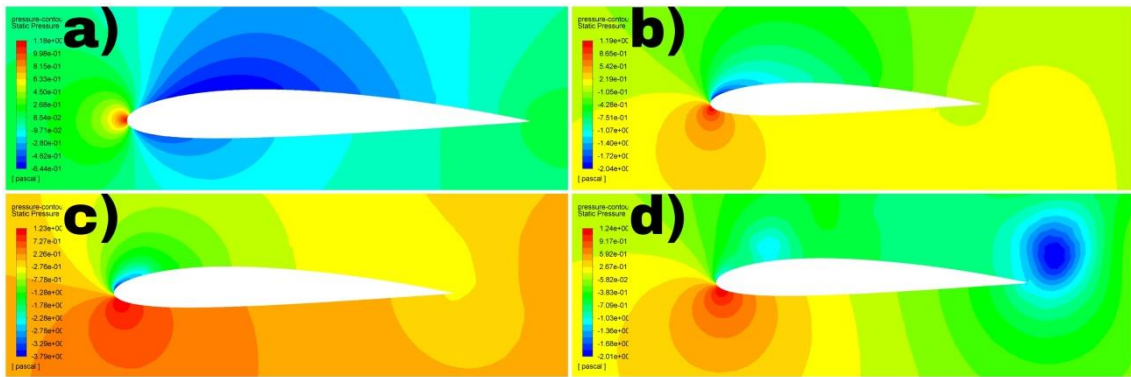


Fig. 15 Contours of static pressure at an angle of attack of (a) 0°, (b) 6°, (c) 9°, (d) 18° derived from k- $\omega$  SST model for NACA 2412 airfoil

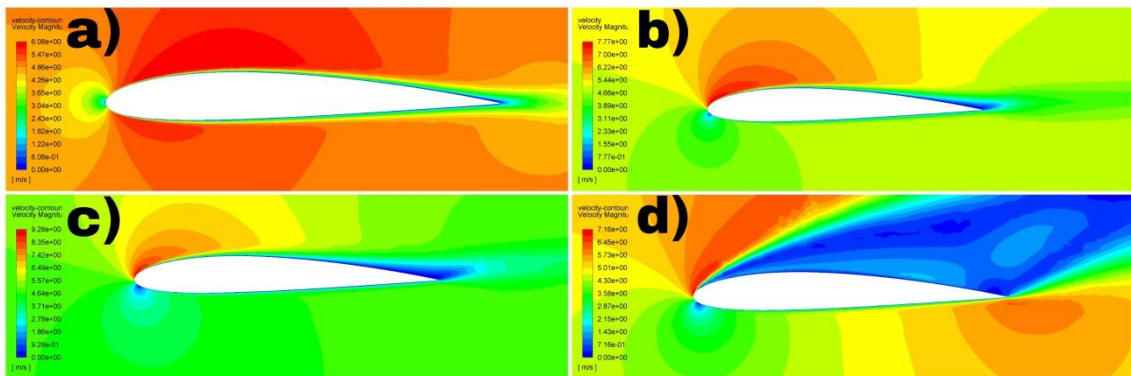


Fig. 16 Contours of velocity magnitude at an angle of attack of (a) 0°, (b) 6°, (c) 9°, (d) 18° derived from Spalart-Allmaras model for NACA 2412 airfoil.

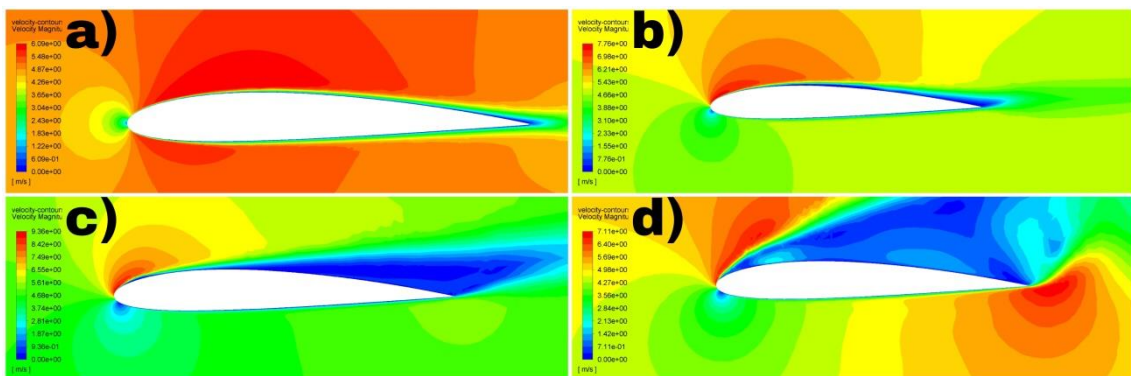


Fig. 17 Contours of velocity magnitude at an angle of attack of (a) 0°, (b) 6°, (c) 9°, (d) 18° derived from k- $\omega$  SST model for NACA 2412 airfoil.

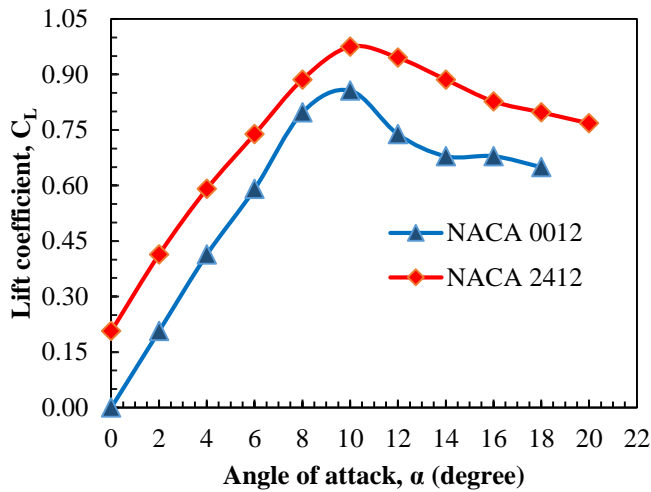


Fig. 18 Comparison of lift coefficient between NACA 0012 and NACA 2412 airfoils using experimental data.

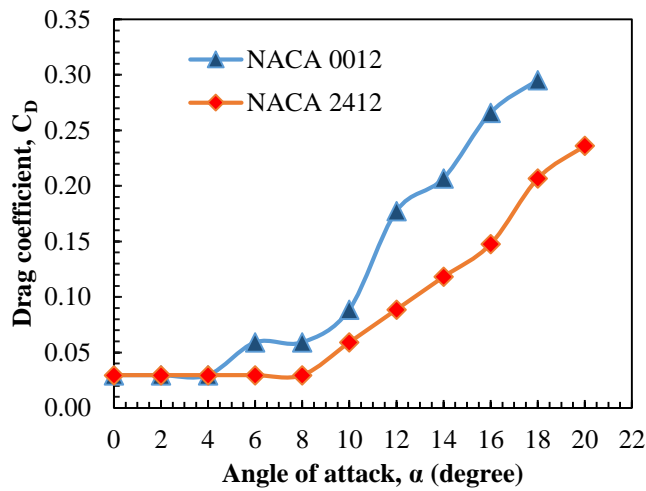


Fig. 19 Comparison of drag coefficient between NACA 0012 and NACA 2412 airfoils using experimental data.

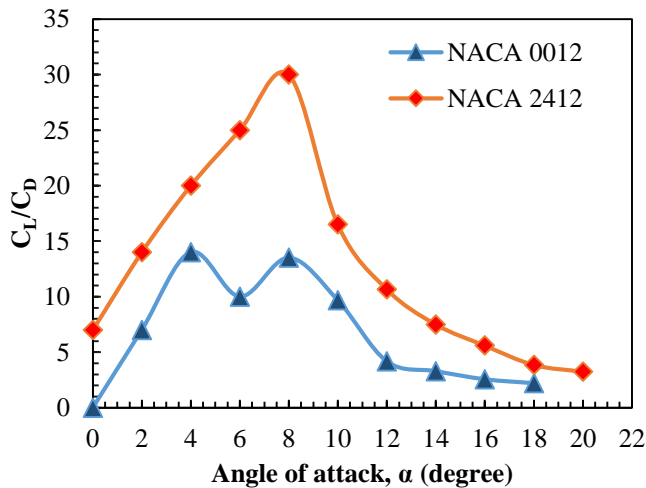


Fig. 20 Comparison of lift coefficient to drag coefficient ratio between NACA 0012 and NACA 2412 airfoils using experimental data.

Fig. 19 demonstrates the variation of drag coefficient with respect to the angle of attack for both NACA 0012 and NACA 2412 airfoils. It can be observed that at a low angle of attack the drag coefficient varies a little bit with respect to the angle of

attack since only skin friction drag is affecting the airfoils while the pressure drag is negligible. After stall angle of attack, there is a rapid increase in drag coefficient which is due to separation of flow, which enhances pressure drag, and thus total drag is increased. It is also observed that the drag coefficient of NACA 0012 is higher than that of NACA 2412 airfoil at almost all angles of attack.

Fig. 20 illustrates the variation of lift coefficient to drag coefficient ratio with respect to the angle of attack for both NACA 0012 and NACA 2412 airfoils. It can be observed that the lift coefficient to drag coefficient ratio of NACA 2412 is higher than that of NACA 0012 airfoil for all angles of attack. The ratio increases from zero angle of attack to the angle of attack of 8° for NACA 2412 airfoil and 4° for NACA 0012 airfoil and after that lift coefficient to drag coefficient ratio gradually falls. The lift coefficient to drag coefficient ratio of NACA 2412 airfoil is greater than that of the NACA 0012 airfoil which indicates that NACA 2412 airfoil is more fuel economic.

#### 4 Conclusions

This paper has presented the evaluation of five different turbulence models at low Reynolds number as well as the aerodynamic comparison between NACA 0012 airfoil and NACA 2412 airfoil for various angles of attack. The findings of this study can be concluded as follow:

Spalart-Allmaras model and  $k-\omega$  SST model are capable of providing the most accurate prediction for lift coefficient at low angle of attack for both airfoils.  $k-\omega$  SST model, Spalart-Allmaras model, Transition  $k-k_L-\omega$  model, and  $\gamma-Re_\theta$  transition SST model can predict drag coefficient reasonably at a low angle of attack. At a high angle of attack, however, no turbulence model is able to provide a satisfactory prediction for lift coefficient and drag coefficient indicating that these models are unable to predict post-stall characteristics. NACA 2412 airfoil provides better aerodynamic performance. Moreover, NACA 2412 is more fuel economic. NACA 0012 airfoil provides zero lift at an angle of attack of 0° while NACA 2412 airfoil provides appreciable lift at an angle of attack of 0°. The stall angle of attack for both of the airfoils is found to be the same *ie.* 10°.

#### Acknowledgments

The authors are grateful to Fluid Machinery Lab, Chittagong University of Engineering & Technology for providing the laboratory facility.

#### References

- [1] Patel, K.S., Patel, S.B., Patel, U.B. and Ahuja, A.P., 2014. CFD Analysis of an Aerofoil. *International Journal of Engineering Research*, 3(3), pp.154-158.
- [2] Pranto, M.R.I. and Inam, M.I., 2020. Numerical Analysis of the Aerodynamic Characteristics of NACA4312 Airfoil. *Journal of Engineering Advancements*, 1(02), pp.29-36.
- [3] Mubassira, S., Muna, F.I. and Inam, M.I., 2021. Numerical Investigation of Aerodynamic Characteristics of NACA 4312 Airfoil with Gurney Flap. *Journal of Engineering Advancements*, 2(02), pp.63-70.
- [4] Milne-Thomson, L.M., 1973. *Theoretical aerodynamics*. Courier Corporation.

- [5] McLay, A., 1995. Computational Fluid Dynamics: the Basics with Applications, JD Anderson, McGraw-Hill Book Company.
- [6] Sahoo, S. and Maity, S., 2020. CFD Analysis of Responses of Two-Equation Turbulence Models for Flow over NACA 0012, NACA 4412 and S809 Aerofoils. In *Advances in Mechanical Engineering* (pp. 31-40). Springer, Singapore.
- [7] El Maani, R., Radi, B. and El Hami, A., CFD Analysis of the Transonic Flow over a NACA 0012 Airfoil. Published by ISTE Ltd. London, UK.
- [8] Badran, O., Aldudak, R.Q.F. and und Aerodynamik, F.S., Two-Equation Turbulence Models for Turbulent Flow over a NACA 4412 Airfoil at Angle of Attack 15 Degree. *Mechanical Engineering Department, Faculty of Engineering technology, Al-Balqa Applied University, Jordan*.
- [9] Oukassou, K., El Mouhsine, S., El Hajjaji, A. and Kharbouch, B., 2019. Comparison of the power, lift and drag coefficients of wind turbine blade from aerodynamics characteristics of Naca0012 and Naca2412. *Procedia Manufacturing*, 32, pp.983-990.
- [10] Eleni, D.C., Athanasios, T.I. and Dionissios, M.P., 2012. Evaluation of the turbulence models for the simulation of the flow over a National Advisory Committee for Aeronautics (NACA) 0012 airfoil. *Journal of Mechanical Engineering Research*, 4(3), pp.100-111.
- [11] Linjing, M.A., Jiang, C., Gang, D.U. and Renjing, C., 2010. Numerical simulation of aerodynamic performance for wind turbine airfoils. *Acta Energiæ Solaris Sinica.*, 2, pp.203–209.
- [12] Bacha, W. and Ghaly, W., 2006. Drag prediction in transitional flow over two-dimensional airfoils. In *44th AIAA AeroSpace Sciences Meeting and Exhibit* (p. 248).
- [13] Sogukpinar, H., 2018, February. The effects of NACA 0012 airfoil modification on aerodynamic performance improvement and obtaining high lift coefficient and post-stall airfoil. In *AIP conference proceedings* (Vol. 1935, No. 1, p. 020001). AIP Publishing LLC.
- [14] Saxena, E.S. and Kumar, M.R., 2015. Design of NACA 2412 and its Analysis at Different Angle of Attacks, Reynolds Numbers, and a wind tunnel test. *International Journal of Engineering Research and General Science*, 3(2), pp.193-200.
- [15] Mayer, Y., Zang, B. and Azarpeyvand, M., 2019. Aeroacoustic characteristics of a NACA 0012 airfoil for attached and stalled flow conditions. In *25th AIAA/CEAS Aeroacoustics Conference* (p. 2530).
- [16] Harish, H.V., Arundeeep, M., Santhosh, N., 2019. Prediction Of Stalling Angle By Analysis Of Flow Over Symmetric Aerofoil. *Journal of Engineering Science and Technology* 2(2), pp.17-28.
- [17] Patil, B.S. and Thakare, H.R., 2015. Computational fluid dynamics analysis of wind turbine blade at various angles of attack and different Reynolds number. *Procedia Engineering*, 127, pp.1363-1369.
- [18] Hasegawa, M. and Sakaue, H., 2017. Drag reduction using hairy chemical coating on NACA 0012 airfoil in turbulent airflow. In *55th AIAA Aerospace Sciences Meeting* (p. 0283).
- [19] Venkatesan, S.P., Kumar, V.P., Kumar, M.S. and Kumar, S., 2018. Computational analysis of aerodynamic characteristics of dimple airfoil NACA 2412 at various angles of attack. *Idea*, 46, p.10.
- [20] Meghani, P., 2018. A 2D Aerodynamic Study on Morphing in The NACA 2412 Aerofoil. In *13th Research and Education in Aircraft Design Conference, Brno, Czech Republic*.
- [21] Havaladar, S.N., Pawar, S., Lele, A., Pradhan, R. and Rishi, A., Experimental Investigation of Lift for NACA 2412 Airfoil without Internal Passage with NACA 2412 Airfoil with Internal Passage in a Subsonic Wind Tunnel. *Journal of Aerospace Engineering & Technology*, 5(2), pp.27-33.
- [22] ANSYS Fluent 2019 R2. 2019.
- [23] Wilcox, D.C., 1988. Reassessment of the scale-determining equation for advanced turbulence models. *AIAA journal*, 26(11), pp.1299-1310.
- [24] Menter, F.R., 1994. Two-equation eddy-viscosity turbulence models for engineering applications. *AIAA journal*, 32(8), pp.1598-1605.
- [25] Launder, B.E., Spalding, D.B., 1974. The numerical computation of turbulent flows. *Computer Methods in Applied Mechanics and Engineering*. 3(2), pp.269–289.
- [26] Shih, T.H., Liou, W.W., Shabbir, A., Yang, Z. and Zhu, J., 1995. A new k- $\epsilon$  eddy viscosity model for high reynolds number turbulent flows. *Computers & fluids*, 24(3), pp.227-238.
- [27] Spalart, P. and Allmaras, S., 1992, January. A one-equation turbulence model for aerodynamic flows. In *30th Aerospace Sciences Meeting and Exhibit* (p. 439).
- [28] Walters, D.K. and Cokljat, D., 2008. A three-equation eddy-viscosity model for Reynolds-averaged Navier–Stokes simulations of transitional flow. *Journal of Fluids Engineering*, 130(12).
- [29] Walters, D.K. and Leylek, J.H., 2004. A new model for boundary layer transition using a single-point RANS approach. *J. Turbomach.*, 126(1), pp.193-202.
- [30] Langtry, R. and Menter, F., 2005, January. Transition modeling for general CFD applications in aeronautics. In *43rd AIAA Aerospace Sciences Meeting and Exhibit* (p. 522).
- [31] Menter, F.R., Langtry, R. and Völker, S., 2006. Transition modelling for general purpose CFD codes. *Flow, Turbulence and Combustion*, 77(1), pp.277-303.
- [32] Langtry, R.B. and Menter, F.R., 2009. Correlation-based transition modeling for unstructured parallelized computational fluid dynamics codes. *AIAA Journal*, 47(12), pp.2894-2906.
- [33] Contigiani, C.C., Colli, A.N., Pérez, O.G. and Bisang, J.M., 2020. The effect of a conical inner electrode on the mass-transfer behavior in a cylindrical electrochemical reactor under single-phase and two-phase (Gas-Liquid) swirling flow. *Journal of The Electrochemical Society*, 167(8), p.083501.

# Mechanical and Energy Absorption Performance of Expanded Perlite Foam-filled Steel Tubes

*Sadman Shahriar, Md. Arifuzzaman\*, Pranto Karua*

Department of Mechanical Engineering, Khulna University of Engineering & Technology, Khulna 9203, BANGLADESH

Received: March 13, 2022, Revised: March 22, 2022, Accepted: March 22, 2022, Available Online: March 24, 2022

## ABSTRACT

The main objective of this research is to manufacture expanded perlite (EP) foam-filled stainless steel tubes for energy absorption application and to investigate their physical and compressive behavior. Foam-filled steel tubes (FFT) were manufactured by consolidating expanded perlite/sodium silicate composite foam inside the tube. The EP particles of size 5-6 mm were taken for manufacturing FFTs. Two different sodium silicate solution to water (S/W) ratios and three compaction ratios (CR) were the manufacturing parameters of the foams. The manufactured FFTs were characterized for density, yield stress, plateau stress, energy absorption, and energy absorption efficiency. The compression test results showed that the foam filling improved the compressive properties and energy absorption ability of the steel tube significantly. The failure analysis along with the stress-strain curves was also conducted. The change in failure mechanism is found to be the reason for high energy absorption and energy absorption efficiency for high-density foam-filled tubes.

Keywords: Expanded Perlite, Composite Foam, Foam Filled Tube, Energy Absorption Capacity.



This work is licensed under a [Creative Commons Attribution-Non Commercial 4.0 International License](https://creativecommons.org/licenses/by-nc/4.0/).

## 1 Introduction

In recent years, the main concern of motor vehicles manufacturers is creating safer vehicles with minimum damage when there is an accidental impact [1]. It is necessary to provide an energy-absorbing structure at the front bumper to minimize the damage due to impact. To meet this criterion, different types of empty and composites foam tubes are used as energy-absorbing elements in the design of the vehicle e.g. crash box and anti-intrusion bars [2]. The empty profiles absorb the impact energy of crash at a very low force level and reduce the damage to the vehicle and are considered as mostly inefficient while kept under bending conditions as a high amount of deformation occurs in a small hinge. The crashworthiness of empty tubes under compressive loading conditions was investigated by many researchers [3]. The researches indicate that the energy absorption capacity of such tubes is limited. It is found that simply increasing the thickness of tube walls or implementing double walls tubes can result in increasing specific energy absorption [4]. But a great change is observed using foam filler material inside the tubes and investigations have been done depending on foam fillers to enhance the energy absorption and mechanical properties of thin-walled tubes. Studies have shown that the damping level of different components can be increased up to five times by inserting metallic foams in them [5]. Applications of such foam-filled tubes include anti-intrusion bars [6], crash boxes [7], frame of coach structures [8], or bumpers in the car industry [9]. Nonetheless, the non-metallic foam fillers may also be used for manufacturing foam filled-tubes for energy absorption applications where the cost and the lightweight are the main concerns. For example, Aktay, et al. [10] and Toksoy and Guden [11] studied polystyrene foam-filled aluminum tubes while Meguid, et al. [12] and Alia, et al. [13] investigated PVC foam-filled steel and aluminum tubes to observe the crashing and energy absorption behavior. Expanded perlite composite foams are newly developed low-cost materials which can be

manufactured using expanded perlite particles with various binders including sodium silicate solution [14], starch [15], epoxy [16], recycled polystyrene [17], sodium silicate solution with corn starch [18]. These low-cost composite foams may be a good alternative to be used as filler for steel tubes to enhance the mechanical and energy absorption capacity of the filled tubes.

Therefore, in this work, the expanded perlite/sodium silicate foam-filled stainless steel tubes were produced through a cost-effective compaction process. The quasi-static compressive test was conducted on the hollow and foam-filled tubes for characterization. The compressive properties, energy absorption per unit volume, and energy absorption efficiency were investigated based on the manufacturing parameters and the density to find out the effectiveness of expanded perlite/sodium silicate foam filling in the steel tube.



Fig. 1 Expanded perlite particles (5-6 mm)

## 2 Materials and Methodology

### 2.1 Materials

#### 2.1.1 Expanded Perlite

Expanded perlite (EP) was collected from China and separated into different size groups using sieves and particles of sizes 5-6 mm were selected for this work (see Fig. 1). The measured bulk density of the particles is 0.073 g/cm<sup>3</sup>.

\*Corresponding Author Email Address: [arif48@me.kuet.ac.bd](mailto:arif48@me.kuet.ac.bd)

### 2.1.2 Sodium Silicate Solution and Stainless Steel Tube

Sodium silicate solution (SSS) with weight ratio ( $\text{SiO}_2/\text{Na}_2\text{O}$ ) 3.22 and a density of  $1.38 \text{ g/cm}^3$  was diluted using drinking water and used as a binder for manufacturing expanded perlite composite foams. Two different SSS to water ratios (1:1 and 2:1 by weight) were considered in this work. Stainless steel (304) welded tubes of 25.4 mm outside diameter and 0.4 mm thickness were used as shown in Fig. 2. The measured tube bulk density is  $0.567 \text{ g/cm}^3$ .



Fig. 2 Hollow stainless steel tube (Diameter = 25.4 mm and thickness = 0.4 mm)

### 2.2 Specimen Preparation

A steel tube was taken and one side of it was covered by a polymer net so that the SSS can pass leaving wet EP particles trapped inside the tube. The tube was filled with the required amount of EP and soaked in the diluted SSS for 2 minutes for proper wetting of the particles. The tube with wet EP particles was taken out of the binder and the excess binder was drained out of the tube. The tube was then taken to the universal testing machine and the wet EP particles inside the tube were compacted using a plunger of a diameter slightly less than the internal diameter of the tube until the final height became 40 mm. The particles remained compacted for about 5 minutes and there was an insignificant spring back. The particles were compacted for three values of compaction ratios (e.g. 2.5, 3.0, and 3.5). Note that, the compaction ratio is the ratio of the height of the loose particle column to the final height after compaction. The specimens were then kept inside an oven at  $110^\circ\text{C}$  for curing until the weight loss became constant. The hollow part of the tube with no particles was cut by a hand grinder and both sides of the tube were flattened using a CNC lathe. The specimens may be identified as S\_X\_Y where 'S' for sample, the number in place of X and Y indicates SSS/Water (S/W) ratio and compaction ratio (CR).

### 2.3 Mechanical Testing

The uniaxial compression test was conducted on a Universal Testing Machine (Model – Controls 50-C10B/PR) with a loading rate (5 N/s) to investigate the compressive and energy absorption behavior. Four samples for each configuration have been tested.

## 3 Results and Discussion

### 3.1 Physical Properties

The mass fractions of constituents and densities of the prepared composites are given in Table 1. Filled tube and foam density are plotted as a function of compaction ratio for two S/W ratios in Fig. 3. Both foam and filled tube density increased linearly with increasing compaction ratio for both binder contents. The least-square lines and  $R^2$  values are also shown in Fig. 3. High linearity is represented by higher  $R^2$  values. The density is higher for a high S/W ratio for all compaction ratios

because the EP particles were exposed to a high concentration of sodium silicate during manufacturing. The high value of the mass fraction of sodium silicate in foam (see Table 1) is also seen for a high S/W ratio because of the same reason.

Table 1 Mass fractions and density of the foam-filled steel tube (Average values calculated from three specimens are given in the table).

Sample No.	Mass fraction of EP in foam (%)	Mass fraction of sodium silicate in foam (%)	Mass fraction of foam	Mass fraction of steel tube	Filled tube density ( $\text{g/cm}^3$ )	Foam density ( $\text{g/cm}^3$ )
S_1_2.5	72.53	27.47	31.56	68.44	0.83	0.27
S_1_3.0	70.20	29.80	37.17	62.84	0.90	0.35
S_1_3.5	64.24	35.76	41.66	58.34	0.98	0.43
S_2_2.5	44.90	55.11	42.32	57.68	0.99	0.44
S_2_3.0	46.54	53.47	46.90	53.11	1.07	0.52
S_2_3.5	47.58	52.42	49.11	50.90	1.12	0.58

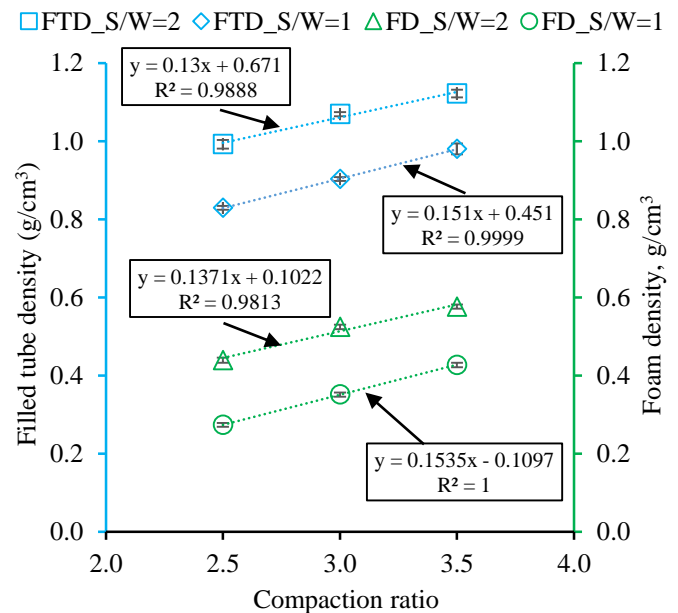


Fig. 3 Filled tube density and foam density as a function of CRs for both S/W ratios. Standard deviations calculated from four specimens are given as error bars.

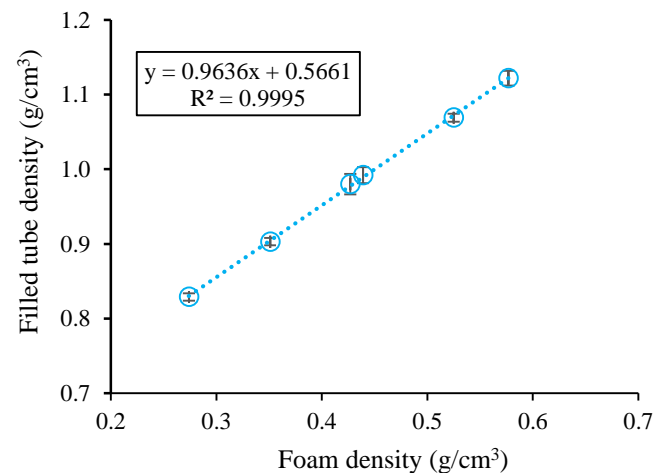


Fig. 4 Filled tube density as a function of foam density

In Fig. 4, the filled tube density is plotted as a function of foam density irrespective of S/W ratios. It is seen that the filled tube density increased linearly showing a high correlation coefficient with increasing foam density regardless of the S/W ratio and CR.

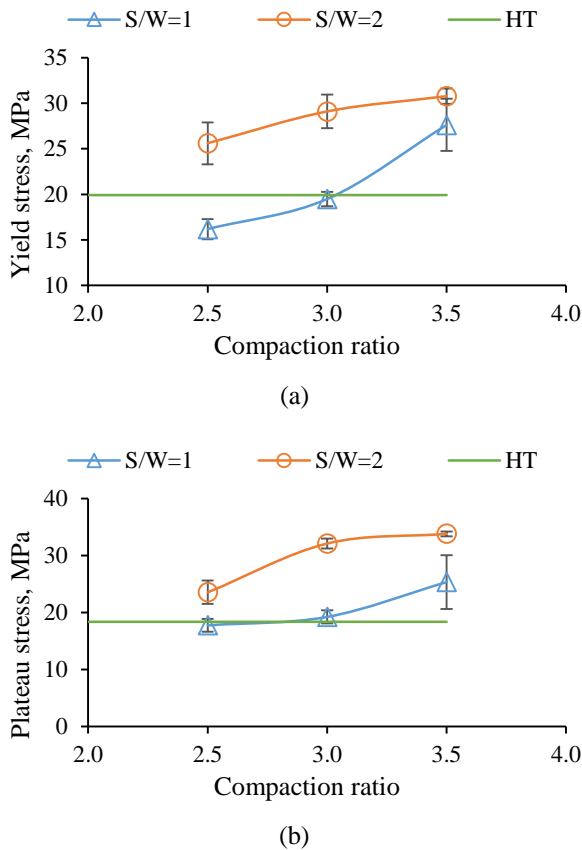


Fig. 5 Compressive properties of the HT and tubes filled with EP/SSS foam for different CRs for S/W ratios: (a) Yield stress; and (b) Plateau stress (20-40% strain).

### 3.2 Compressive Properties

#### 3.2.1 Effect of Foam Manufacturing Parameters on Compressive Properties of Foam-filled Tubes (FFT)

In Fig. 5, the compressive properties are plotted as a function of CR for both S/W ratios. It is seen from Fig. 5(a) that the yield stress (YS) increases consistently with the increasing CR for both S/W ratios. The YSs for S/W ratio = 1 at compaction ratios 2.5 and 3.0 appear to be lower than that of the hollow tube (HT). There may be two reasons for this to occur i. e. the prestressing of the tube during the compaction of perlite composite foam inside the tube and the load-bearing capacity of the foam is not sufficient to compensate for the prestressing of the tube. Nonetheless, for the S/W ratio = 1 and CR = 3.5, the YS is higher than that of the HT because the load-bearing capacity of the foam is now sufficient to compensate for the prestressing of the tube. On the other hand, for S/W ratio = 2, all FFTs show higher YS when compared with the YS of HT because of the higher binder content in the foam. It should be noted that the high compaction ratio and high binder content increases the compressive strength of the perlite/sodium silicate foams [14]. The plateau stress (PS) is calculated by averaging the stress from 20% strain to 40% strain and plotted as a function of CR in Fig. 5(b). It is seen that the PS also increases with increasing compaction ratio for both S/W ratios. The plateau stress for S/W ratio = 1 for CR = 2.0 and

2.5 are very close to the PS of the HT because of the same reason described for YS. Again the PS for S/W ratio = 2 is higher than the HT due to the higher strength of the foams.

Fig. 6 shows the energy absorption (EA) up to 40% strain and the energy absorption efficiency (EAE) at 40% strain of the HT and FFTs as a function of CRs for both S/W ratios. The EA increases consistently with increasing CR for both S/W ratios. The EA is significantly higher in the FFTs as compared to the HT [see Fig. 6(a)] except for the FFT with the foam made of S/W ratio = 2.5 and CR = 2.5. The FFTs with low S/W ratios and low CRs (i. e. S/W=1 with CR=2.5 and 3.0; S/W=2 with CR=2.5) show less EAE and FFTs with high S/W ratios and high CRs (i. e. S/W=1 with CR=3.5; S/W=2 with CR = 2.5 and 3.0) show higher EAE compared to the EAE of the HT [see Fig. 6(b)]. The less EAE for some FFTs is attributed to the low load-bearing capacity as well as the prestressing of the tube during FFT manufacturing.

Therefore, it is seen that the manufacturing parameters of perlite/sodium silicate composites i.e. S/W ratio and CR play an important role in the improvement of mechanical properties of FFTs.

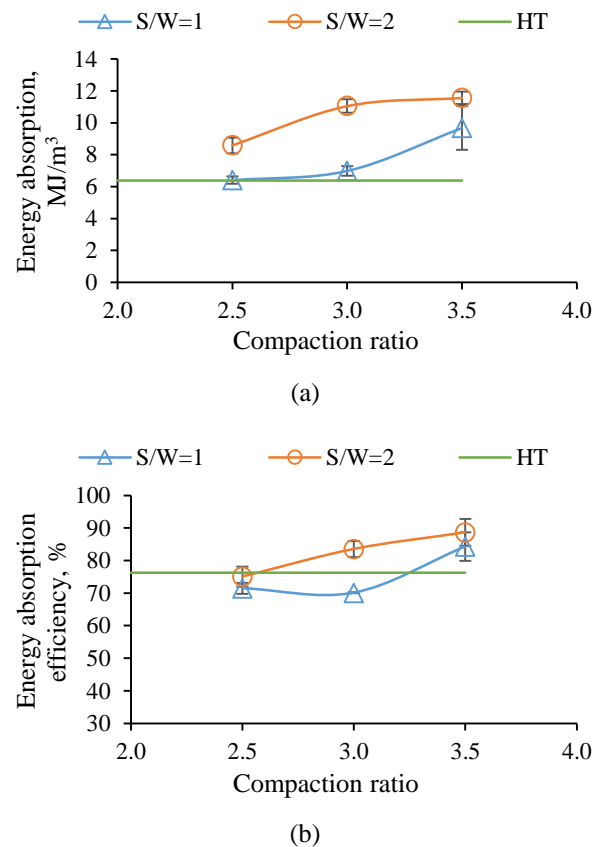


Fig. 6 (a) Energy absorption per unit volume up to 40% strain and (b) Energy absorption efficiency at 40% strain as functions of CR for both S/W ratios.

#### 3.2.2 Effect of Density on Compressive Properties of the Foam-filled Tubes

In Fig. 7, the YS and PS are plotted as a function of tube density for both HT and FFTs. Both the YS and PS increased highly linearly with increasing the density of the tube as indicated by the high  $R^2$  values. The change in the density of the FFTs is due to the change in the foam density inside the tube because the steel tube size and material are the same for all FFTs. Therefore it is the foam density that caused the increase in both

YS and PS of the FFTs. So, the density of the foam inside the FFTs is highly responsible for the improvement of the compressive properties of the FFTs. The EA and EAE are plotted as a function of tube density in Fig. 8. It is seen that the EA increases linearly with increasing density with a high R<sup>2</sup> value. Although the EAE increases with increasing tube density, the linearity is not high as indicated by the low R<sup>2</sup> value.

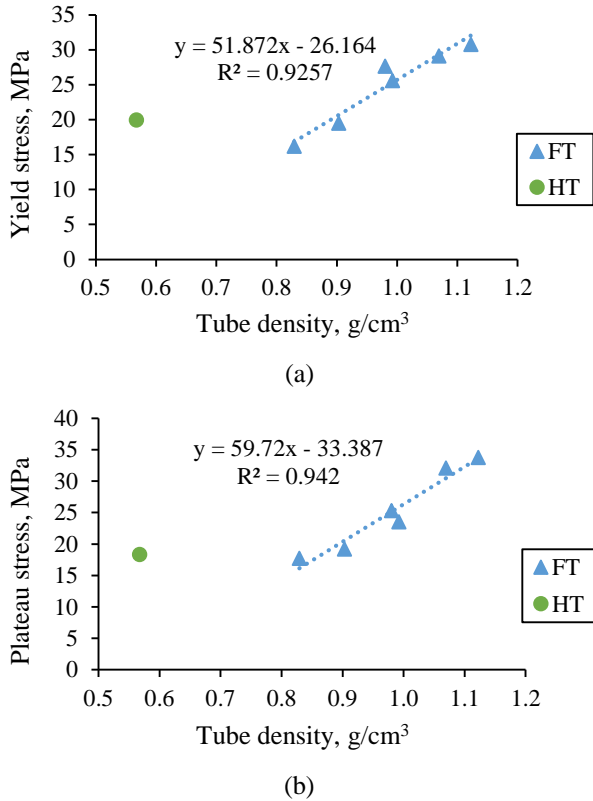


Fig. 7 Compressive properties of the tubes with the variation of tube density: (a) Yield stress; and (b) Plateau stress (20–40% strain).

From the above results, it can be said that the compressive properties of the FFTs improved significantly when the density of the foam inside the tube is increased as compared to the HT. The percentage increase in YS, PS, EA, and EAE in the highest density FFTs are seen to be 54.49%, 83.84%, 81.63%, and 16.32% respectively compared with the HT. The improvements in mechanical properties and energy absorption occurred with a cost of only an 8.34% decrease in specific energy absorption.

The variation of EAE of the FFTs and HT with strain is shown in Fig. 9. In general, it appears that after the peak stress is reached, the EAE increases with increasing strain for HT and FFTs. It can be seen that the EAE is consistently higher for FFTs filled with perlite foam with CR = 3.0 and 3.5 when compared with EAE of HT throughout the range of strain studied [see Fig. 9(a)]. Though the EAE of S<sub>1</sub>\_3.0 coincides with HT's EAE, it remains higher for S<sub>1</sub>\_3.5 than HT's EAE. For samples made of S/W ratio = 2, FFTs show higher EAE compared with HTs for the whole strain range after the peak stress (see Fig. 10) is reached. Therefore, the perlite foam filling has a significant impact in improving the energy absorption efficiency of the tube.

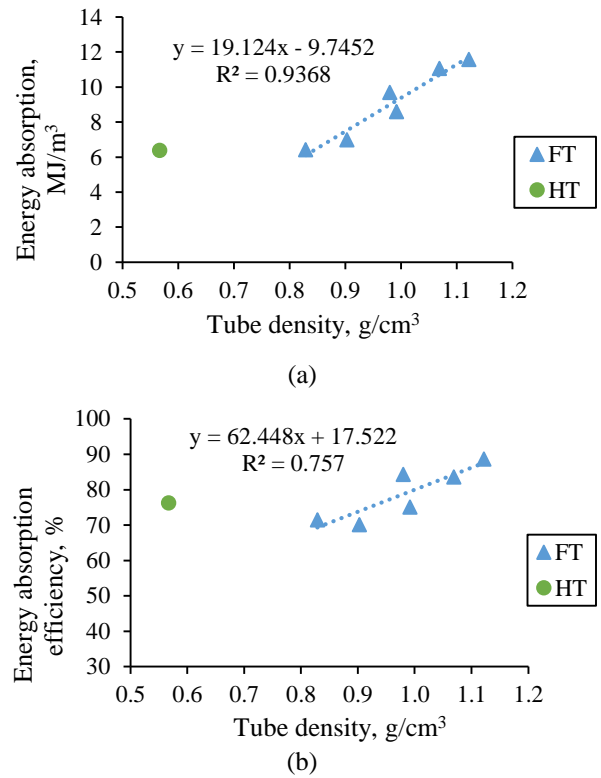


Fig. 8 (a) Energy absorption per unit volume up to 40% strain and (b) Energy absorption efficiency at 40% strain as a function of tube density.

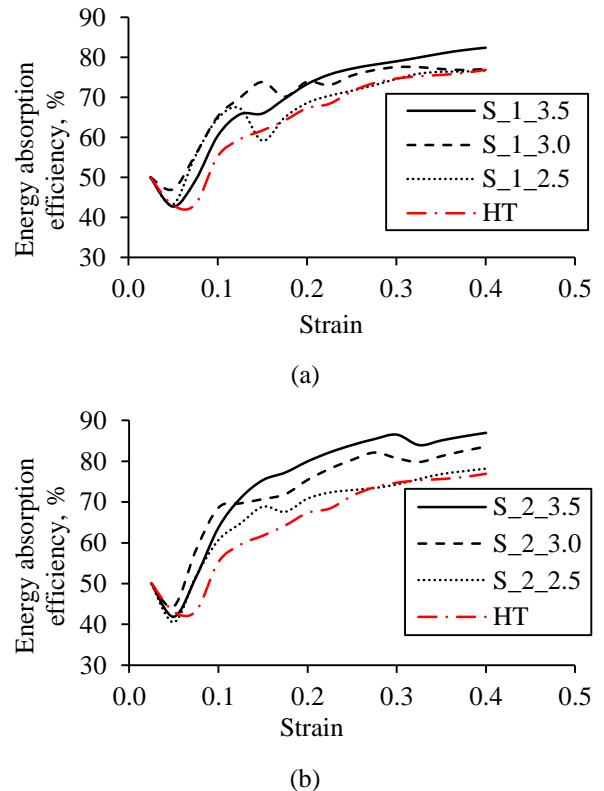
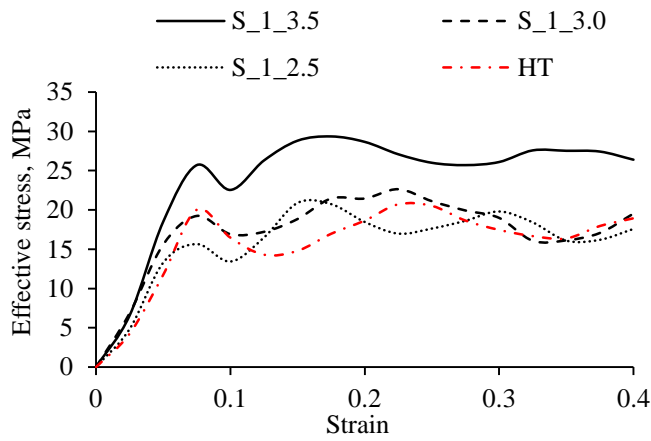


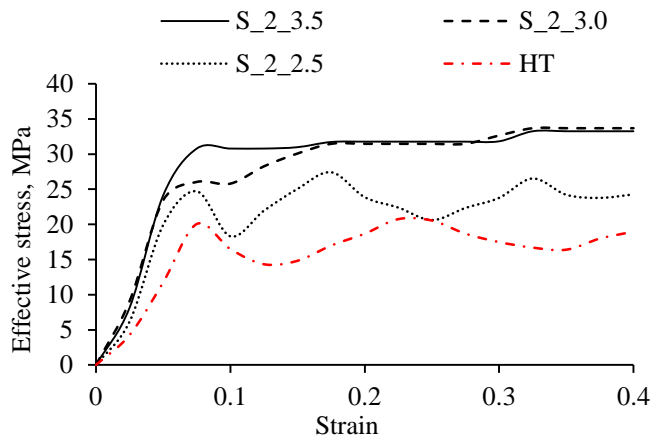
Fig. 9 Variation of energy absorption efficiency with strain for (a) S/W ratio = 1 and (b) S/W ratio = 2.

3.2.3 Effective Stress-Strain Curves and Failure Analysis

The effective stress versus strain curves for the HT and FFTs are shown in Fig. 10. Stress increases linearly with increasing strain up to a peak (i. e. yield point). After that, the curve for the hollow tube shows two peaks for the range of strain studied. Each peak is associated with each three-fold buckling failure of the tube due to compression as shown in Fig. 11(a). Specimen with S/W ratio = 1 and CR = 2.5 shows three peaks and CR = 3.0 shows two peaks in their respective stress-strain curves but for the specimen with S/W ratio = 1 and CR = 3.5, the curve shows a single peak and then a plateau in the stress-strain curve. However, the failure for the HT is three-fold buckling and for the FFTs with the S/W ratio = 1 consists of a single ring formation and then three-fold buckling as shown in Fig. 11(c) – (f).



(a)



(b)

Fig. 10 Effective stress-strain curves for (a) S/W ratio = 1 and (b) S/W ratio = 2.

On the other hand, the stress-strain curve for S/W ratio = 2, the FFT with CR = 2.5 shows three peaks instead of two peaks for HT although the location of the peak in the stress-strain curve is different. In this case, the failure of the specimen is similar to the FFTs for S/W ratio = 1. For S/W ratio = 2 and CRs = 3.0 and 3.5, the stress-strain curves do not show any peak rather a plateau [see Fig. 11(g)] is seen for the strain range studied. The three-fold buckling failure is eliminated and the failure occurred by the formation of rings (concertina) as seen in Fig. 11(h) and (i). The change in failure mode is the reason for the high energy absorption and energy absorption efficiency of the high-density foam-filled tubes.



Fig. 11 (a) Hollow tube; (b) Foam filled tube; (c) Crashed hollow tube; (d) - (i) Some photographs of the crashed FFT specimens after compression tests made of S/W ratio = 1 and S/W ratio = 2 for various compaction ratios.

4 Conclusion

The work is focused on the development and characterization of perlite foam-filled steel tubes for energy absorption application. The findings of the research can be summarized as:

- The compressive properties, energy absorption, and energy absorption efficiency of the foam-filled tubes significantly depend on the foam manufacturing parameters such as binder content and compaction ratio.
- The percentage increase in yield stress, plateau stress, and energy absorption in the highest density foam-filled tube is found to be 54.49%, 83.84%, and 81.63% respectively compared with those of the hollow tube. The improvements in mechanical properties and energy absorption occurred with a cost of only an 8.34% decrease in specific energy absorption.
- The energy absorption efficiency is found to be increasing with increasing strain and EAE is higher than that of the hollow tube throughout the range of strain studied except for the low-density foams.
- For the high-density foam-filled tubes, the failure mechanism is changed from three-fold buckling to the formation concertina which is the reason for the high energy absorption capacity of those foam-filled tubes.

**Nomenclature**

Parameters	Acronyms
Expanded perlite	EP
Sodium silicate solution	SSS
Foam-filled tube	FFT
Hollow tube	HT
Yield stress	YS
Plateau stress	PS
Energy absorption	EA
Energy absorption efficiency	EAE
Sodium silicate solution to water ratio	S/W ratio
Compaction ratio	CR

**Acknowledgements**

The authors acknowledge the financial support for this work from Khulna University of Engineering & Technology.

**References**

- [1] Xiao, Z., Fang, J., Sun, G. and Li, Q., 2015. Crashworthiness design for functionally graded foam-filled bumper beam. *Advances in Engineering Software*, 85, pp.81-95.
- [2] Zarei, H.R. and Kröger, M., 2007. Crashworthiness optimization of empty and filled aluminum crash boxes. *International Journal of Crashworthiness*, 12(3), pp.255-264.
- [3] Abramowicz, W., 2003. Thin-walled structures as impact energy absorbers. *Thin-walled structures*, 41(2-3), pp.91-107.
- [4] Kavi, H., Toksoy, A.K. and Guden, M., 2006. Predicting energy absorption in a foam-filled thin-walled aluminum tube based on experimentally determined strengthening coefficient. *Materials & design*, 27(4), pp.263-269.
- [5] Strano, M., Marra, A., Mussi, V., Goletti, M. and Bocher, P., 2015. Endurance of damping properties of foam-filled tubes. *Materials*, 8(7), pp.4061-4079.
- [6] Strano, M., Villa, A. and Mussi, V., 2013. Design and manufacturing of anti-intrusion bars made of aluminium foam filled tubes. *International Journal of Material Forming*, 6(1), pp.153-164.
- [7] Zarei, H.R. and Kröger, M., 2008. Optimization of the foam-filled aluminum tubes for crush box application. *Thin-walled Structures*, 46(2), pp.214-221.
- [8] Cazzola, G.J., Alcalá Fazio, E. and Izquierdo, F.A., 2013. Study of the bending response of metal foam-filled beams applied to enhance the rollover behaviour of coach structures. *International Journal of Crashworthiness*, 18(6), pp.620-632.
- [9] Ahmad, Z. and Thambiratnam, D.P., 2009. Application of foam-filled conical tubes in enhancing the crashworthiness performance of vehicle protective structures. *International Journal of Crashworthiness*, 14(4), pp.349-363.
- [10] Aktay, L., Toksoy, A.K. and Güden, M., 2006. Quasi-static axial crushing of extruded polystyrene foam-filled thin-walled aluminum tubes: experimental and numerical analysis. *Materials & Design*, 27(7), pp.556-565.
- [11] Toksoy, A.K. and Güden, M., 2005. The strengthening effect of polystyrene foam filling in aluminum thin-walled cylindrical tubes. *Thin-walled structures*, 43(2), pp.333-350.
- [12] Meguid, S.A., Attia, M.S. and Monfort, A., 2004. On the crush behaviour of ultralight foam-filled structures. *Materials & Design*, 25(3), pp.183-189.
- [13] Alia, R.A., Guan, Z., Jones, N. and Cantwell, W.J., 2015. The energy-absorption characteristics of metal tube-reinforced polymer foams. *Journal of Sandwich Structures & Materials*, 17(1), pp.74-94.
- [14] Arifuzzaman, M.D. and Kim, H.S., 2014, December. Development of new perlite/sodium silicate composites. In *International Conference on Mechanical, Industrial and Energy Engineering (ICMIEE)*, Khulna University of Engineering & Technology, Khulna, Bangladesh.
- [15] Shastri, D. and Kim, H.S., 2014. A new consolidation process for expanded perlite particles. *Construction and Building Materials*, 60, pp.1-7.
- [16] Allameh-Haery, H., Kisi, E. and Fiedler, T., 2017. Novel cellular perlite-epoxy foams: Effect of density on mechanical properties. *Journal of Cellular Plastics*, 53(4), pp.425-442.
- [17] Al Abir, A., Faruk, M.O. and Arifuzzaman, M. 2021, December. Novel Expanded Perlite Based Composite using Recycled Expanded Polystyrene for Building Material Applications. In *International Conference on Mechanical, Industrial and Energy Engineering (ICMIEE)*, Khulna University of Engineering & Technology, Khulna, Bangladesh.
- [18] Adhikary, P., Arifuzzaman, M. and Kabir, E., 2020. Compressive properties of expanded perlite based particulate composite for the application in building insulation Board. *Journal of Engineering Advancements*, 1(1), pp.01-05.

# Fundamental Study of CH<sub>4</sub>-Air Combustion under an Axisymmetric Small-scale Rectangular Combustor using Computational Modeling

Karan Gaglani<sup>1</sup>, Md. Amzad Hossain<sup>2,\*</sup>

<sup>1</sup>Department of Aerospace Engineering, Embry-Riddle Aeronautical University, Prescott, AZ-86301, USA

<sup>2</sup>Department of Mechanical Engineering, Embry-Riddle Aeronautical University, Prescott, AZ-86301, USA

Received: February 13, 2022, Revised: March 25, 2022, Accepted: March 25, 2022, Available Online: March 28, 2022

## ABSTRACT

The optimization of the design and operating conditions of industrial combustors depends on the fundamental study of combustion dynamics and flow behaviors. Complete combustion increases the thermal efficiency as well as reduces the emission significantly. A study of this kind also allows exploring alternative fuels that would increase the combustion efficiency thus the life cycle of the systems. To develop a highly-performed combustion system for power plants and/or rocket engines, fundamental research under an axisymmetric small-scale combustor is considered in this study. The  $k-\varepsilon$  (2 Eqn.) and species transport model (STM) are used to study the flow turbulence and combustion behavior, respectively. A Parallel flow injection configuration of fuel and air is considered. Combustion behavior is investigated at a wide range of fuel and air flow rate conditions while keeping the air slot dimension (240 mm) and fuel injection slot diameter (10 mm) constant. The fuel velocity (FV) and air velocity (AV) are changed from 2 m/s to 30 m/s so that a better test matrix could be proposed. At each run, turbulence, the flame temperature, reaction heat release rate, mass fraction of CO<sub>2</sub>, etc are studied. It is seen that the combustion temperature increases with the increase in fuel injection velocity. The static flame temperature varies from 1855 K (min.) to 2350 K (max.) and falls within the standard limits of CH<sub>4</sub>-Air combustion. The mass fraction of CO<sub>2</sub> is found to be within the acceptable limit (0.121 to 0.153). The heat of the reaction changes from 1.2 W (min.) to 15.6 W (max.) at variable  $Re_{air}$  and  $Re_{CH_4}$  conditions. It is observed that the computational models used in this study are capable of predicting the flow and combustion behaviors accurately.

Keywords: Axisymmetric Combustor, Parallel Flow Injection, Species Transport Model, Flame Temperature, Heat of Reaction, Emission.



This work is licensed under a [Creative Commons Attribution-Non Commercial 4.0 International License](https://creativecommons.org/licenses/by-nc/4.0/).

## 1 Introduction

Combustion is a chemical reaction in which different forms of energy are produced. Daily, the amount of CO<sub>2</sub> released is increasing. Thus research is being done to make the combustion processes more efficient to lower their impact on the environment. The US has been showing a trending growth in oil demand followed by China [1]. According to the International Energy Association (IEA, 2020 Edition) [1], the US had produced a 5.41GT (Gigaton) of CO<sub>2</sub> in 2018. The US had experienced an increase of ~ 3% unlike the European Union and Japan which have continued the decline. Therefore, the fundamental study of combustion is crucial for the development of clean energy technologies for power plants, airplane industries, rockets, etc.

Researchers have been doing extensive research developing highly-performed combustors and green combustion technologies. There is a lot of experimental and CFD research on premixed and non-premixed combustion. For example, Hossain et al. [2]-[5] have performed laser diagnostics (PLIF and PIV) and premixed combustion modeling to understand the flow and flame interaction at a wide range of Reynolds numbers and equivalence ratio conditions. They have developed the flame front tracing tools and developed optimum operating conditions for lab-scale high-speed combustion tests. Hamzah [6] compared the combustion performance of propane and methane inside an axial combustor using a non-premixed combustion model. They showed that the maximum temperature for propane is less than the methane and NO<sub>x</sub> production is mostly controlled

by the temperatures. Ibrahim [7] studied the effect of radiation on the flame size and overall flame performance in a methane-air combustion medium. They found that the air swirl number and the combustor exit to Swirler diameter ratio adversely influenced the flame temperature and flame length. Pitsch et al. [8] have performed a flamelet formulation model and investigated the effect of exact differential diffusion on the flame performance. They showed that the accurately measured Lewis number could be used to predict the scalar dissipation rate, pressure, and boundary conditions. Matalon et al. [9] have investigated the combustion instabilities in both premixed and non-premixed combustion. They studied the role of different types of diffusion, thermal expansion, and heat losses on flame instabilities. They showed that the instabilities in premixed combustion are mostly controlled by the thermal expansion, whereas, in diffusion (non-premixed) flame, instabilities are controlled by the thermal-diffusive effects. Lacaze et al. [10] have performed non-premixed combustion based on the flame structure analysis. They have investigated the flame stability in a liquid rocket engine near critical and supercritical conditions. They found that the flame stability is greatly controlled by the pressure, local strain, and temperature variations. Barths et al [11] have investigated the combustion performance of direct injection diesel engines using flamelet-based non-premixed combustion modeling. They proved that the multiple flamelets model (MFM) improves the understanding of the ignition phase, combustion pressure, heat release, and emission characteristics.

\*Corresponding Author Email Address: [hossaim4@erau.edu](mailto:hossaim4@erau.edu)

Hossain et al. [12] have studied the effect of Ultra Low-swirl Burner (LSB) ( $S = 0.17$ ) on the combustion behavior of non-premixed methane-air mixture at low-to-high Re conditions. It was seen that the swirl number and Re play a significant role in combustion stability and thermal performance.

Although there are enormous scientific resources on non-premixed combustion, the applicability of those models is severely limited. In non-premixed combustion, the mass fractions are assigned in the model. There is no control over combustion reactions or combustion kinetics. Therefore, how species are generated, transformed through the combustion process, and how the diffusion controls the chemical kinetics can not be entirely explained by the non-premixed (NPM) combustion model. It is the species transport model (STM) that provides more information on species-derived chemical kinetics of the combustion. However, the scholarly resources on species transport model (STM)-based combustion are very limited, especially those for industrial applications. For example, Kassem et al. [13] have utilized the eddy dissipation model along with the species transport equations and studied the turbulent combustion of methane-jet flame. They showed that the ANSYS fluent overpredicts the flame mean temperature and underpredicts the flame length at the centerline of the combustor. Kongre et al. [14] have performed CFD and experimental tests to validate the combustion behavior of a direct ignition diesel engine.

Furthermore, the scientific resources on the design and optimization of industrial combustors are very limited. For example, Enagi et al. [15] have used the species transport model and non-premixed combustion model with laminar finite rate technique. They have optimized the design and performance criterion of the combustor. Davis et al. [16] have developed a comprehensive kinetic model to accurately predict H<sub>2</sub>-CO combustion data. D'Errico et al. [17] performed CFD modeling to design and optimize the combustion system for modern heavy-duty diesel engines. The information regarding the safe experimental methodology, optimum operating conditions, or test matrix is still limited. Hossain et al. [18] have studied the fundamentals of CH<sub>4</sub>-Air combustion in a cross-flow configuration under a small-scale combustor using the STM. The diffusion flame and its interaction with flow characteristics were studied at limited operating conditions. A more fundamental combustion study needs to be done to develop a next-generation highly-performed combustor for the industry.

To address the above issues, the species transport model (STM) is used to study the CH<sub>4</sub>-Air combustion under an axisymmetric small-scale combustor. The combustion is performed at equivalence ratio ( $\phi$ ) = 1.0 and a wide range of CH<sub>4</sub> and Airflow conditions. The global combustion characteristics such as static flame temperatures, heat release rates, and mass fraction of CO<sub>2</sub> are investigated. Flow characteristic such as turbulent Intensity (I) is also measured. A relation has been made between the combustion and flow characteristics at a wide range of methane and airflow velocities. The ongoing work aims to optimize the test operating conditions of the proposed axisymmetric combustor.

## 2 Computational Methodology

For this study, a combustor with a length of 1800 mm and a width of 250 mm is examined. The authors come up with these dimensions based on the findings of previous research articles which could be found elsewhere [18]. As illustrated in Fig. 1, the fuel and air injection holes both are accommodated within the width of the combustor. The test operating conditions are

optimized by maintaining the fuel slot height at 10 mm and the air slot height at 240 mm. The surface mesher and smooth transition inflation are used to create the mesh. Mesh Independence study is carried out by refining the grid size, grid growth rate, grid aspect ratios, etc. Based on the CFD analysis, going over mesh elements of 203424 and nodes of 204330 does not significantly affect the flow and flame characteristics. Considering the mesh independence study, the authors decided to use the mesh elements of 203424 and nodes of 204330 for this research (Fig. 2).



Fig. 1 2D Axisymmetric Combustor



Fig. 2 The Meshing Domain

To discretize the fluid flow governing equations, the finite volume method (FVM) is utilized. A pressure-based, absolute, steady, and 2D axisymmetric space is considered in this study. The Energy equation and volumetric reaction are turned ON. Standard k- $\epsilon$  (2 Eqn.) and species transport equation are used for turbulence and combustion study. For the k and  $\epsilon$  [18], the following two transport equations are used:

$$\frac{\partial}{\partial t} (\rho k) + \frac{\partial}{\partial x_i} (\rho k u_i) = \frac{\partial}{\partial x_j} \left[ \left( \mu + \frac{\mu_t}{\sigma_k} \right) \frac{\partial k}{\partial x_j} \right] + G_k + G_b + \rho \epsilon - Y_M + Y_k \quad (1)$$

$$\frac{\partial}{\partial t} (\rho \epsilon) + \frac{\partial}{\partial x_j} (\rho \epsilon u_j) = \frac{\partial}{\partial x_i} \left[ \left( \mu + \frac{\mu_t}{\sigma_\epsilon} \right) \frac{\partial \epsilon}{\partial x_i} \right] + C_{1\epsilon} \frac{\epsilon}{k} (G_k + C_{2\epsilon} G_b) - C_{2\epsilon} \rho \frac{\epsilon^2}{k} + S\epsilon \quad (2)$$

Where,  $G_k$  and  $G_b$  are the turbulent kinetic energy (TKE) generation due to the average velocity gradient and buoyancy forces, respectively,  $\mu_t$  is the turbulent viscosity, and  $\mu$  is the molecular viscosity. The source terms used for the energy transport phenomena are  $\sigma_k$  and  $S\epsilon$ . The  $Y_M$  term in the k equation shows the contribution of fluctuating dilation to the overall dissipation rate. In the  $\epsilon$  equation,  $C_{1\epsilon}$ ,  $C_{2\epsilon}$  and  $C_{3\epsilon}$  are the volume fraction constants and  $S\epsilon$  is the user-defined source terms.

The species transport model (STM) is used to account for the effect of chemical reactions and the nature of components and species. The general equation for the species transport model is expressed below [18]-[19],

$$\frac{\partial}{\partial t} (\rho Y_i) + \nabla \cdot (\rho \vec{v} Y_i) = -\nabla \cdot \vec{J}_i + R_i + S_i \quad (3)$$

Where  $\vec{J}_i$  is the diffusion flux of species i due to the change in concentration and temperature gradients,  $R_i$  is the net rate of production of species i by the chemical reaction,  $Y_i$  is the local mass fraction of species,  $S_i$  is the rate of creation by additional sources such as particulate, soot, emission, etc. The  $R_i$  is

determined by Eddy-Dissipation Model (EDM). The details about EDM could be found elsewhere [18]. The following equation is used to predict the mass diffusion in a turbulent flow,

$$\vec{J}_i = -\left(\rho D_{i,m} + \frac{\mu_t}{Sc_t}\right) \nabla Y_i - D_{T,i} \frac{\nabla T}{T} [Turbulent Flow] \quad (4)$$

Where  $D_{T,i}$  is the thermal diffusion coefficient,  $D_{i,m}$  is the mass diffusion coefficient,  $Sc_t$  is the turbulent Schmidt number,  $D_t$  is the turbulent diffusivity. The detail of those models could be found in [12], [18]-[20]. The boundary conditions and solution schemes used for this study are listed in Table 1 and Table 2.

Table 1 The Boundary Conditions Used in STM

Parameters	Conditions/Ranges
Equivalence Ratio ( $\phi$ )	1.0 [Stoichiometric Condition]
Wall	Stationary Wall with Standard Wall Roughness
Outlet	Pressure Outlet
$Re_{CH_4}$	1.2 E+3 to 1.2 E+4
$Re_{Air}$	3.2 E+4 to 3.2 E+5

Table 2 The Solution Schemes Used in STM

Parameters	Solution Schemes
Solution Initialization	Hybrid Initialization
Scheme Used	Couple
Spatial Discretization	Pressure: Second Order Momentum/TKE/TDR/CH <sub>4</sub> /O <sub>2</sub> /CO <sub>2</sub> /H <sub>2</sub> O/ Energy: Second-Order Upwind

### 3 Numerical Uncertainties and Validation

The numerical uncertainties are calculated to see how off the results are from the true value (target). The variable input values are implemented to measure the numerical sensitivity. The repeated measurements are performed to characterize the random (precision) uncertainty. The overall uncertainty varies between 0.05% and 0.90%. The calculated numerical uncertainties fall within the acceptable standard limits of uncertainties ( $\leq 5\%$ ). Thus, the results presented in this paper are deemed to be valid. The numerical uncertainty is listed in Table 3.

Table 3 The Numerical Uncertainties in Computational Results

Categories	Uncertainties (%)	Overall Uncertainty (%)
Turbulent Intensity	0.22%-0.45%	
Static Temperature	0.15%-0.25%	
Heat of Reaction	0.55%-0.90 %	0.05%-0.90%
Mass Fraction of CO <sub>2</sub> , H <sub>2</sub> O, and N <sub>2</sub>	0.05%-0.07%	

The authors do believe that the experimental tests need to be done to further validate the results presented in this paper. The authors are still working on the project and aiming to perform the experimental tests soon.

### 4 Results and Discussions

This paper focuses on the CFD modeling of stoichiometric methane-air combustion ( $\phi = 1$ ) under a small-scale rectangular combustor at a wide range of methane and airflow conditions. The combustion study is performed using the species transport model (STM). To start the iteration in CFD, FV of 30 m/s ( $Re_{CH_4} = 1.8 E+4$ ) is considered as an arbitrary reference value. Then AV is changed from 2 m/s to 20 m/s ( $Re_{Air} = 3.2 E+4$  to  $3.2 E+5$ ). This is how the optimum range of AV is decided. Similarly, to get the optimum range of FV, AV = 30 m/s ( $Re_{Air} = 4.9 E+5$ ) is considered as an arbitrary reference value. The FV is changed from 2 m/s to 20 m/s ( $Re_{CH_4} = 1.2 E+3$  to  $1.2 E+4$ ). The authors are interested to present the flow and flame characteristics at low operating conditions first. After that, the flow and combustor behavior at moderate-to-high operating conditions will be discussed.

#### 4.1 Flow and Flame Characteristics at Low $Re_{Air}$ and $Re_{CH_4}$

##### 4.1.1 Flow and Flame Characteristics at $Re_{Air} = 3.2 E+4$ (AV = 2 m/s) when $Re_{CH_4} = 1.8 E+4$ (FV = 30 m/s)

The flow inside a combustor is controlled by turbulence or diffusion. Also, the relative behavior of fluctuating velocity component over mean velocity is important for flow characterization. To address these, the turbulent intensities (I) are investigated. The turbulent intensity reaches a minimum of 4.2 (%) and a maximum of 700.1 (%) as shown in Fig. 3. The turbulent intensity is found to be around ~350% in the ignition zone. The higher turbulence in the ignition zone indicates better mixing and entrainment. The better mixing confirms the flame anchoring in the ignition zone.

The static temperature contour shows the instantaneous flame temperature of the methane-air combustion. As expected, the flame temperature reaches 2167 K at  $Re_{Air} = 3.2 E+4$  (Fig. 4). It is seen that the temperature is well distributed inside the combustor. The flame expansion is seen to be high. The flame is expanded from the ignition point to the downstream direction. However, a better lateral expansion could be achieved if the flow swirl is further improved at the combustor inlet.

The heat released during the exothermic reaction defines the soundness of the combustion. To understand the heat transfer and overall heat generation, the heat of reaction contour is studied. In this case, the heat of reaction ( $\Delta H$ ) reaches a max of 15.2 W (Fig. 5). The thermal energy generation is maximized near the upstream of the combustor, especially in the mixing point or ignition point.

The study of mass fractions (mf) of the products is very important especially to determine the completeness of the combustion. The mass fraction of CO<sub>2</sub>, H<sub>2</sub>O, and N<sub>2</sub> are presented in Fig. 6. In the methane-air flame, the maximum  $mf_{CO_2}$ ,  $mf_{H_2O}$ , and  $mf_{N_2}$  are found to be 0.142, 0.117, and 0.767 respectively. The mass fractions of the products are within the acceptable limits of CH<sub>4</sub>-Air combustion as stated in [19]-[20]. Therefore, it is indicating that the combustion is complete and there is no unburn mixture present in the system.

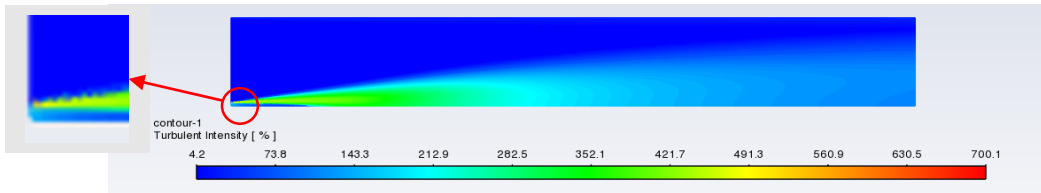


Fig. 3 Contour of the turbulent intensity at  $Re_{Air} = 3.2 E+4$  ( $AV = 2$  m/s)

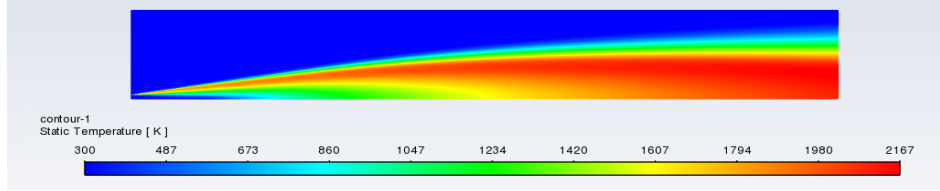


Fig. 4 Contour of the static temperature at  $Re_{Air} = 3.2 E+4$  ( $AV = 2$  m/s)

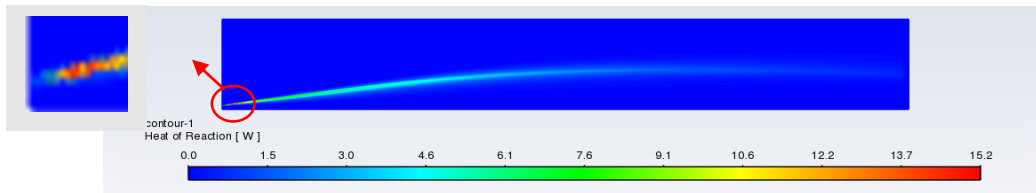


Fig. 5 Contour of heat of reaction during the methane-air combustion at  $Re_{Air} = 3.2 E+4$  ( $AV = 2$  m/s)

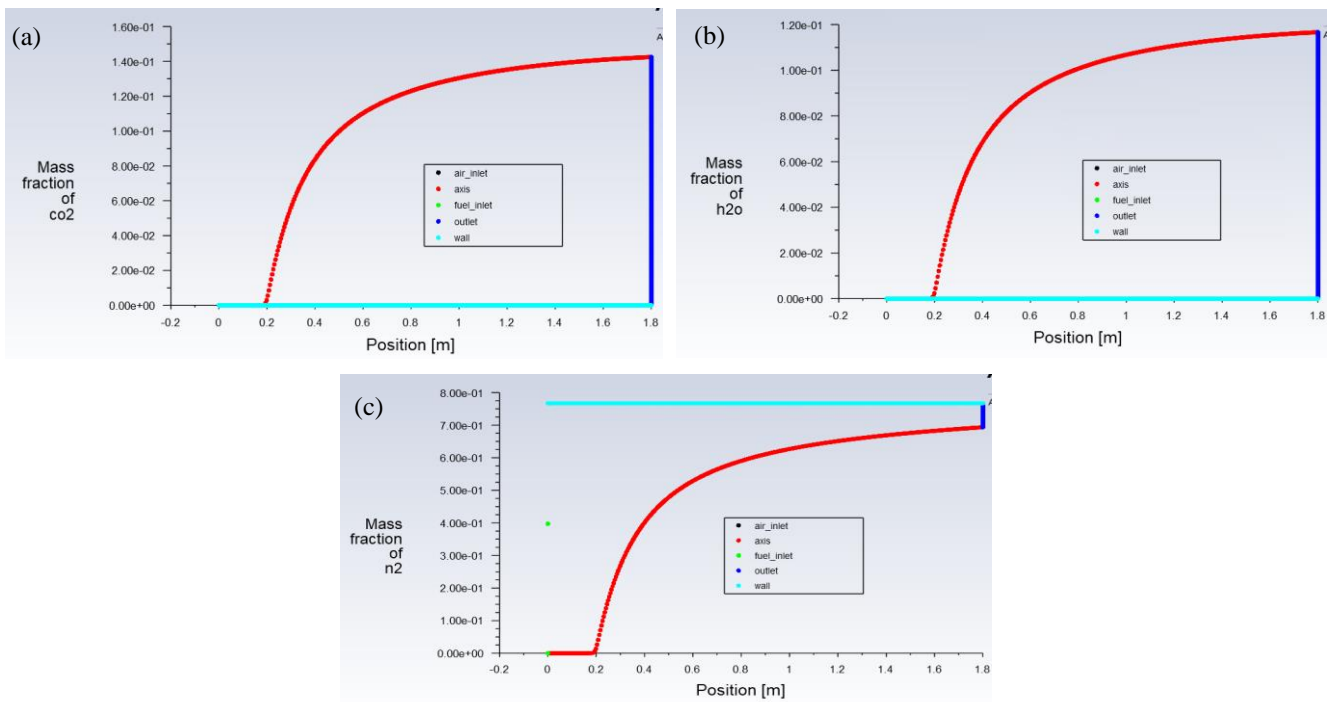


Fig. 6 Profiles of mass fraction of (a)  $CO_2$ , (b)  $H_2O$  and (c)  $N_2$  at  $Re_{Air} = 3.2 E+4$  ( $AV = 2$  m/s)

#### 4.1.2 Flow and Flame Characteristics at $Re_{CH_4} = 1.2 E+3$ ( $FV = 2$ m/s) when $Re_{Air} = 4.9 E+5$ ( $AV = 30$ m/s)

The minimum and maximum turbulent intensity are found to be 10.0 % and 681 % respectively at  $Re_{CH_4} = 1.2 E+3$  (

Fig. 7). The turbulent intensity is low compared to what is seen in Fig. 3. This is due to the low velocity (bulk) intake of the combustor. In another word, the relative change of velocity fluctuation over the average velocity is comparatively low in this case.

The static temperature reaches a maximum of 2269 K at  $Re_{CH_4} = 1.2 E+3$  (Fig. 8). It is also seen that at this specific condition, the flame is leaning to the bottom wall. This indicates

that the flame has very little expansion or lateral displacement. It is due to the presence of less fluctuation or turbulence in the flow. Also, the recess length further needs to be checked so that fully burnt and expanded flame could be achieved even at high Re conditions. The heat of the reaction reaches 2.9 W (Fig. 9). The generation of heat ( $\Delta H$ ) is less in this case which is due to the intake of less fuel to the system.

The maximum mass Fraction of  $CO_2$ ,  $H_2O$ , and  $N_2$  reaches 0.146, 0.120, and 0.767 respectively (Fig. 10). The mass fraction of combustion products does not change with temporal and spatial directions. The mass fraction falls within the acceptable limits of  $CH_4$ -Air combustion, as stated in [19]-[20]. Thus combustion is considered to be complete.

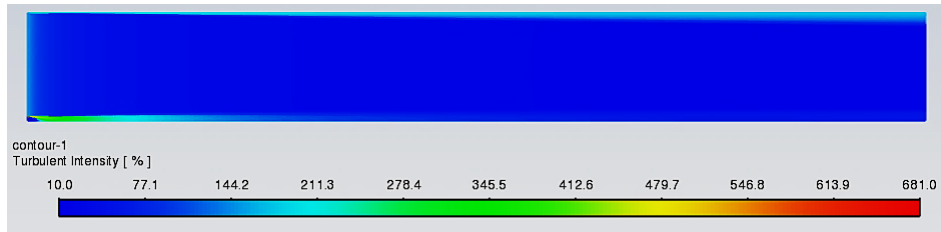


Fig. 7 Contour of the turbulent intensity at  $Re_{CH_4} = 1.2 E+3$  (FV = 2 m/s)

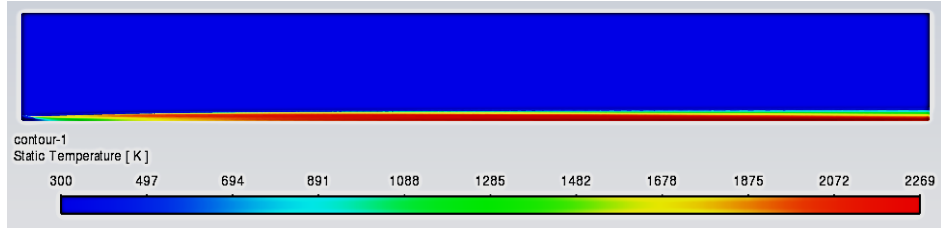


Fig. 8 Contour of the static temperature at  $Re_{CH_4} = 1.2 E+3$  (FV = 2 m/s)

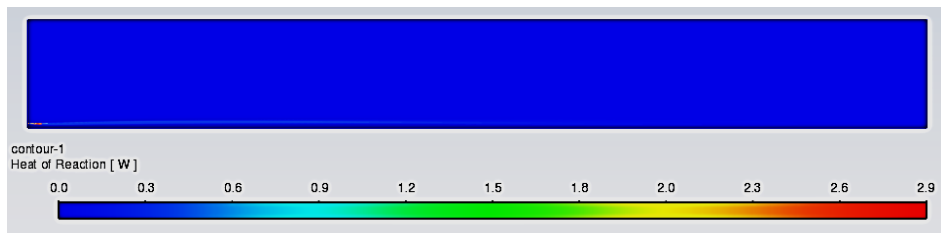


Fig. 9 Contour of heat of reaction at  $Re_{CH_4} = 1.2 E+3$  (FV = 2 m/s)

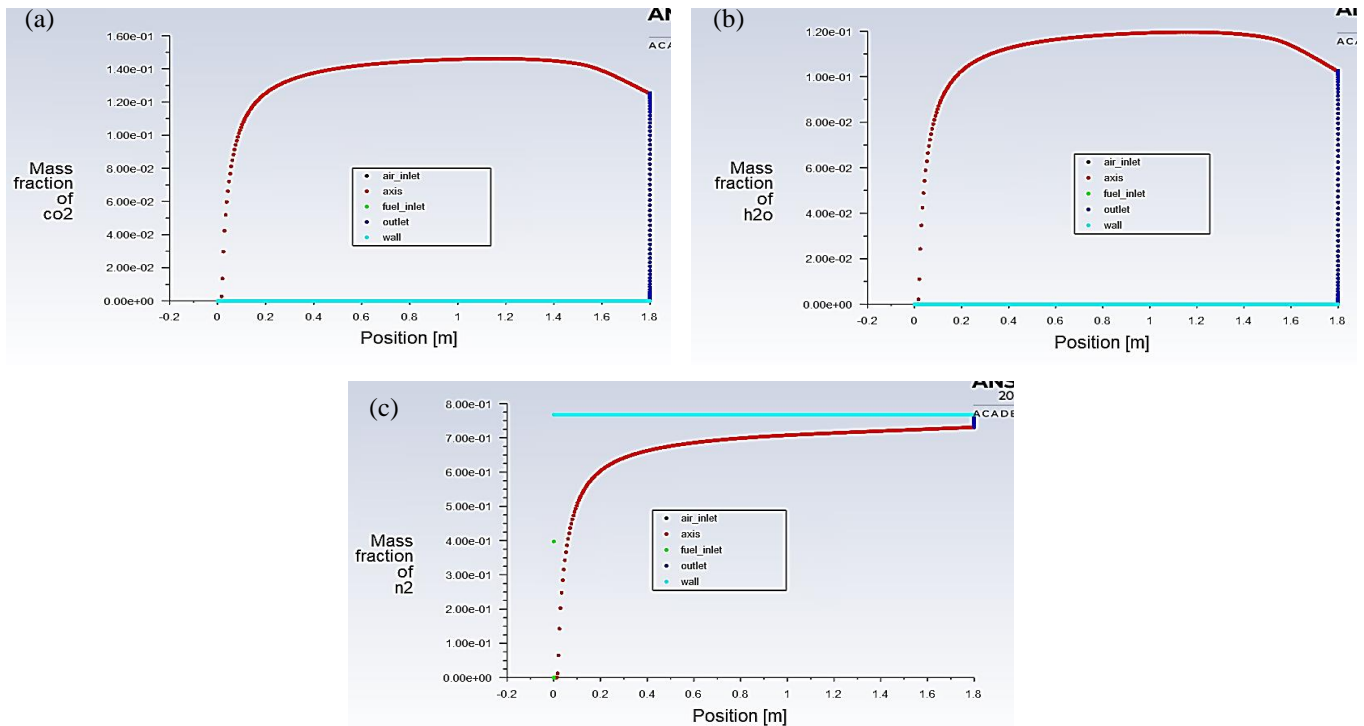


Fig. 10 Profiles of mass fraction of (a)  $CO_2$ , (b)  $H_2O$  and (c)  $N_2$  at  $Re_{CH_4} = 1.2 E+3$  (FV = 2 m/s)

#### 4.2 The Flow Properties and Combustion Dynamics at Variable $Re_{Air}$

The flow and combustion characteristics are investigated under  $AV = 4$  m/s to 20 m/s ( $Re_{Air} = 6.5 E+4$  to  $3.2 E+5$ ) while

keeping  $Re_{CH_4} = 1.8 E+4$ . It is observed from CFD analysis that going over  $AV = 14$  m/s, does not provide stable and complete combustion. Thus the flow and combustion characteristics at  $Re_{Air} = 6.5 E+4$  to  $2.3 E+5$  ( $AV = 4$  m/s to 14 m/s) are only reported here.

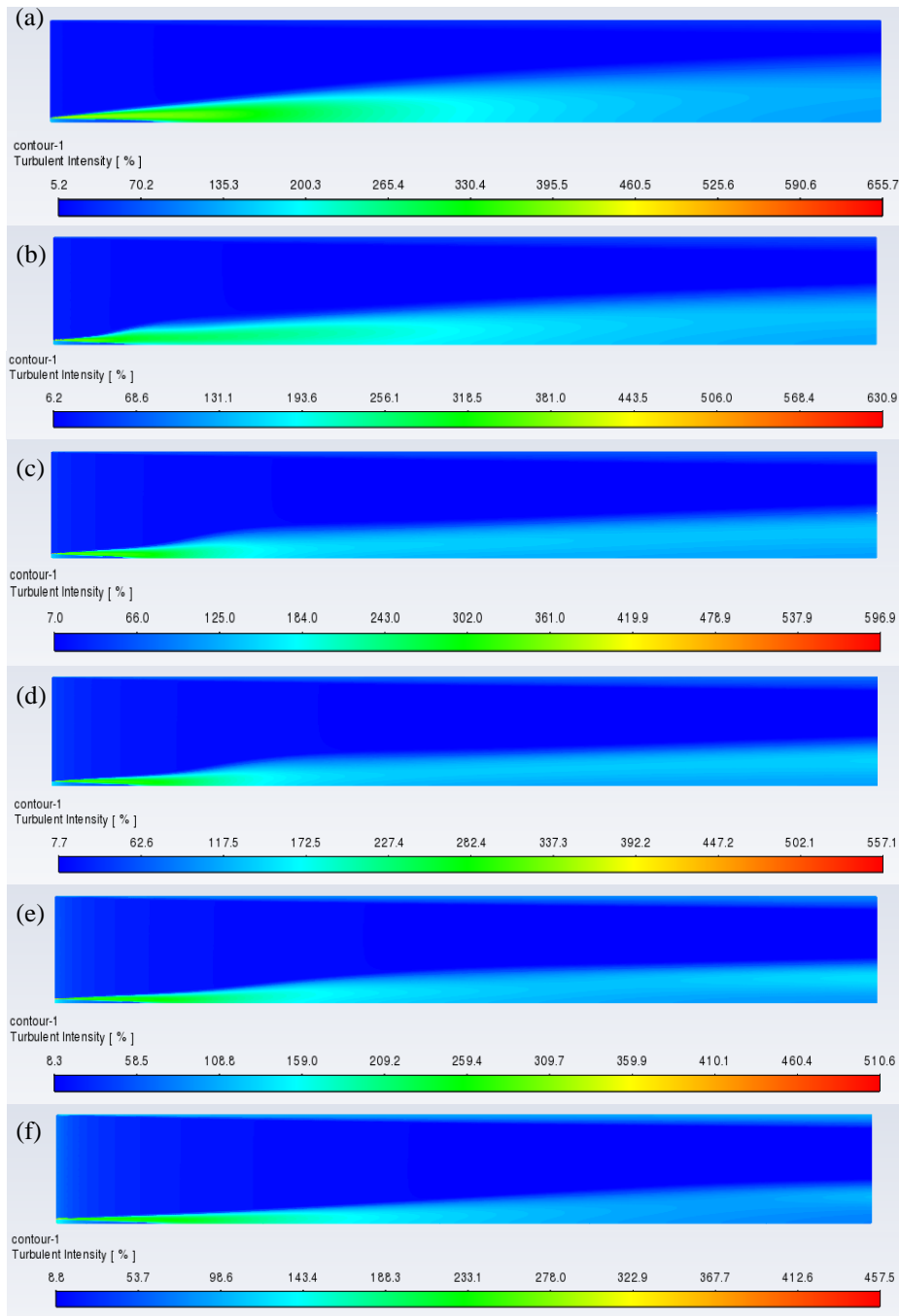
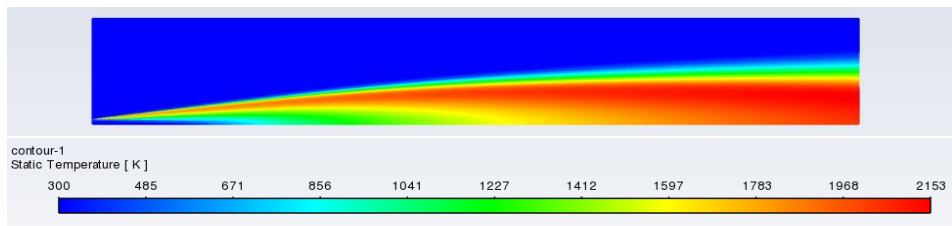


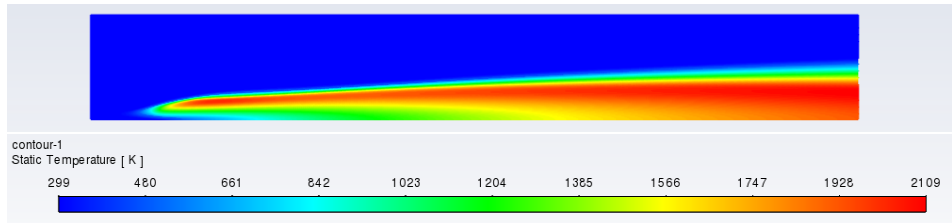
Fig. 11 The change in turbulent intensity contours at different  $Re_{air}$  values when  $Re_{CH_4}$  is kept at  $1.8 \times 10^4$ , (a)  $Re_{air} = 6.5 \times 10^4$ , (b)  $Re_{air} = 9.7 \times 10^4$  (c)  $Re_{air} = 1.3 \times 10^5$ , (d)  $Re_{air} = 1.6 \times 10^5$ , (e)  $Re_{air} = 1.9 \times 10^5$ , and (f)  $Re_{air} = 2.3 \times 10^5$

The turbulent intensity ( $I$ ) increases with the increase in  $Re_{Air}$  (Fig. 11). The  $I_{min}$  increases from 5.2% to 8.8 % whereas  $I_{max}$  decreases from 655.7% to 457.5% as  $Re_{Air}$  changes from  $6.5 \times 10^4$  (4 m/s) to  $2.3 \times 10^5$  (14 m/s). Increasing AV positively affects the  $I_{min}$ , but adversely affects the  $I_{max}$  as long as MV remains constant. However, the overall turbulence value is high and sufficient enough to provide sound mixing in the combustor. The turbulence helps in flame anchoring in the ignition point. For future high Re (or Mach) testing, the decrease in flow turbulence might induce flame instability. The flow swirling ratio needs to be increased. The swirlers with different geometries or blunt bodies should be installed upstream of the combustor.

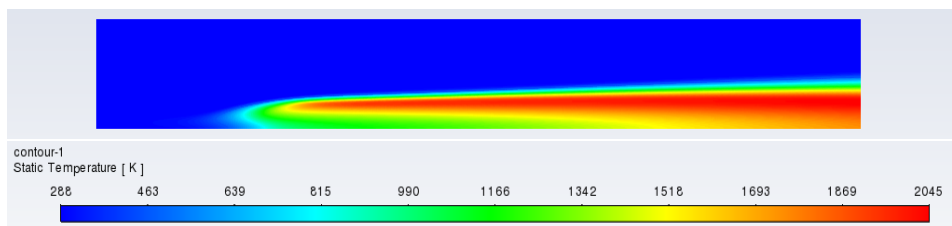
The static temperature decreases from 2153 K to 2013 K as  $Re_{Air}$  increases from  $6.5 \times 10^4$  to  $1.6 \times 10^5$ . (Fig. 12 (a-d)). After that the static temperature increases to 2086 K and 2350 K when  $Re_{Air} = 1.9 \times 10^5$  and  $2.3 \times 10^5$ , respectively (Fig. 12 (e-f)). This sudden decrease and increase in static temperature could be correlated to the change in reactant entrainment rate, flow fluctuation, etc. Also, the mesh growth rate, mesh fining rate should be further checked to get a stable static temperature at these operating conditions. However, the change observed in static temperature (2013 K-2350 K) falls within the standard limit of methane-air combustion [19]-[20].



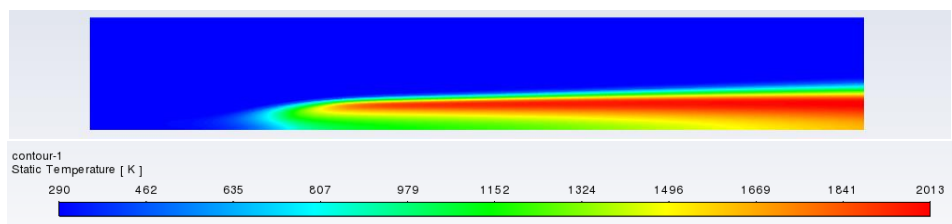
(a)



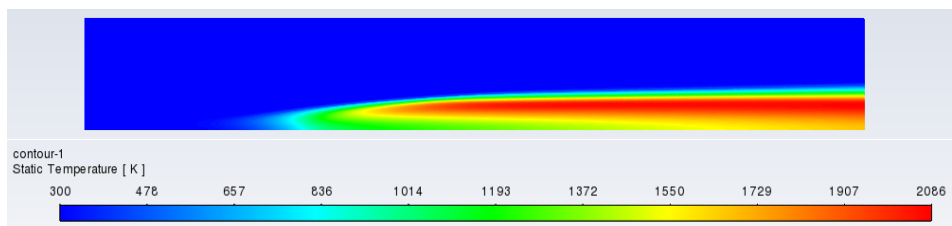
(b)



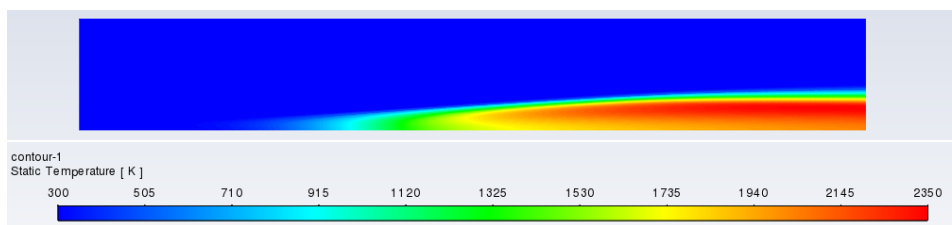
(c)



(d)



(e)



(f)

Fig. 12 The change in static temperature contours at different  $Re_{air}$  values when  $Re_{CH_4}$  is kept at  $1.8 E+4$ , (a)  $Re_{air} = 6.5 E+4$ , (b)  $Re_{air} = 9.7 E+4$  (c)  $Re_{air} = 1.3E+5$ , (d)  $Re_{air} = 1.6 E+5$ , (e)  $Re_{air} = 1.9 E+5$ , and (f)  $Re_{air} = 2.3 E+5$

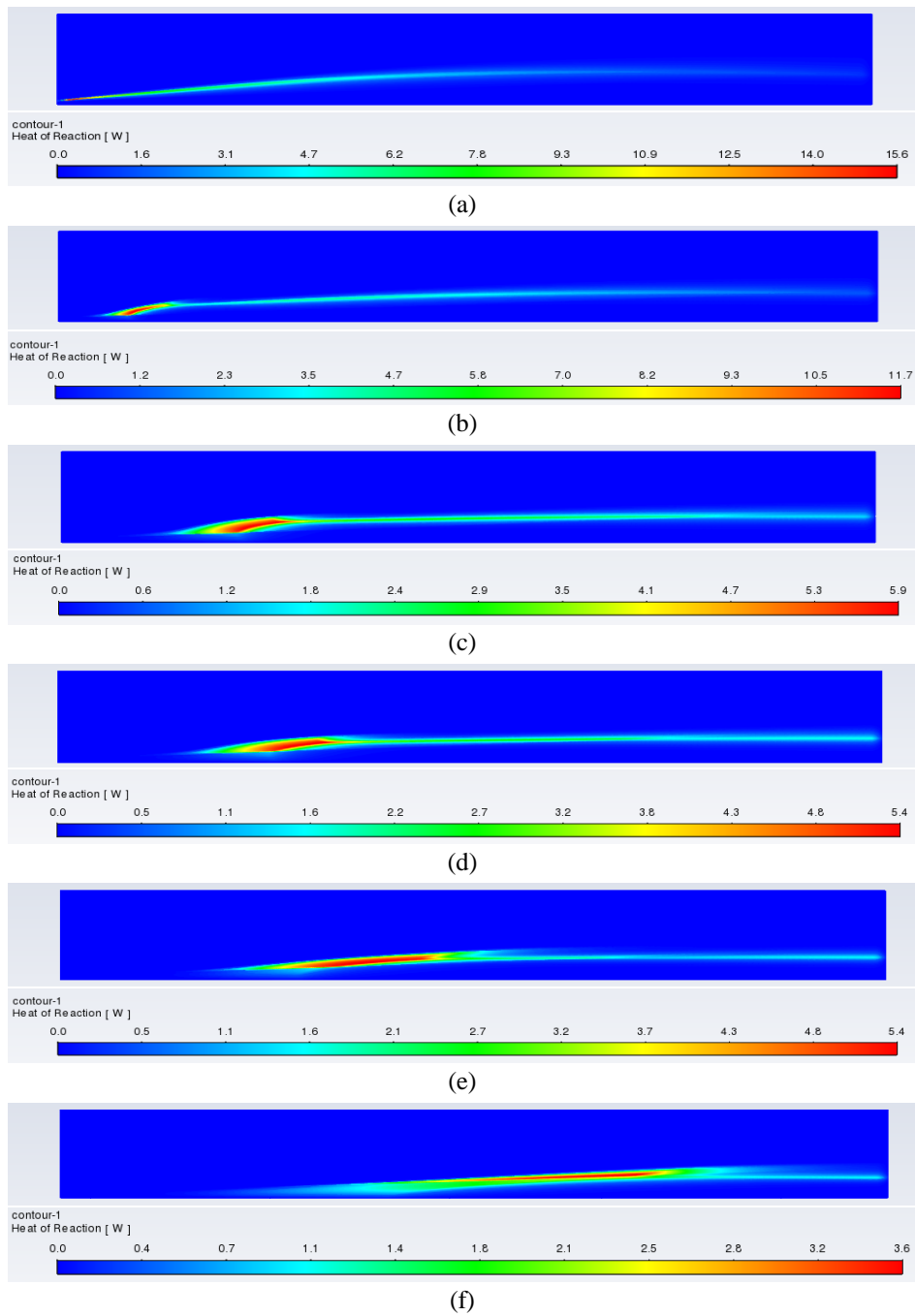


Fig. 13 The change in heat of reaction contours at different  $Re_{air}$  values when  $Re_{CH_4}$  is kept at  $1.8 E+4$ , (a)  $Re_{air} = 6.5 E+4$ , (b)  $Re_{air} = 9.7 E+4$  (c)  $Re_{air} = 1.3E+5$ , (d)  $Re_{air} = 1.6 E+5$ , (e)  $Re_{air} = 1.9 E+5$ , and (f)  $Re_{air} = 2.3 E+5$

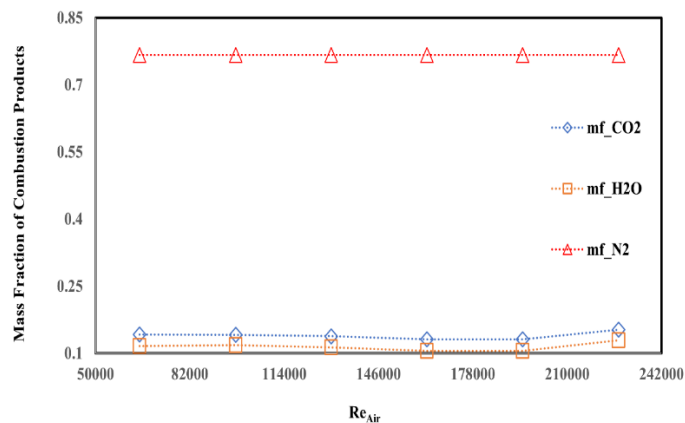


Fig. 14 The change in mass fraction of CO<sub>2</sub>, H<sub>2</sub>O and N<sub>2</sub> at different  $Re_{air}$  values when  $Re_{CH_4}$  is kept at  $1.8 E+4$ .

The heat of reaction (HOR) decreases from 15.6 W to 11.7 W as  $Re_{Air}$  increases from  $6.5 \times 10^4$  to  $9.7 \times 10^4$ . (Fig. 13 (a-b)). After that, the HOR value remains constant at around  $\sim 5.5$  W (Fig. 13 (c-d)). Then HOR drops to 3.6 W (Fig. 13 (f)). Overall HOR decreases with an increase in  $Re_{Air}$ . This decrease in heat generation is due to the insufficient supply of  $CH_4$  in the system. The  $CH_4$  supply should be adjusted (increased) to keep up the high level of HOR for each run of combustion tests. However, the heat of reaction magnitude is matched with the exothermic enthalpy of methane and air chemical reaction reported in [19]-[20]. The mass fraction of  $CO_2$  at the combustor outlet decreases from 0.142 to 0.131 as  $Re_{Air}$  increases from  $6.5 \times 10^4$  to  $1.9 \times 10^5$  (Fig. 14). The mass fraction of  $CO_2$  increases to 0.153 at  $Re_{Air} = 2.3 \times 10^5$  (Fig. 14). This increase in mass fraction of  $CO_2$  should be further examined by increasing the meshing and relaxation factor in CFD. The mass fraction of  $H_2O$  decreases from 0.116 to 0.105 when  $Re_{Air}$  changes from  $6.5 \times 10^4$  to  $1.9 \times 10^5$  (Fig. 14). The mass fraction of  $H_2O$  increases to 0.129 at  $Re_{Air} = 2.3 \times 10^5$  (Fig. 14). The average mass fraction of  $H_2O$  is found to be 0.114 which is similar to what is stated in [19]. The mass fraction of  $N_2$  at the combustor outlet remains constant at 0.767 when  $Re_{Air}$  changes from  $6.5 \times 10^4$  to  $2.3 \times 10^5$ . The overall trend of mass fraction of  $CO_2$ ,  $H_2O$ , and  $N_2$  is steadier. The range of production

mass fraction falls within the acceptable standard limit presented in [19].

### 4.3 The Flow Properties and Combustion Dynamics at Variable $Re_{CH_4}$

The CFD investigation is further extended by keeping  $Re_{Air}$  constant at  $4.9 \times 10^5$  ( $AV = 30$  m/s) and changing  $Re_{CH_4}$  from  $2.4 \times 10^3$  to  $1.8 \times 10^4$  ( $FV = 4$  m/s to 30 m/s). However, crossing over  $Re_{CH_4} = 7.2 \times 10^3$  ( $MV = 12$  m/s), does not provide stable or complete combustion. Thus, the authors are interested to present the results at  $Re_{CH_4} = 2.4 \times 10^3$  to  $7.2 \times 10^3$  ( $MV = 4$  m/s to 12 m/s) only. At this time, the effect of variable  $Re_{CH_4}$  (at constant  $Re_{Air}$ ) on the flame and flow properties is investigated. The minimum turbulent intensity ( $I_{min}$ ) of  $\sim 12\%$  is observed under all  $Re_{CH_4}$  conditions. However maximum turbulent intensity ( $I_{max}$ ) decreases from 667% to 524% as  $Re_{CH_4}$  varies from  $2.4 \times 10^3$  to  $7.2 \times 10^3$  (Fig. 15). The decrease in  $I_{max}$  could be related to the presence of less flow fluctuation in the system. Installing swirlers or a bluff body upstream of the combustor could enhance the flow turbulence at high Reynolds conditions. Also, perforated plates with various blockage ratios could be used at the combustor inlet. The use of this kind of plate alters the turbulence level, eddy size, and overall flow fluctuation in the system.

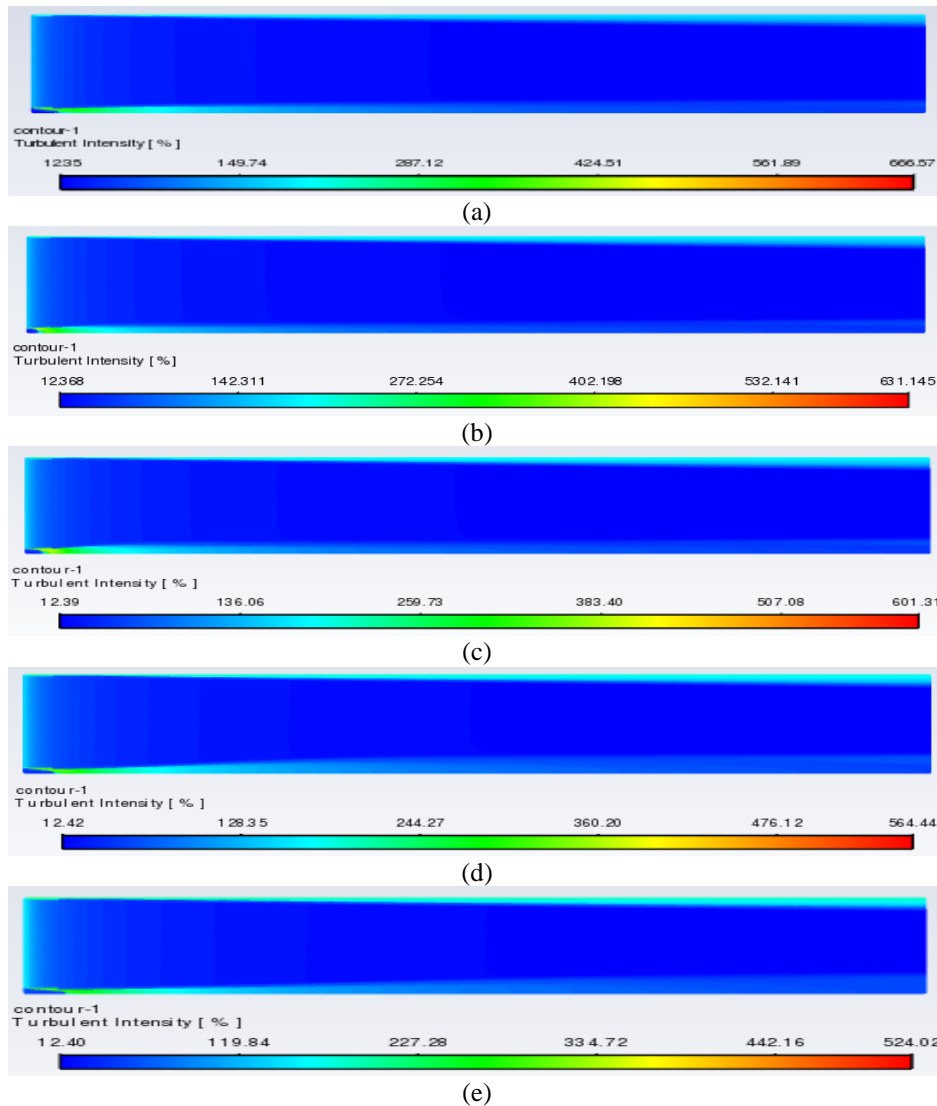


Fig. 15 Turbulent Intensity contour at variable  $Re_{CH_4}$  when  $Re_{Air}$  is kept at  $4.9 \times 10^5$ , (a)  $Re_{CH_4} = 2.4 \times 10^3$ , (b)  $Re_{CH_4} = 3.6 \times 10^3$  (c)  $Re_{CH_4} = 4.8 \times 10^3$ , (d)  $Re_{CH_4} = 6.0 \times 10^3$ , and (e)  $Re_{CH_4} = 7.2 \times 10^3$

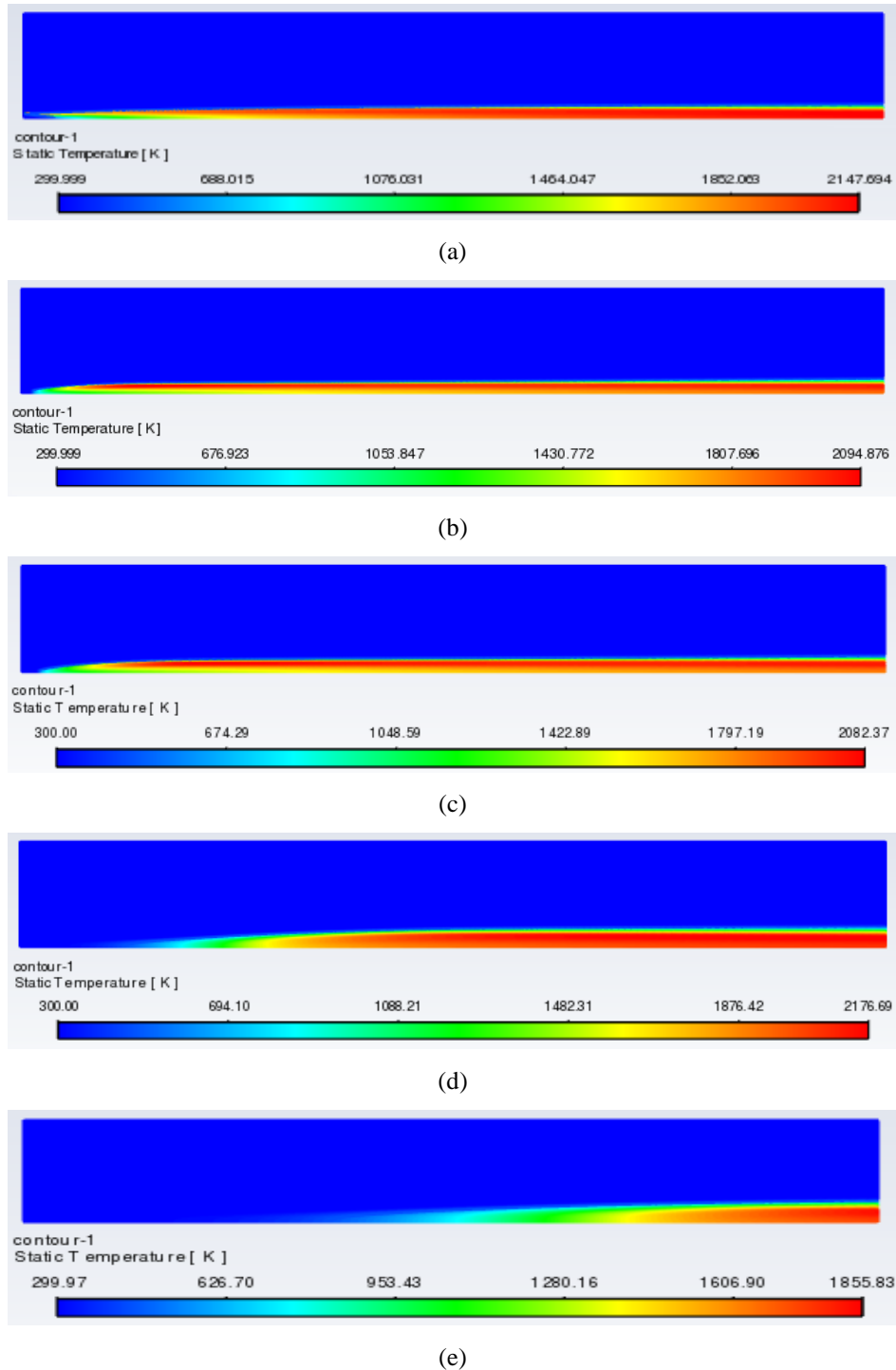


Fig. 16 The change in static temperature contour at variable  $Re_{CH_4}$  when  $Re_{Air}$  is kept at  $4.9 \times 10^5$ , (a)  $Re_{CH_4} = 2.4 \times 10^3$ , (b)  $Re_{CH_4} = 3.6 \times 10^3$  (c)  $Re_{CH_4} = 4.8 \times 10^3$ , (d)  $Re_{CH_4} = 6.0 \times 10^3$ , and (e)  $Re_{CH_4} = 7.2 \times 10^3$

The static temperature decreases from 2148 K to 2082 K as  $Re_{CH_4}$  varies from  $2.4 \times 10^3$  to  $4.8 \times 10^3$  (Fig. 16 (a-c)). The static temperature is then increased to 2177 K and decreased to 1856 K at  $Re_{CH_4} = 6.0 \times 10^3$  and  $7.2 \times 10^3$ , respectively. The static temperature, in general, has decreased with the increase in  $Re_{CH_4}$ . The decrease in static temperature results due to the insufficient supply of air into the combustor. Making the mixture oxygen-rich might mitigate this issue. In this research, only the stoichiometric mixture is considered. The authors do believe that the effect of different equivalence ratios ( $\phi$ ) or lean-to-rich mixture conditions at each  $Re$  should be investigated using both CFD and experiments.

The heat of reaction is found to be 3.0 at  $Re_{CH_4} = 2.4 \times 10^3$  (Fig. 17 (a)), whereas it reaches a maximum of 8.9 and 8.1 at  $Re_{CH_4} = 3.6 \times 10^3$  and  $4.8 \times 10^3$ , respectively (Fig. 17 (b-c)). The minimum heat of reactions of 1.3 and 1.2 are observed at  $Re_{CH_4} = 6.0 \times 10^3$  and  $7.2 \times 10^3$ , respectively (Fig. 17 (d-e)). This change in heat of reaction is because of the constant supply of air while the methane velocity keeps changing. To overcome this, the air velocity needs to be adjusted at variable  $Re_{CH_4}$ . A test matrix should be developed for air and methane flow velocities accommodating various equivalence ratios ( $\phi$ ).

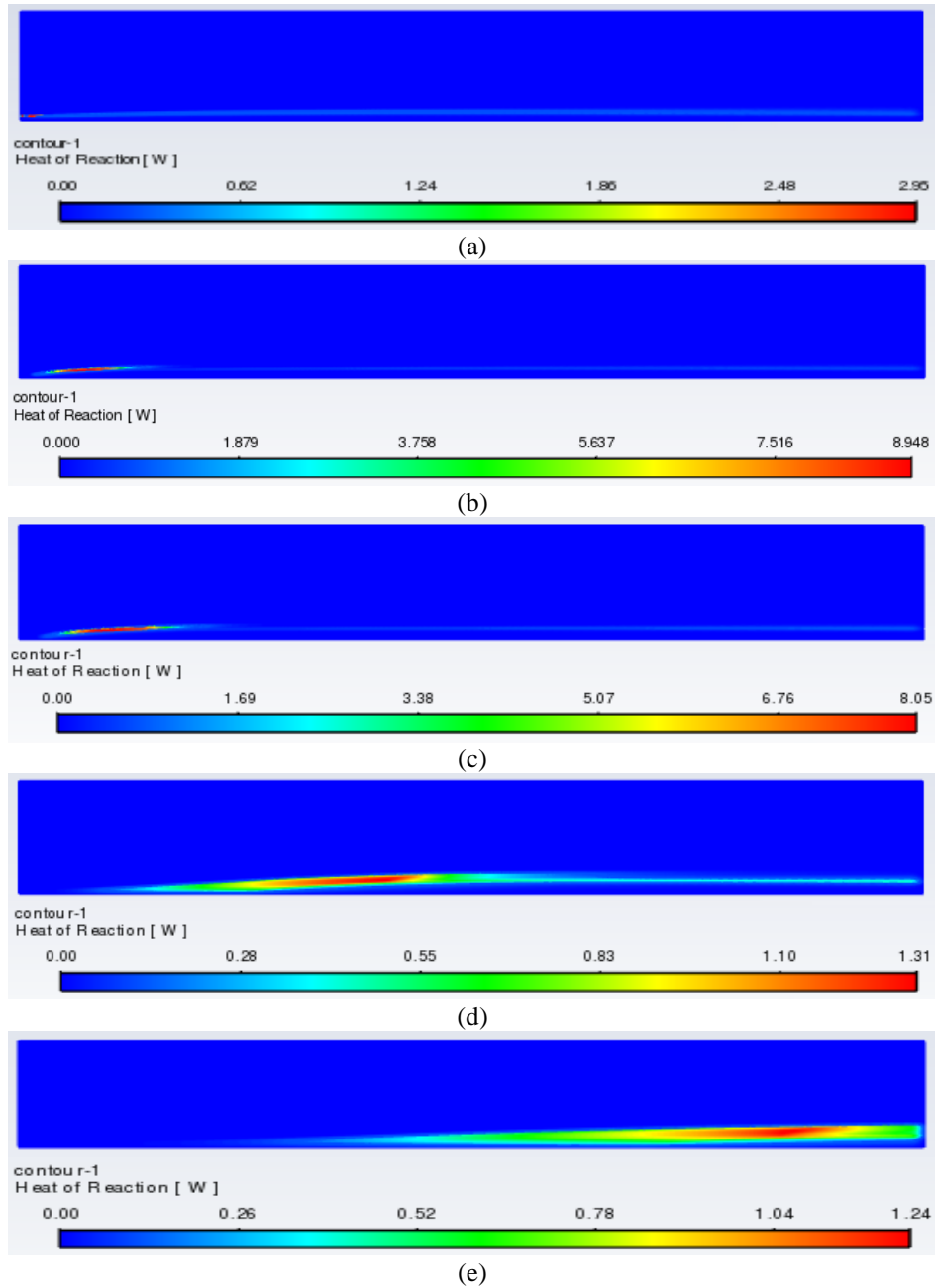


Fig. 17 The change in heat of reaction at variable  $Re_{CH_4}$  when  $Re_{Air}$  is kept at  $4.9 \times 10^5$ , (a)  $Re_{CH_4} = 2.4 \times 10^3$ , (b)  $Re_{CH_4} = 3.6 \times 10^3$  (c)  $Re_{CH_4} = 4.8 \times 10^3$ , (d)  $Re_{CH_4} = 6.0 \times 10^3$ , and (e)  $Re_{CH_4} = 7.2 \times 10^3$

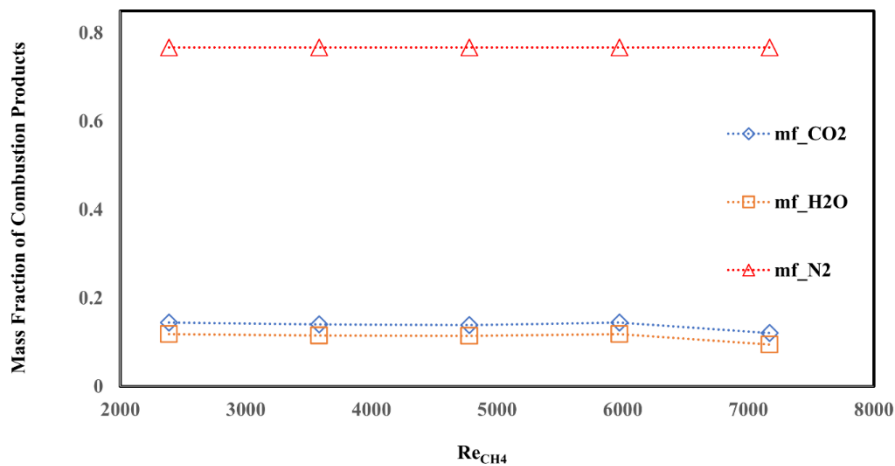


Fig. 18 The change in mass fraction of  $CO_2$ ,  $H_2O$  and  $N_2$  at variable  $Re_{CH_4}$  when  $Re_{Air}$  is kept at  $4.9 \times 10^5$ .

The mass fraction of CO<sub>2</sub> decreases from 0.144 to 0.139 as Re<sub>CH<sub>4</sub></sub> increases from 2.4 E+3 to 4.8 E+3 (Fig. 18). The mass fraction reaches back to 0.144 at Re<sub>CH<sub>4</sub></sub> = 6.0 E+3 and again drops to 0.121 at Re<sub>CH<sub>4</sub></sub> = 7.2 E+3. There is a change in the mass fraction of CO<sub>2</sub>, however, the change is not significant for most of the CFD runs. The mass fraction of H<sub>2</sub>O decreases with the increase in Re<sub>CH<sub>4</sub></sub>. It decreases from 0.118 to 0.114 as Re<sub>CH<sub>4</sub></sub> changes from 2.4 E+3 to 4.8 E+3 (Fig. 18). After that, it reaches the original value of 0.118 and then drops to 0.095. An average mass fraction of H<sub>2</sub>O of 0.112 is observed from the CFD study. The mass fraction of N<sub>2</sub> remains constant at 0.767 at all Re<sub>CH<sub>4</sub></sub> conditions. The mass fraction of products falls within the acceptable limit of CH<sub>4</sub>-air combustion as reported elsewhere [19]-[20].

The ongoing research is focused on optimizing the possible test operating conditions for methane-air combustion under a small-scale rectangular combustor. In this research, a cross-validation technique has been implemented to develop an optimum test matrix. First, the fuel injection velocity is kept constant and air injection velocity is changed. The second time, the air injection velocity is kept constant and fuel injection velocity is changed. The authors found a preliminary test operating conditions: Re<sub>Air</sub> and Re<sub>CH<sub>4</sub></sub> could be changed from 3.2 E+4 to 2.3 E+5 and 1.2 E+3 to 7.2 E+03, respectively. The authors are planning to continue this research using the reverse test validation method where at each of the fuel injection velocities, a wide range of air injection velocities will be investigated. Afterward, a complete test matrix will be proposed.

## 5 Conclusions

A species transport Model (STM) with 2D axisymmetric space is used to study the stoichiometric ( $\phi = 1$ ) CH<sub>4</sub>-Air combustion under an axisymmetric small-scale combustor. In this study, a parallel injection of methane and air streams is considered. The methane and air are introduced to the combustor without any prior mixing thus the mixture is non-premixed.

- The combustion and flow characteristics are investigated at air injection velocity (AV) = 2 m/s to 30 m/s and fuel injection velocity (FV) = 2 m/s to 30 m/s.
- The research shows that AV over 14 m/s and FV over 12 m/s do not provide stable and complete combustion. Thus, the authors come up with preliminary test operating conditions: Re<sub>Air</sub> = 3.2 E+4 to 2.3 E+5 and Re<sub>CH<sub>4</sub></sub> = 1.2 E+3 to 7.2 E+3.
- In the first approach of CFD study, FV is kept at 30 m/s (Re<sub>CH<sub>4</sub></sub> = 1.8 E+4) while AV is changed from 2 m/s to 14 m/s (Re<sub>Air</sub> = 3.2 E+4 to 2.3 E+5). At these specific conditions, I<sub>min</sub> increases from 5.2 % to 8.8 % whereas I<sub>max</sub> decreases from 655.7 % to 457.5%. The static temperature varies from 2013 K to 2350 K. The heat of reaction (HOR) is decreased from 15.6 W to 3.6 W. The decrease in HOR value could be linked to the supply of less CH<sub>4</sub> into the combustor. The average mass fraction of the CO<sub>2</sub>, H<sub>2</sub>O, and N<sub>2</sub> are found to be 0.139, 0.115, and 0.767, respectively.
- In the second approach of the CFD study, a cross-test validation technique is implemented. Now, AV is kept at 30 m/s (Re<sub>Air</sub> = 4.9 E+5) while FV is changed from 2 m/s to 12 m/s (Re<sub>CH<sub>4</sub></sub> = 1.2 E+3 to 7.2 E+3). The I<sub>min</sub> remains constant at ~12% whereas the I<sub>max</sub> drops from 681% to 524 %. The static temperature varies between 1856 K and 2269 K. The heat of reaction (HOR) varies from 1.2 W to 8.9 W.

The average mass fractions of CO<sub>2</sub>, H<sub>2</sub>O, and N<sub>2</sub> are 0.139, 0.113, and 0.767, respectively.

- The authors would like to conduct more research using combustion modeling, analytical analysis, and experimental tests. The authors are also interested to validate the CFD results with the experimental tests soon. The authors will investigate the effect of different equivalence ratios ( $\phi$ ) and Reynolds numbers on the flow and flame characteristics and see how that affects the combustor design.

## Nomenclature

STM	Species Transport Model
AV	Airflow Velocity
FV	Fuel flow Velocity
$\mu_t$	Turbulent Viscosity
D <sub>t</sub>	Turbulent Diffusivity
TKE	Turbulent Kinetic Energy
G <sub>b</sub>	Generation of TKE due to the Change in Buoyancy Forces
G <sub>k</sub>	Generation of TKE due to the Change in Velocity Gradient
Y <sub>i</sub>	The Local Mass Fraction of Each Species
$\sigma_k, \sigma_\epsilon$	Source terms used in Energy Transport Analysis
S <sub>i</sub>	Rate of Creation by Particulate, Soot, etc.
R <sub>i</sub>	Net Rate of Production of Species i by the Chemical Reaction
$\Delta T$	Change in Temperature during the Combustion
J <sub>i</sub>	The Diffusion Flux of Species i
D <sub>T,i</sub>	Coefficients of the Thermal Diffusion
D <sub>i,m</sub>	Coefficients of the Mass Diffusion
Sc <sub>t</sub>	The Turbulent Schmidt Numbers
$\rho$	Density of the reactants
k	Thermal Conductivity
C <sub>p</sub>	Specific Heat
Re <sub>air</sub>	Reynolds Number Based on Air Velocity and Air Inlet Slot Geometry
Re <sub>CH<sub>4</sub></sub>	Reynolds Number Based on Fuel Velocity and Fuel Slot Geometry
$\phi$	Equivalence Ratio-a ratio of actual A/F ratio over stoichiometric A/F ratio

## Acknowledgments

This research is not supported by any organizations or agencies. The authors would like to thank the Department of Mechanical Engineering and the IT team of Embry-Riddle Aeronautical University, Prescott, USA for providing access to the ANSYS 2021 R1 academic.

## Declaration of Competing Interest

The authors declared that there are no known competing financial interests or personal relationships that could have appeared to influence the research work presented in this article.

## References

- [1] CO<sub>2</sub> Emissions from Fuel Combustion (2020 Edition) by *International Energy Agency (IEA)*, Accessed: 2021, Available: <http://energyatlas.iea.org/#!/tellmap/1378539487>
- [2] Hossain, M.A., 2020. Laser Diagnostics of Compressible and High-intensity Premixed Methane-air Combustion Inside a Backward Facing Step Combustor Using High-repetition Rate CH-PLIF and PIV (Doctoral dissertation, The University of Texas at El Paso).
- [3] Islam, M.N.A., Hossain, M.A., De la Torre, M., Acosta-Zamora, A. and Choudhuri, A.R., 2019. Laser Diagnostics of Highly Turbulent Premixed Methane-Air Flow Over a

- Backward Facing Step Using PIV and OH-PLIF. In *AIAA Propulsion and Energy 2019 Forum* (p. 4323).
- [4] Hossain, M.A., Islam, M.N.A. and Choudhuri, A., 2019, July. Flame Imaging of Highly Turbulent Premixed Methane-Air Combustion Using Planar Laser Induced Fluorescence (PLIF) of CH (CX). In *ASME Power Conference* (Vol. 59100, p. V001T01A008). American Society of Mechanical Engineers.
- [5] Hossain, M.A., Islam, M.N.A., Hossain, W. and Choudhuri, A.R., 2020. CH-PLIF Diagnostics of High Intensity Turbulent Premixed Methane-Air Combustion. In *AIAA Scitech 2020 Forum* (p. 1705).
- [6] Hamzah, D.A., 2015. Theory Comparison between Propane and Methane Combustion inside the Furnace. *International Journal of Current Engineering and Technology*, 5(4), pp.2429-2434.
- [7] Ibrahim, I.A., Gad, H.M. and Shabaan, M.M., 2014. Numerical simulation of combustion characteristics of methane flame in an axisymmetric combustor model. *Global Journal of Engineering Science*, pp.2349-4506.
- [8] Pitsch, H. and Peters, N., 1998. A consistent flamelet formulation for non-premixed combustion considering differential diffusion effects. *Combustion and flame*, 114(1-2), pp.26-40.
- [9] Matalon, M., 2007. Intrinsic flame instabilities in premixed and nonpremixed combustion. *Annu. Rev. Fluid Mech.*, 39, pp.163-191.
- [10] Lacaze, G. and Oefelein, J.C., 2012. A non-premixed combustion model based on flame structure analysis at supercritical pressures. *Combustion and Flame*, 159(6), pp.2087-2103.
- [11] Barths, H., Hasse, C. and Peters, N., 2000. Computational fluid dynamics modelling of non-premixed combustion in direct injection diesel engines. *International Journal of Engine Research*, 1(3), pp.249-267.
- [12] Hossain, M.A., December 2021. Study of Ultra Low-swirl Burner (LSB) for Non-Premixed Methane-Air Combustion Using Computational Analysis. Proceedings of the *International Conference on Mechanical Engineering and Renewable Energy 2021 (ICMERE 2021)*, 12 – 14, Chattogram, Bangladesh.
- [13] Kassem, H.I., Saqr, K.M., Aly, H.S., Sies, M.M. and Wahid, M.A., 2011. Implementation of the eddy dissipation model of turbulent non-premixed combustion in OpenFOAM. *International Communications in Heat and Mass Transfer*, 38(3), pp.363-367.
- [14] Kongre, U.V. and Sunnapwar, V.K., 2010. CFD modeling and experimental validation of combustion in direct ignition engine fueled with diesel. *International Journal of Applied Engineering Research*, 1(3), p.508.
- [15] Enagi, I.I., Al-Attab, K.A. and Zainal, Z.A., 2017. Combustion chamber design and performance for micro gas turbine application. *Fuel Processing Technology*, 166, pp.258-268.
- [16] Davis, S.G., Joshi, A.V., Wang, H. and Egolfopoulos, F., 2005. An optimized kinetic model of H<sub>2</sub>/CO combustion. *Proceedings of the combustion Institute*, 30(1), pp.1283-1292.
- [17] D'Errico, G., Lucchini, T., Onorati, A. and Hardy, G., 2015. Computational fluid dynamics modeling of combustion in heavy-duty diesel engines. *International Journal of Engine Research*, 16(1), pp.112-124.
- [18] Hossain, M.A., 2022. Computational Study of Methane-air Combustion Using the Species Transport Model. In *AIAA SCITECH 2022 Forum* (p. 1102).
- [19] Ge, H.W. and Gutheil, E., Modeling and Simulation of Turbulent Spray Flows Using RANS and PDF Transport Equations.
- [20] Urzica, D. and Gutheil, E., 2008. Counterflow combustion modeling of CH<sub>4</sub>/air and CH<sub>4</sub>/O<sub>2</sub> including detailed chemistry. *Italy: ILASS*.

This page is left intentionally blank

# Journal of Engineering Advancements (JEA)

DOI: <https://doi.org/10.38032/jea>

---

Indexed by:



Volume 03 Issue 01

DOI: <https://doi.org/10.38032/jea.2022.01>

---

**Published by: SciEn Publishing Group**

Website: [www.scienpg.com](http://www.scienpg.com)